Beam Energy and System-size Dependence of the Space-time Extent of the Pion Emission Source Produced in Heavy-Ion Collisions

A Dissertation Presented

by

Alex Mwai

to

The Graduate School

in Partial Fulfillment of the Requirements

for the Degree of

Doctor of Philosophy

in

Chemistry

(Chemical Physics)

Stony Brook University

December 2014

Stony Brook University

The Graduate School

Alex Mwai

We, the dissertation committee for the above candidate for the Doctor of Philosophy degree, hereby recommend acceptance of this dissertation.

Roy Lacey - Dissertation Advisor

Professor, Department of Chemistry

Jiangyong Jia - Chairperson of Defense

Associate Professor, Department of Chemistry

Trevor Sears

Professor, Department of Chemistry

Derek Teaney

Associate Professor, Department of Physics and Astronomy

This dissertation is accepted by the Graduate School.

Charles Taber

Dean of the Graduate School

Abstract of the Dissertation

Beam Energy and System-size Dependence of the Space-time Extent of the Pion Emission Source Produced in Heavy-Ion Collisions

by

Alex Mwai

Doctor of Philosophy

in

Chemistry

(Chemical Physics)

Stony Brook University

2014

The primary goal of high-energy nuclear physics is to develop a thorough understanding of the QCD phase diagram: Its different phases, their boundaries, and the physics they define. Heavy-ion collisions reproduce at a microscale the conditions necessary to initiate the phase transitions of nuclear matter that are only possible at extreme temperatures (T) and baryon chemical potential (μ_B).

An important probe utilized in studies of the hot and dense matter created in heavy-ion collisions is the method of Hanbury-Brown and Twiss interferometry. The technique is useful in providing measurements in space and time of the pion emission sources at freeze-out. One enduring question of interest in studies of the QCD phase diagram is the position in T and μ_B coordinates of the QCD Critical End Point (CEP) as well as the onset of deconfinement, as predicted by model calculations. According to these models, the Equation of State (EoS) should soften in the vicinity of the CEP and/or a first order phase transition. The expanding hot and dense system is sensitive to changes in the EoS. A softening of the EoS will therefore be reflected in measurements of the final size in space-time of the pion emission source. Another question is how small can a system be before we see a turn-off of hydrodynamically driven final-state effects.

In this thesis, detailed HBT measurements obtained using the PHENIX detector at the Relativistic Heavy Ion Collider (RHIC) are presented for three beam collision energies

($\sqrt{s_{NN}}$ = 39, 62, and 200 GeV) and three collision species ($d + Au$, $Cu + Cu$, and $Au+Au$). The measurements are studied for their dependence on collision geometry and transverse mass (m_T), and observations are made on how the small asymmetric system, $d + Au$, compares to the $A + A$ systems for these dependencies. In addition, newly observed universal scaling patterns with the initial transverse size, $\bar{R}$, and $1/\sqrt{m_T}$ for both RHIC HBT measurements and the $Pb+Pb$ collision system at $\sqrt{s_{NN}} = 2.76$ TeV are discussed. Finally, observations of non-monotonic behavior in the excitation functions of HBT measurements are presented in detail and their significance reflected on. The results presented here provide a valuable extension to the current understanding of the dynamics of the hot and dense systems produced in heavy-ion collisions.

To Mum: The most beautiful, selfless person I will ever get to know.

To Mwaniki and Kiama: My best friends and the reason I do this.

Contents

List of Figures

List of Tables

Acknowledgments

I would like to express my most sincere and heartfelt gratitude to my advisor, Professor Roy Lacey. One could not ask for a better mentor and friend, and this work is testament to his incredible patience, mentorship, and support over the course of my graduate school career.

I would also like to thank the chair of my committee, Professor Jiangyong Jia, for his kind assistance and guidance through the years, and for being such a great role model for all of us in the nuclear chemistry group. Thanks also go to my committee members, Professor Trevor Sears and Professor Derek Teaney, for their very helpful feedback which helped me see this thesis to completion.

Over the years, I have benefited immensely from the advice, support, and encouragement of Dr. Arkadiy Taranenko and Dr. Nuggehalli Ajitanand. I have learnt a lot from them – both about science and about life in general – and it was indeed a great honor working with them.

To current and past members of the nuclear chemistry group at Stony Brook: Thank you for the wonderful years we have shared. You made graduate school life so much easier.

Advancements in science take team effort and nothing exemplifies that better than the PHENIX collaboration. I consider myself extremely lucky to have been part of such a unique international team at the forefront of scientific discovery. The lessons I take with me from all my interactions with its members, I am certain, will prove to be invaluable.

Finally, to my family and friends: Thank you for standing by me, and for giving me your blessings to get me through this journey.

1. Introduction

1.1. Standard Model

The standard model is a theory of physics that provides a unified account of all the interactions of matter and the forces of nature, with the exception of gravity. It has proven to be highly successful, withstanding even the toughest of scrutiny. The Standard Model has 17 named particles – 12 fermions and 5 bosons, of which the Higgs boson discovered in 2012 is the most recent. All the elementary particles that are the building blocks of matter are fermions which can be described using Fermi-Dirac statistics. Other elementrary particles are the force carriers which mediate interactions between matter and are subject to Bose-Einstein statistics (Bosons).

1.2. Quantum Chromodynamics

Quantum Chromodynamics (QCD) is a non-abelian gauge theory of strong interaction, describing how the elementary particles, quarks, interact by exchange of the gauge bosons for the strong force, gluons. These strong interactions are only possible because both quarks and gluons carry color charge, which is analogous to electric charge. But unlike the chargeless photon which mediates electromagnetic interactions but cannot interact with another photon, a gluon is able to interact with another gluon. This characteristic makes QCD interactions a lot more complex and gives rise to very interesting features. One distigushing property of the QCD theory is asymptotic freedom. The interaction strength between two quarks is defined in terms of a coupling constant, α_s, as:

$$\alpha_s = g_s^2/4\pi \tag{1.1}$$

where g_s is the QCD gauge coupling. Asymptotic freedom describes how the interaction strength diminishes as the separation between the two quarks grows smaller and will asymptotically approach zero at very small separations (this corresponds to higher energies and momentum). Eqn. 1.1 describes this logarithmic decrease which is as a result of gluon self-coupling, leading to an anti-screening i.e., effective color charge increases with distance [110].

Another very important distinguishing characteristic of QCD is color-confinement, manifest at low energy. As you try to separate a quark-antiquark pair by pulling them apart, their interaction becomes increasingly stronger as their separation distance increases. Past a certain distance, the energy applied to separating the quark-antiquark pair will go into forming a new quark-antiquark pair. This is the reason we cannot observe free quarks in the lab (i.e., at macroscopic distances) since at such distances, quarks and gluons are bound in color singlet states or hadrons [110].

Over the years, several theoretical methods have been developed to provide a quantitative test of the validity of QCD. Two of the most important are Lattice QCD (LQCD) and Perturbative QCD (PQCD). At high energies, corresponding to high temperatures and or baryon-chemical potential, QCD is solved through the application of PQCD and calculations based on this perturbative approach have provided some of the most precise validations of the theory [104] . At lower energies, there is an increase in the coupling constant which renders PQCD inaccurate [87]. In these regimes of energy ($\sim <1$ GeV), LQCD, which involves approximations of Euclidean space-time on a hypercubic lattice, is a more viable option since it does not rely on the small parameter expansions of PQCD. LQCD currently allows for the most precise determination of α_s [64].

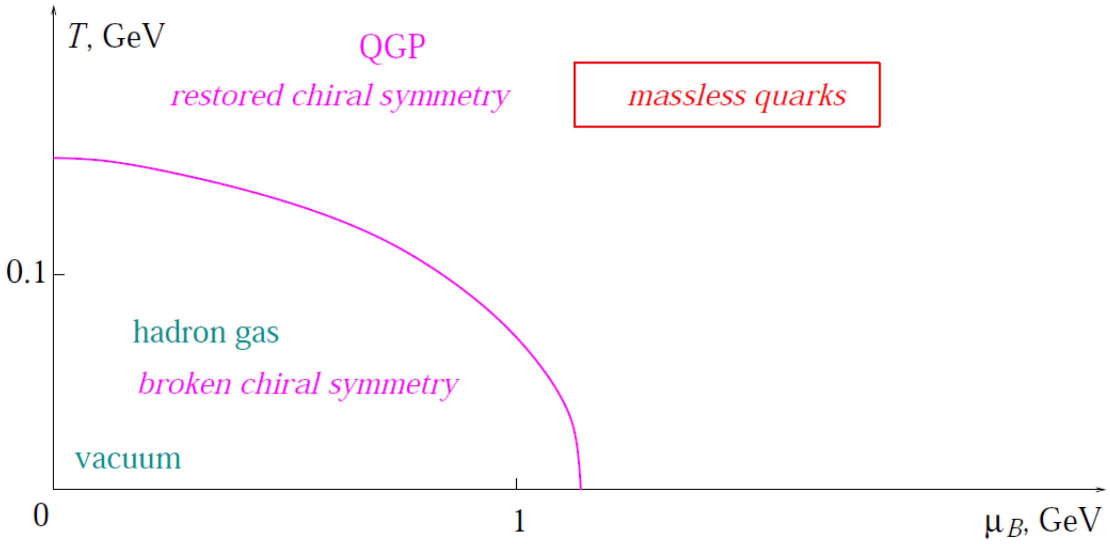

Figure 1.1.: The conjectured QCD phase diagram

One of the central conjectures of the QCD theory is the QCD phase diagram. The QCD phase diagram defines the state of a system of strongly interacting matter in terms of the thermodynamic parameters of temperature (T) and baryon chemical potential (μ_B). It shows the different phases of the system for a set of T and μ_B, the physics defining these phases, and the boundaries that separate them [106]. The current QCD phase diagram includes input from model calcuations, PQCD and LQCD calculations, as well as deductions from experiment. The goal of high-energy nuclear physics is to develop a thorough understanding of the QCD phase diagram.

1.3. QCD Phase Diagram

One of QCD's most spectacular predictions is the existence of a phase of nuclear matter where the quarks and gluons are deconfined, forming a plasma of mostly liberated quarks and gluons or QGP[54, 47] . The prediction of this deconfined state of matter at high temperatures and/or baryon-chemical potential followed from the work of Wilczek, Gross, and Politzer in describing asymptotic freedom, work for which they were awarded the Nobel Prize in physics in 2004. Based on theoretical calculations, the transition from hadronic matter to QGP is supposed to occur when the energy density of the medium is comparable to that inside a proton [66] .

Figure 1.2 shows LQCD calculations for the change in the energy density with temperature. The critical temperature is found to be $T_c = 173 \pm 15$ MeV and the critical energy

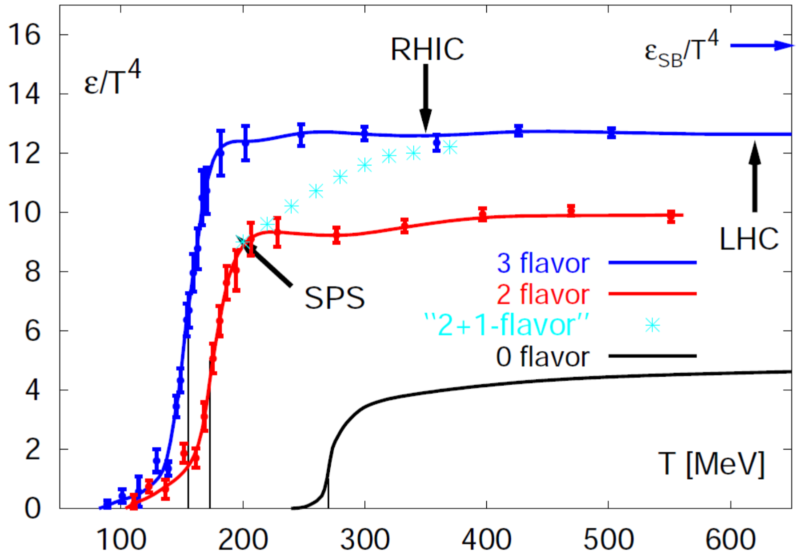

Figure 1.2.: Temperature dependence of the energy density, ε, scaled to T^4 for SPS, RHIC, and LHC energies. These calculations, based on LQCD, are done for different number of flavors. A rapid increase in $\varepsilon(T)$ is evident at $T \approx 160$ MeV which is the critical temperature. This increase occurs over a very narrow change in temperature and can be explained as a change in the degrees of freedom of their medium, signaling a phase transition [66].

density $\varepsilon = 0.7 \pm 0.3$ GeV/fm^3[87] . The change in the energy density, starting at $T = T_c \sim 160$ MeV, occurs over a very short range in temp of about 20 MeV. This sharp increase in the energy density can be interpreted as a change in the degrees of freedom of the medium, as it goes from a confined to a deconfined state. Assuming a hadronic gas of three very light pions (π^+, π^-, π^0), and therefore a total of three degrees of freedom. The equation of state for this hadronic gas phase becomes:

$$p = \frac{3\pi^2}{90}T^4 \tag{1.2}$$

for $T \gtrsim \frac{M\pi}{2}$ where p is the pressure, T is the temperature and M_π is the pion mass.

At higher temperatures, past T_c, we have a collection of quarks and gluons. The gluons provide eight colors and two spin degrees of freedom for $8 \times 2 = 16$ total degrees of freedom. For the quarks, we will have 2-3 flavors or n_f, with each flavor carrying an equal number of quarks and antiquarks (2 degrees of freedom). In addition, we have 2 degrees of freedom from spin and 3 from color. The total degrees of freedom contribution from quarks is $n_f \times 2 \times 2 \times 3 \times 7/8 = 21$-$32$ degrees of freedom. The 7/8 factor is introduced to account for the difference between Bose-Einstein and Fermi-Dirac statistics [42]. The degrees of freedom in this phase will be the sum from the contributions of the quarks and gluons, i.e,

$$16 + \frac{21}{2}n_f \tag{1.3}$$

The Equation of State for this deconfined phase of quarks and gluons is:

$$p = \frac{\pi^2}{90}(16 + \frac{21}{2}n_f) \tag{1.4}$$

We therefore find that there is a dramatic increase in the degrees of freedom going from the hadronic gas at $T < T_c$ to the deconfined quarks and gluons at $T > T_c$ [66].

While the change in the energy density is abrupt, the medium's pressure shows a smooth and gradual increase over the same range in temperature. The speed of sound given by:

$$c_s^2 = dP/d\epsilon \tag{1.5}$$

Therefore becomes very small over this temperature range ($c_s^2 \to 0$).

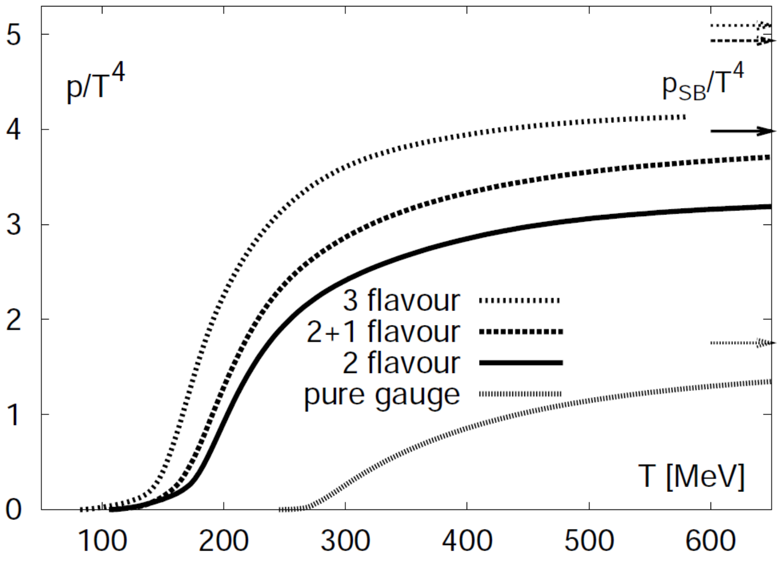

Figure 1.3.: Temperature dependence of the system's pressure, scaled to T^4. This is studied for the same number of flavors as Fig. 1.2. The scaled pressure dependence shows a smooth rise, rather than a sudden increase, at T_c [66].

The experimental verification of QGP at RHIC has been one of the defining moments of high energy nuclear physics. At RHIC energies, the QGP formed is now believed to be a strongly coupled QGP (sQGP) as opposed to the weakly coupled QGP (wQGP) which would be formed at much higher temperatures.

While there is an overwhelming body of experimental evidence for the formation of QGP at high T and/or μ_B, the transitions are not very well understood. Calculations based on Lattice QCD show that at high T and small μ_B ($\mu_B \to 0$), there is a smooth crossover transition from hadronic gas to QGP [46] . Theoretical calculations on the other hand show that at low T ($T \to 0$) and high μ_B, the system experiences a first-order phase transition [36, 40]. This would suggest that the first-order phase transtion line must end somewhere, and this would be the critical point of second order, and of the 3-D Ising universality class [68]. To theoretically determine the critical point, one would need to calculate the QCD partition function to establish the end of the first-order phase transtion line. These calculations have been hampered by several limitations in the capability of our current theoretical methods which leaves the experimental approach as the only viable way to establishing the location of the QCD Critical End Point (CEP) [106].

1.4. Relativistic Heavy Ion Collisions and BES

To experimentally probe the QCD phase diagram, we collide heavy ions at ultrarelativistic speeds. This allows us to recreate at a microscale the conditions of temperature and density necessary to induce the hypothesized phase transition from hadronic matter to QGP. The first facility capable of colliding heavy ions was the Alternating Gradient Synchotron (AGS) at Brookhaven National Laboratory. Later, the Super Proton Synchrotron at CERN was able to achieve heavy ion collisions at up to $\sqrt{s_{NN}} = 18$ GeV. The commisioning of the Relativistic Heavy Ion Collider in 2000 as the first heavy ion collider meant that researchers were now able to probe the phase diagram at even greater temperatures. RHIC makes use of the old AGS facility as an injector, allowing for even more intense beams to be collided. The newly commissioned Large Hadron Collider at CERN has ushered a new era in heavy ion studies, with energies of up to 5.5 TeV per nucleon pair attainable.

1.4.1. The Bjorken scenario of the space-time evolution of relativistic heavy-ion collisions in the central-rapidity region

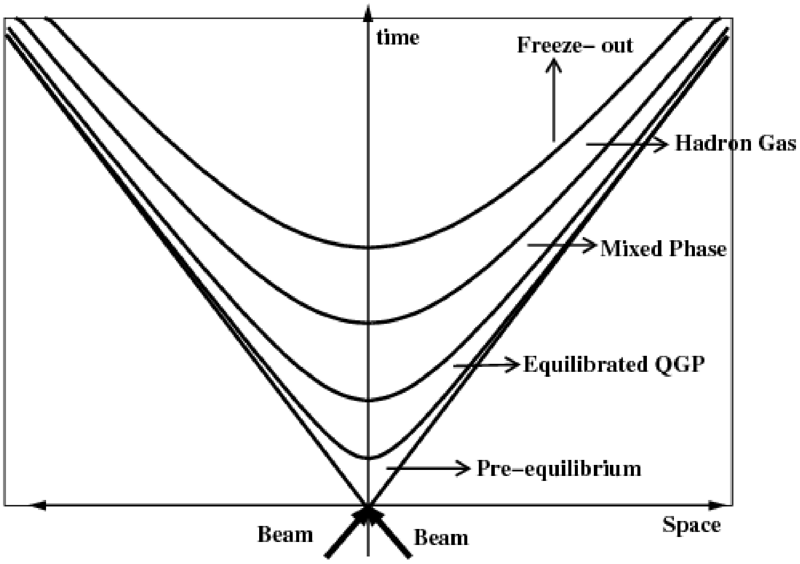

Figure 1.4.: Space-time evolution of a heavy ion collision at mid-rapidity.

Formation: As the ions are are accelerated to ultrarelativistic speeds, they are flattened, resembling pancakes, on the center of mass system as a result of Lorentz contraction. The crossing time for the two nuclei is very short and is given by:

$$\tau_{cross} = 2R/\gamma \tag{1.6}$$

where γ is the Lorentz factor and R is the nuclei radius [87].

After crossing, the two pancakes recede from each other at a speed c. The inital energy density of the receding colliding ions can be estimated to be about 1-10 GeV/fm^3, not taking into account any collisions from hadrons produced and assuming an initial time, T_0, of about 1 fm/c which can be viewed as the time it takes to establish the initial conditions. The formation time is comparable to the time-scale of the strong interaction. Once these initial conditions are established, they remain invariant under Lorentz transformation [42].

Thermalization: The particles produced will interact at the initial energy density, reaching thermal equilibrium in ($T_{therm} > T_0$) for T_{therm} ~5-10 fm/c. If thermal equilibrium is attained early, say at T_{therm}<1 fm/c (or $T_{therm} < T_0$), then the system will exhibit collective flow and there will be formation of QGP [66].

Hydrodynamic expansion: Once thermal equilibrium has been attained, the system undergoes a fluid-like expansion. The initial expansion will be longutidinal, due to the larger pressure gradient in that direction as opposed to the transverse. The time dependence of the energy density can be given as $\epsilon\ 1/t^n$ where $1 <= n <= 4/3$. The lifetime of the longutidinal hydrodynamic expansion is of the order of R, where R is the nuclei radius (~7 fm/c).

3-D Expansion: Following the longitudinal expansion is a relatively short-lived 3-D expansion (about T_0 ~ 0.3 fm/c) and cool-off ending in freeze-out. This is thought to occur when the mean-free-path, λ, is comparable to R or at an energy density of $\epsilon \sim 0.075\ GeV/fm^3$ [87]. Inelastic collisions end earlier than elastic collisions. The system will therefore undergo chemical freeze-out first which has the effect of fixing the total particle yield. Kinetic freeze-out then follows when elastic collisions end, thereby fixing the total momentum distribution of the particles [79].

1.4.2. BES

While theory has not been able to determine the exact location of the CEP, studies have been able to narrow it down to a region in T and μ_B that is accessible at RHIC collision energies [62, 101]. The basic premise is that at different collision energies, resulting hot and dense systems will traverse different trajectories as they cool down and eventually hadronize. Assuming ideal hydrodynamics, these trajectories are isentropic, and they trace a constant baryon per entropy ratio [33]. This means that one can experimentally search for the critical end point by colliding heavy ions at different collision energies–varying by small steps–and looking for key signatures that would denote a change in the reaction dynamics of the system.

The presence of a critical point would be characterized by a divergence in the correlation length, ξ, which can be thought of as a measure of the distance from the CEP ($\xi \rightarrow \infty$). This would in turn lead to an increase in fluctuations in the derivatives of thermodynamic functions. The divergences of the derived quantities act as powers or critical exponents of the correlation length[107].

It has been argued though that due to a phenomena known as critical slowing down, where the long wavelength dynamics are slowed down near the CEP, the growth of the correlation length is limited to $\xi_{freeze-out}$ ~ 3 fm [39]. This will have the effect of reducing the magnitude of related fluctuations which are proportional to $\xi_{freeze-out}$. For this reason, the higher moments of $\xi_{freeze-out}$ like the third order skeweness and fourth order kurtosis ($\xi^{9/2}_{freeze-out}$ and $\xi^{7}_{freeze-out}$ respectively) provide more sensitivity to the CEP [105]. On the other hand, the focusing effect as shown in Fig. 1.6, where the CEP behaves

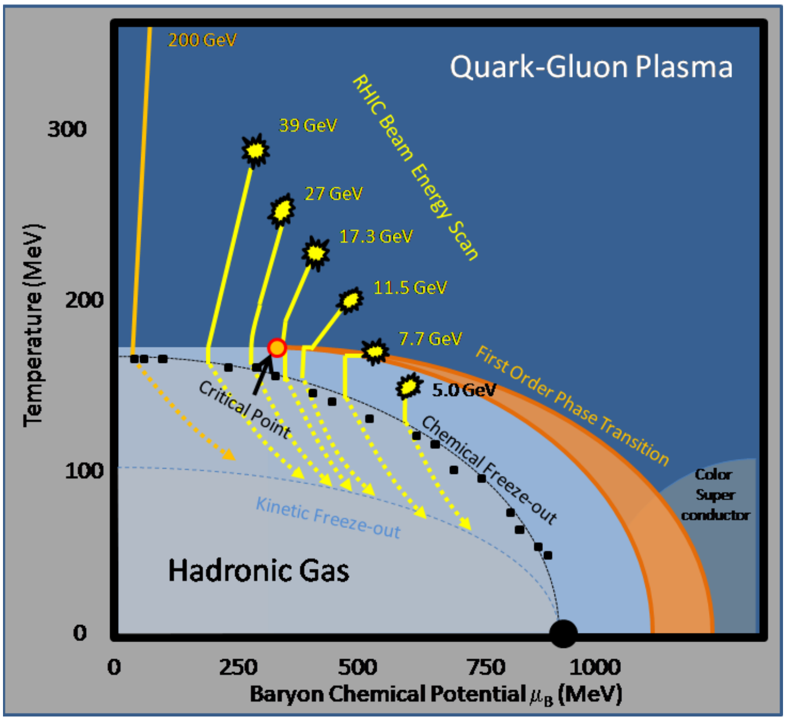

Figure 1.5.: The QCD phase diagram showing the energies so far undertaken by RHIC as part of the Beam Energy Scan program phase 1 (BES 1), as well as their theorized reaction trajectories (yellow curves). Black solid markers are estimates for the $T : \mu_B$ coordinates at freeze-out.

as an attractor of close by reaction trajectories, would provide an added advantage to experimentalists. This is because different collision energies with reaction trajectories close to the CEP will be drawn to it and therefore one does not necessarily need to narrow down to a specific collision energy so as to find the CEP.

1.5. Signatures of CEP

As mentioned above, event-by-event fluctuations in the derived quantities of thermodynamic observables as a function of temperature provide some of the direct evidence of the CEP and much of the experimental efforts have focused on different fluctuation measurements. Another set of indirect probes look for the expected softening of the Equation of State EoS in the vicinity of the CEP or for a first-order phase transition. The following discussion will focus more on a few of these probes.

1.5.1. Flow measurements

In heavy-ion collisions, spatial anistropy resulting from the overlap geometry of collision creates a pressure gradient which in turn leads to an azimuthal anisotropy in the momentum distribution of emitted particles. This azimuthal anisotropy in momentum-space is a manifestation of collective expansion behavior known as flow. Experimentally, we measure anisotropic flow from the distribution of momenta with respect to the reaction plane. This is characterized by the following form:

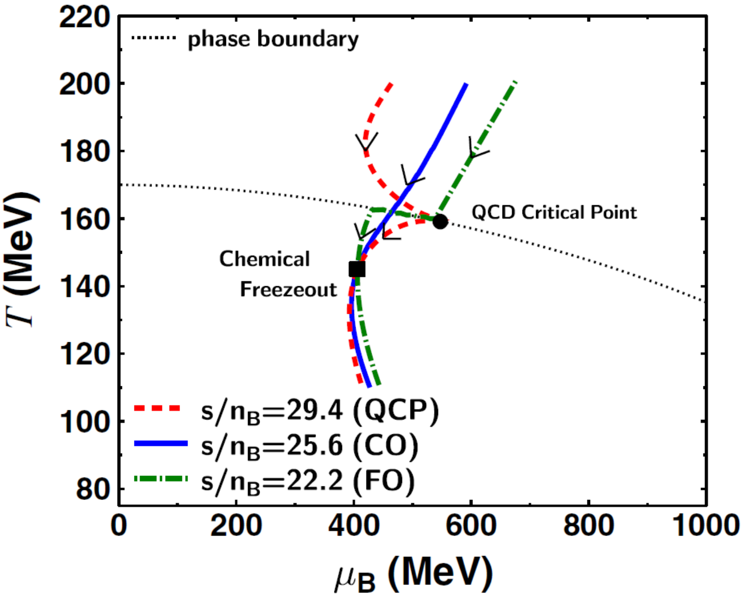

Figure 1.6.: Calculated trajectories in the $T:\mu_B$ phase space of QCD for the case of no CEP (solid line) and with a CEP (dotted and dashed-dotted) illustrating the focusing effect [32].

$$E\frac{d^3N}{d^3p} = \frac{1}{2\pi}\frac{d^2N}{p_T dp_T dy}(1+2\sum_{n=1}^{\infty}\upsilon_n cos[n(\varphi-\psi_{RP})]) \qquad (1.7)$$

Where E is the energy of the particle, N is the total number of particles, p is the momentum, p_T is the transverse momentum, y is the rapidity, φ is the azimuthal angle of the particle, and ψ_{RP} is the reaction plane angle. The Fourier decomposition yields the Fourier coefficients υ_n. υ_1 is known as the directed flow, υ_2 is the elliptical flow, and υ_3 is the triangular flow. As mentioned previously, a system going through a first-order phase transtion will show a softening of the EoS. Directed flow is formed early in the evolution of the systems since it arises from the pressure generated during the crossing of the two nuclei, and only affects particles in the forward and backward rapidity region [73]. Model calculations predict a dip in the υ_1 excitation function due to a reduction in directed flow as a result of the softening of the EoS, which could be used as a signature for first-order phase transition [98] .

Elliptic flow, which is formed much later than directed flow, has been especially well studied at RHIC as a signature of collective effects in the hot-dense medium and has been shown to be proportional to the initial spatial anisotropy [80, 88, 111]. Like directed flow, elliptic flow will also be sensitive to changes in the EoS which drive the dynamics of the system, and is expected to show non-monotonic behavior in its $\sqrt{s_{NN}}$ dependence as the system traverses a first-order phase transition [78].

Part of the appeal of elliptic flow coefficients is their sensitivity to transport coefficients such as the specific shear viscosity to entropy density ratio, η/s, that describe the dynamics of the system [82]. Flow measurements have been utilized to extract estimates of η/s by relativistic viscous hydrodynamic fits to experimental data [99, 53]. The η/s once extracted can be studied for its dependence on μ_B and T, to provide estimates for the location of the CEP in μ_B and T phase space. The QCD critical end point, as mentioned in section 1.3 is of the 3-D Ising model universality class, and as such will display critical properties that are characteristic of all physical systems of this universality class. It is therefore expected that η/s will show a similar trend in the transition from hadronic matter to QGP at a CEP as that shown by molecular systems of the same universality class. Molecular systems, such as those of helium, water and nitrogen for example, show that the η/s has a minimum at the critical point when plotted for its dependence in temperatue at fixed pressure values (one of which is the critical pressure where the minimum is observed) [55].

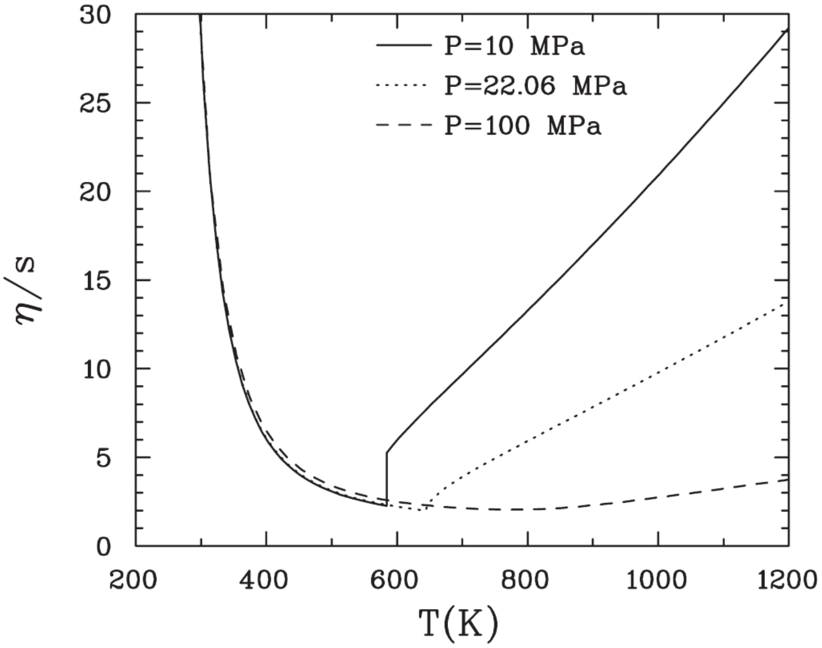

Figure 1.7.: η/s as a function of temperature for water. Each curve represents an isobaric curve, with the critical pressure at 22.06 MPa and the other two curves at 10 MPa and 100 MPa. A rapid change can be seen at the isobar below the critical pressure while η/s shows a minimum at the critical point [55].

Studies of the excitation function of $v_2(p_T)$ also indicate a flat dependence from $\sqrt{s_{NN}}$ 62-200 GeV which would suggest a softening of the EoS, as well as relatively small values of average η/s over this range in $\sqrt{s_{NN}}$ [81].

1.5.2. Measurements of the system size at freeze-out

One would expect that an increase in collision energy would lead to a monotonic increase in the lifetime of the system as well as its emission duration. A system evolving through a mixed phase at lower energy however, or traversing a critical point, would show dramatic changes in the excitation functions of its system size in space and time. For example, due to the reduced pressure gradient, $c_s^2 \sim 0$ and the system would show a reduced final geometric transverse size but an enhanced emission duration as the system slows down [75, 97]. Measurements of the collision energy and system size dependence of emission sources can therefore help locate the CEP or the onset of deconfinement.

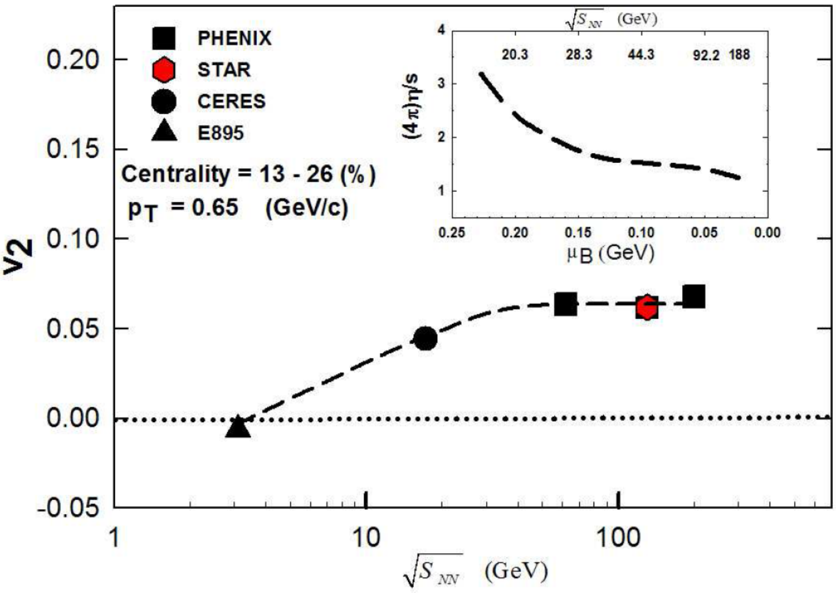

Figure 1.8.: The $v_2(p_T)$ excitation function showing a flat dependence for $\sqrt{s_{NN}} = 62$-200 GeV. The inset shows the $(4\pi)\eta/s$ dependence on μ_B [81].

1.5.3. Turn-off of hydrodynamic-driven final-state effects

The small systems of $p+p$ and $p(d)+A$ have routinely been applied in heavy-ion studies to provide benchmarks for expected signatures of QCD matter created in the $A+A$ systems [8, 13]. The elementary collisions of $p+p$ allow for the characterization of particle productions processes in the abscence of both initial and final-state effects while the asymmetric $(d)p+A$ systems allow for the separation of initial and final state effects. It is expected that the $(d)p+A$ systems would show the same initial state effects as $A+A$ collisions but collective effects will be largely absent since the systems are not large enough and are too short-lived for the formation of QGP [100, 21, 13].

Recent results for high-multiplicity $p+p$ and $(d)p+A$ collision systems where these small systems are seen to exhibit signatures usually associated with collective phenomena in $A+A$ systems has led to a revival of interest in them, beyond their use as calibration tools for $A+A$ collisions. These results, and the new challenges they present are discussed in this section.

Ridge structure

Two particle angular correlations have been a very useful tool in the study of particle production and collective effects in heavy-ion collisions [4, 28, 6, 2]. Typically, it involves building distributions of the relative separation of two particles in ϕ and η (i.e., $\Delta\phi$, $\Delta\eta$) where ϕ is the azimuthal angle and η is the pseudorapidity defined as:

$$\eta = -ln(tan(\theta/2)) \tag{1.8}$$

with θ, the polar angle, defined in the counter-clockwise beam direction [52].

In minimum-bias $p+p$ and $p(d)+A$ collision systems, the "near-side" ($\Delta\phi \approx 0$; $\Delta\eta \approx 0$) is dominated by a large peak attributed to jets. Jets are a stream of hadrons contained in a narrow cone, resulting from hard scattering processes within the medium. The "away-side" ($\Delta\phi \approx \pi$) also show similar structure, from fragmentation in the recoiling jets and momentum conservation. This peak is seen to be broader in $\Delta\eta$ due to longitudinal momentum distribution [2].

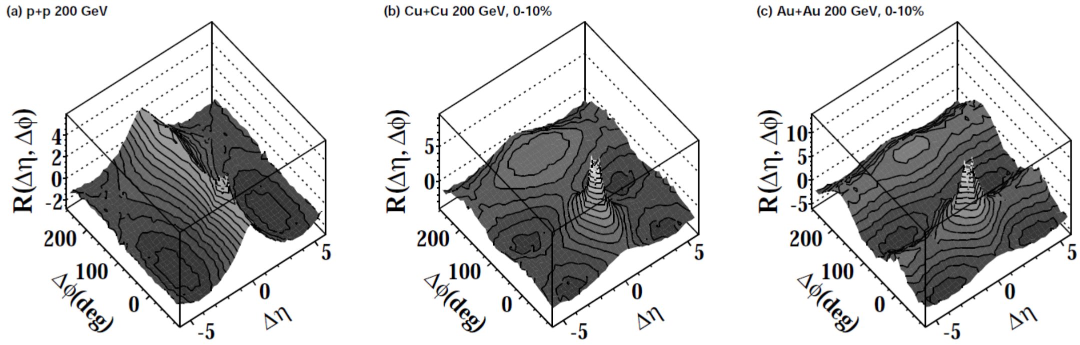

Figure 1.9.: A comparison of two-particle angular correlations for (a) $p+p$, (b) $Cu+Cu$, and (c) $Au+Au$ collision systems at $\sqrt{s} = 200$ GeV. The $p+p$ collisions are minimum bias while the $Cu+Cu$ and $Au+Au$ collisions are selected for the most central 0–10% [28].

In addition to the jet-like features, the $A+A$ systems are also found to have broader ridge-like structures that extend over $\Delta\eta$ in the near-side and away-side. The long-range structures are unrelated to the jet-like effects and have been attributed to flow [28]. Recently, similar structures have also been reported in high-multiplicity $p+p$, $p+Pb$, and $d+Au$ collisions [3, 16, 76].

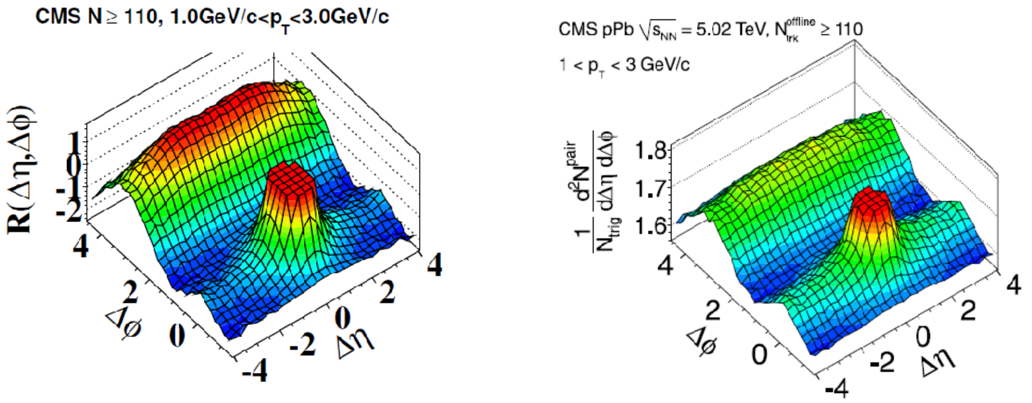

(a) Ridge structures for high-multiplicity $p+p$ collisions at $\sqrt{s_{NN}} = 5.02$ TeV [76].

(b) Ridge structures for high-multiplicity $p+Pb$ collisions at $\sqrt{s} = 7$ TeV [52].

Figure 1.10.: Ridge structures as seen at $\Delta\phi \approx 0$ and $\Delta\phi \approx \pi$ for a wide range in $\Delta\eta$

In $A+A$ collisions, the long-range (in $\Delta\eta$) correlations can be characterized using the components of a Fourier decomposition to the distribution as given by the expression:

$$\frac{dN^{pairs}}{d\Delta\phi} \propto 1 + \sum 2v_{n\Delta}(p_T^a p_T^b) cos(n\Delta\phi) \tag{1.9}$$

where N^{pairs} is the total number of pairs, $v_{n\Delta}$ is the n^{th} harmonic order coefficient, and p_T^i are the transverse momenta of the particles in the pair.

Using the second Fourier coefficient, v_2, to quantify the magnitude of elliptic flow, it has been found that the $d + Au$ and $p + Pb$ systems both show a strong v_2 signal, as well as mass-ordering for identified particles in the v_2 dependence on p_T. Mass-ordering comes about from the greater influence of flow on the momenta of heavier particles [45].

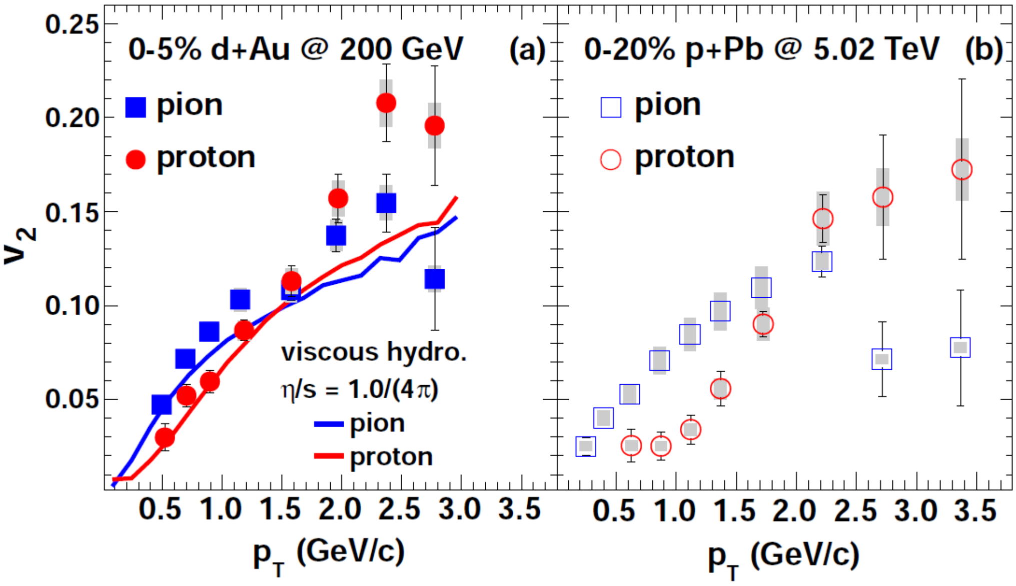

Figure 1.11.: The measured $v^2(p_T)$ for identified particles at (a) RHIC for $d + Au$ at $\sqrt{s}$ = 200 GeV and (b) LHC $p+Pb$ at $\sqrt{s} = 5.02$ TeV. They both show a strong elliptic flow signature as well as mass-ordering [17].

While these results can be explained using the viscous hydrodynamic model (for example, see [17, 3]), alternative models that argue for inital-state effects have also been proposed. The Color Glass Condensate (CGC) model, for instance, proposes that the observed effects are as a result of quantum interference resulting from gluon saturation at very high parton densities [58, 59]. To provide for model constraints and help establish the role of final-state effects in th evolution of small asymmetric systems, one can utilize a different probe that is known to be sensitive to hydrodynamic-like final-state effects. One such probe is the size in space and time at freeze-out of the particle emitting system. The dependence on the collision geometry and transverse mass of the size of the system at freeze-out is well studied for $A + A$ collisions, and is known to exhibit characteristic patterns that can be attributed to hydrodynamic-driven final-state effects [85, 22, 23].

1.5.4. Interferometry

Hanbury-Brown Twiss is a technique of intensity interferometry that utilizes quantum interference between identical particles to measure the size in space and time, as well as the shape, of the hot and dense systems formed from heavy-ion collisions. It measures the so called region of homogeneity–an emission region for correlated particles with the same transverse momentum–at freeze-out and has been extensively used in studies of heavy-ion collisions [22, 15, 1]. HBT does not only reveal the geometry of the particle emitting system but also describes the influence of space-momentum correlations resulting from collective flow effects on the final shape and size at freeze-out. Using the HBT method to obtain detailed measurements of the extent in space and time of pion emission sources for different beam energies and collision systems, this thesis will focus on two objectives:

1. Obtaining a comparison of the final system size dependence on collision geometry and expansion dynamics for $d+Au$ and $Au+Au$ collision systems to determine the influence of hydrodynamic driven final-state effects in small asymmetric systems.
2. An analysis of the excitation functions of the final system size and derived quantities in search of the QCD critical point and/or the onset of deconfinement.

2. HBT theory

The first application of two particle intensity interferometry was in radio-astronomy by Hanbury-Brown and Richard Twiss in the 1950's. Using mirrors to collect stellar light into photomultiplier tubes, they were able to observe an interference pattern analogous to the interference patterns of the Young's experiment. Unlike amplitude interferometry, the method now commonly known as Hanbury-Brown Twiss interferometry (HBT) is based on the correlation effects from fluctuations in the measured intensities of a beam of particles at two detectors. These intensity fluctuations encode information about the size of the source and are therefore useful in the imaging of stellar objects [69]. In the late 1950's Goldhaber et al. independently applied the same technique of intensity interferometry to particle physics. In the process of comparing the mass distributions of like and unlike charge pion-pairs, they observed that there was an angular correlation in the same-charge pion pairs. As identical bosons, the same-charge pion pairs are subject to Bose-Einstein statistics and therefore an enhancement will be observed at small relative momentum [63].

2.1. HBT model

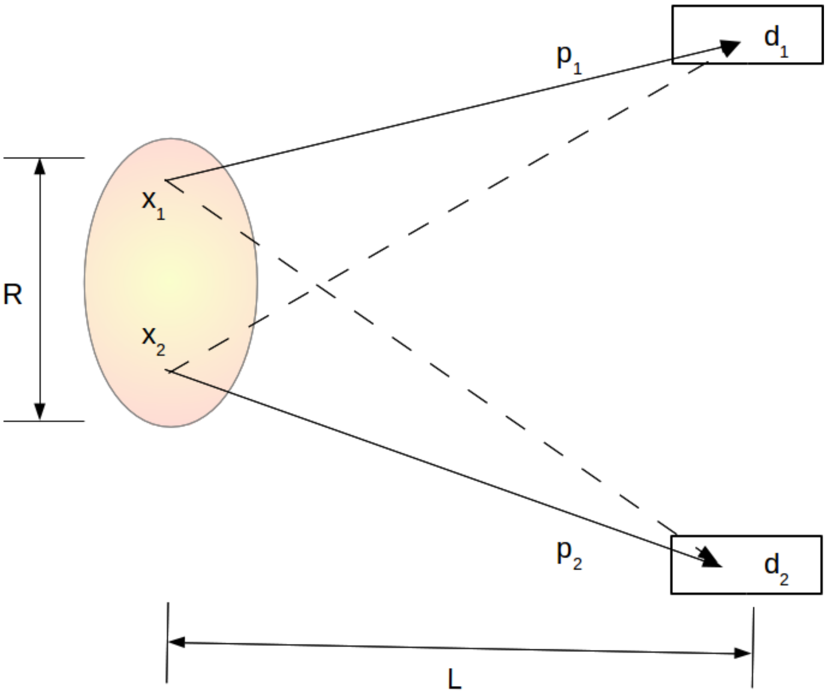

Figure 2.1.: Illustration of an intensity interferometry experiment.

Consider two random source, X_1 and X_2 separated by a distance R. The two sources emit identical particles independently (at x_1 and x_2 respectively), and these particles are then picked up by two detectors d_1 and d_2 a distance L away from the sources and separated by a distance h. The probability amplitude for the detection of the two identical particles is:

$$\psi_{12} \;=\; \frac{1}{\sqrt{2}}\left\{Me^{-ip_1(d_1-x_1)}e^{-ip_2(d_2-x_2)} \pm Ne^{-ip_1(d_2-x_1)}e^{-ip_2(d_1-x_2)}\right\} \tag{2.1}$$

Where M is $A(p_1, d_1)A(p_2, d_2)$ and N is $A(p_1, d_2)A(p_2, d_1)$

The probability density of detecting two particles with momentum p_1 and p_2 for a normalized space-time distribution of the emission source $\rho(x)$ is given by:

$$P_2(p_1, p_2) \;=\; P(p_1)P(p_2)\int d^4x_1 d^4x_2 |A(p_1, p_2)|^2 \rho(x_1)\rho(x_2) \;=\; P(p_1)P(p_2)\left[1 \pm |\tilde{\rho}(q)|^2\right] \tag{2.2}$$

where $\rho(q) \;=\; \int d^4x\rho(x)e^{ix(p_2-p_1)}$ is the Fourier transform of $\rho(x)$.

The single particle probability density is:

$$P(p) \;= \int d^4x\rho(x)|\psi(p)|^2 \tag{2.3}$$

where $\psi(p) \;=\; A(p, d)e^{-ip(d-x)}$.

The two-particle correlation can therefore be expressed in the form:

$$C_2(p_1, p_2) \;=\; \frac{P_2(p_1, p_2)}{P(p_1)P(p_2)} \;=\; 1 \pm |\tilde{\rho}(q)|^2 \tag{2.4}$$

Assuming the source density has a Gaussian profile,

$$\rho(x) \;=\; \frac{1}{4\pi^2 R^4} exp\left(-\frac{x^2}{2R^2}\right) \tag{2.5}$$

with R as the Gaussian width, and with its Fourier transform as:

$$\rho(q) \;=\; \frac{1}{4\pi^2 R^4} exp\left(-\frac{q^2 R^2}{2}\right) \tag{2.6}$$

which is also a Gaussian distribution, the correlation function can be expressed in the form:

$$C_2(p_1, p_2) \;=\; 1 \pm e^{-q^2R^2} \tag{2.7}$$

The above derivation assumes a static extended source. While this might be a good approximation for stellar objects, the rapidly expanding systems produced in heavy-ion collisions require a description that takes into account the resulting space-momentum correlations.

2.2. HBT in dynamic systems

For heavy-ion collisions, the behavior of pions produced can be described by the Klein-Gordon equation for the pion Heisenberg field, $\phi(x)$, as [65]:

$$(\Box + m_\pi^2)\phi(x) = \hat{J}(x) \tag{2.8}$$

$\hat{J}(x)$ is the nuclear current operator while m_π is the pion rest mass. This equation is not easy to deal with since $\hat{J}(x)$ is coupled to $\phi(x)$, the pion field. However, we can make some presumptions that allow us to make estimates for $\hat{J}(x)$. For high multiplicity nucleus-nucleus collisions, the expectation is that at chemical freeze-out, the production of pions is going to be small as compared to the nucleon number and therefore $\hat{J}(x)$ remains mostly unchanged by the emission [65].

This approximation allows us to replace $\hat{J}(x)$ by its expectation value $J(x)$ which is a space-time function. The solution for the equation giving the final pion state is then the coherent state $|J\rangle$, i.e.,

$$|\phi(x)\rangle = |J\rangle \tag{2.9}$$

$|J >$ has several properties, the most relevant to this discussion been that it is an eigenstate of the annihilation operator [93].

$$\hat{a}(\vec{p})|J\rangle = \ i\tilde{J}(\vec{p})|J\Big\rangle \tag{2.10}$$

where the on-shell Fourier transform of $J(x)$, $\tilde{J}(\vec{p})$, is defined as:

$$\tilde{J}(\vec{p}) = \int \frac{d^4x}{\sqrt{(2\pi)^3 2E_p}} exp[i(E_p t - \vec{p}.\vec{x})]J(x) \tag{2.11}$$

$J(x)$ for a classical current can be thought of as a collection of independent source currents with a position defined as x_i and momenta p_i, i.e.,

$$J(x) = \sum e^{i\phi_i} e^{-ip_i.(x-x_i)} J_0(x - x_i) \tag{2.12}$$

If ϕ_i are random phases, then the source is chaotic. Its Fourier transform on-shell is given by:

$$\tilde{J}(\vec{p}) = \sum e^{i\phi_i} e^{ip_i.x_i} \tilde{J}_0(p - p_i) \tag{2.13}$$

where $\tilde{J}_0(p - p_i)$ is the Fourier transform of $J_0(x)$, the individual source currents and is described as:

$$\tilde{J}_0(p - p_i) = \int \frac{d^4x}{\sqrt{(2\pi)^3 2E_p}} e^{i(p-p_i).x} J_0(x) \tag{2.14}$$

Based on the solution for the final pion state, the probability of producing a single particle from position x with momentum p can be described by the equation:

$$P_1(\vec{p}) = E\frac{dN}{d^3p} = E\Big\langle J|a^\dagger(\vec{p})a(\vec{p})|J\Big\rangle \tag{2.15}$$

This single-particle distribution is normalized to the average number of particles per event, $\langle N\rangle$,

$$\int \frac{d^3p}{E} P_1(p) = \langle N\rangle \tag{2.16}$$

The probability of producing a pair of particles is given by:

$$P_2(\vec{p}_1,\vec{p}_1) = E_1E_2\frac{dN}{d^3p_1d^3p_2} = E_1E_2\left\langle J|a^\dagger(\vec{p}_1)a^\dagger(\vec{p}_2)a(\vec{p}_1)a(\vec{p}_2)|J\right\rangle \tag{2.17}$$

With the distribution normalized to the average number of pairs per event, $\langle N(N-1)\rangle$ [71]. The two-particle probability distribution can be expanded using the generalized Wick theorem so that,

$$P_2(\vec{p}_1,\vec{p}_2) = \frac{\langle N(N-1)\rangle}{\langle N\rangle^2}(P_1(\vec{p}_1)P_1(\vec{p}_2) \pm |\bar{S}(\vec{p}_1,\vec{p}_2)|^2).\bar{S}(\vec{p}_1,\vec{p}_2) \tag{2.18}$$

is a covariant quantity defined as:

$$\bar{S}(\vec{p}_1,\vec{p}_2) = \sqrt{E_1E_2\left\langle a^+_{\vec{p}_1}a_{\vec{p}_2}\right\rangle} \tag{2.19}$$

and whose Fourier transform is the emission function [49],

$$\bar{S}(\vec{p}_1,\vec{p}_2) = \tilde{S}(\vec{q},\vec{K}) = \int d^4xe^{-iq.x}S(x,K) \tag{2.20}$$

The off-shell average momentum of the pair is defined as:

$$\vec{K} = \frac{1}{2}(\vec{p}_1+\vec{p}_2) \tag{2.21}$$

where $K^0 = \frac{1}{2}(E_1+E_2)$ and $p_i^0 = E_i = \sqrt{m^2+\vec{p}_i^2}$. The off-shell relative pair momentum is:

$$q = (p_1 - p_2) \tag{2.22}$$

The mass-shell constraint Since q and K are off-shell, they satisfy the orthogonality relationship [71]:

$$q.K = p_1^2 - p_2^2 = 0 \tag{2.23}$$

In the same manner, the single-particle distribution can be described in terms of the Wigner density emission function:

$$P_1(\vec{p}) = E\frac{dN}{d^3p} = \int d^4xS(x,K) \tag{2.24}$$

The correlation function can be described as the ratio of the two-particle probability distribution to the one-particle probability distributions,

$$C(\vec{p}_1,\vec{p}_2) = \Pi\frac{P_1(\vec{p}_1,\vec{p}_2)}{P_1(\vec{p}_1)P_2(\vec{p}_2)} = \Pi\frac{\left\langle J|a^\dagger(\vec{p}_1)a^\dagger(\vec{p}_2)a(\vec{p}_1)a(\vec{p}_2)|J\right\rangle}{\langle J|a^\dagger(\vec{p}_1)a(\vec{p}_1)|J\rangle\,\langle J|a^\dagger(\vec{p}_2)a(\vec{p}_2)|J\rangle} \tag{2.25}$$

Π is the normalization given by: $\frac{\langle N\rangle^2}{\langle N(N-1)\rangle}$

Using the generalized Wick's theorem expansion in equation 2.18 and substituting with equations 2.17 and 2.24, we get:

$$C(\vec{p}_1,\vec{p}_2) = \Pi \frac{\left\langle J|a^{\dagger}(\vec{p}_1)a(\vec{p}_1)|J\right\rangle \left\langle J|a^{\dagger}(\vec{p}_2)a(\vec{p}_2)|J\right\rangle + \left\langle J|a^{\dagger}(\vec{p}_1)a(\vec{p}_2)|J\right\rangle \left\langle J|a^{\dagger}(\vec{p}_2)a(\vec{p}_1)|J\right\rangle}{\langle J|a^{\dagger}(\vec{p}_1)a(\vec{p}_1)|J\rangle \; J \, \langle|a^{\dagger}(\vec{p}_2)a(\vec{p}_2)|J\rangle} \tag{2.26}$$

$$= \; 1 + \frac{|\left\langle J|a^{\dagger}(\vec{p}_1)a(\vec{p}_2)|J\right\rangle|^2}{\langle J|a^{\dagger}(\vec{p}_1)a(\vec{p}_1)|J\rangle \, \langle J|a^{\dagger}(\vec{p}_2)a(\vec{p}_2)|J\rangle} \tag{2.27}$$

$$= \; 1 + \frac{|\int d^4xS(x,K)e^{iq.x}|^2}{\int d^4xS(x,p_1)\int d^4xS(x,p_2)} \tag{2.28}$$

Assuming that we have a smooth momentum dependence for the emission function, i.e., that the single-particle distributions have an exponential dependence on the energy, we can put K on shell and make the estimate $K^0 \backsimeq E_K = \sqrt{m^2+K^2}$, setting $\vec{p}_1 = \vec{p}_2 = \vec{K}$ for small q. This allows us to replace the form in equation 2.26 with,

$$C(\vec{q},\vec{K}) = 1 + \frac{|\int d^4xS(x,K)e^{iq.x}|^2}{|\int d^4xS(x,K)|^2} \tag{2.29}$$

Consequently, measuring the correlation function $C(\vec{q},\vec{K})$, we are able to study the emission function, $S(x,K)$, which carries information about the space-time extent of the system.

Estimating to a Gaussian The emission function can be approximated to a Gaussian and written as [50]:

$$S(x,K) \; = \; N(\overrightarrow{K})S(\bar{x}(\overrightarrow{K}),K)\,exp\left[-\frac{1}{2}\tilde{x}^{\mu}(\overrightarrow{K})B_{\mu\nu}(\overrightarrow{K})\tilde{x}^{\nu}(\overrightarrow{K})\right] + \delta S(x,K) \tag{2.30}$$

where $\bar{x}_{\mu}(\overrightarrow{K}) = \langle x_{\mu}\rangle = x_{\mu} - \bar{x}_{\mu}(\overrightarrow{K})$ and $(B^{-1})_{\mu\nu}(\overrightarrow{K}) = \langle\tilde{x}_{\mu}\tilde{x}_{\nu}\rangle$. $\langle...\rangle$ denote averages and the space-time coordinates, $\tilde{x}^{\mu}$, are defined with respect to the emission center, $\bar{x}(K)$. $\delta S(x,K)$, which is a correction term, is neglected since it has no influence on the half-width of the correlation function from which we extract the spatial-temporal information of the source [109].

Introducing this form to equation 2.29 gives:

$$C(\overrightarrow{K},\vec{q}) \; = \; 1 + exp\left[-q^{\mu}q^{\nu}\,\langle\tilde{x}_{\mu}\tilde{x}_{\nu}\rangle\,(\overrightarrow{K})\right] \tag{2.31}$$

Where the space-time variances $\langle\tilde{x}_{\mu}\tilde{x}_{\nu}\rangle$ have only a $\overrightarrow{K}$ dependence. These are the so called lengths of homogeneity, that is, they describe the source-width emitting particles with momentum $\overrightarrow{K}$. Therefore the HBT measurements obtained are comparable to the actual dimensions of the emission sources only if it is static since then there is an abscence of any space-momentum correlations that tend to “shrink” the actual size as illustrated in Figure 2.2.

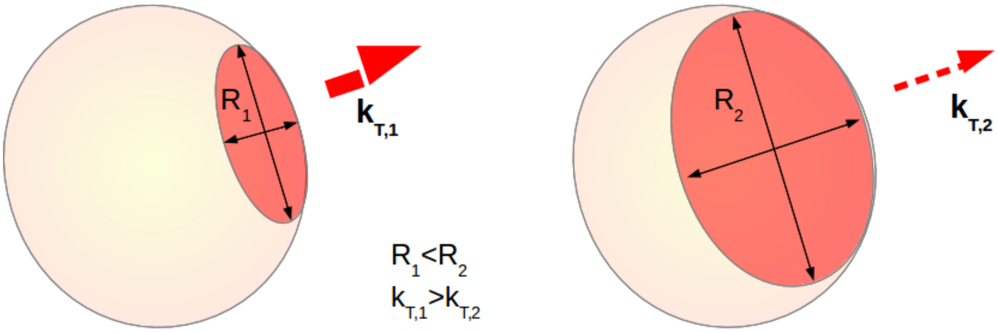

Figure 2.2.: Lengths of homogeneity as measured using HBT. The size of the homogeneity region is dependent on the average momenta of the pair. Therefore studying the dependence of HBT radii with respect to k_T can provide insight into the dynamics of the system.

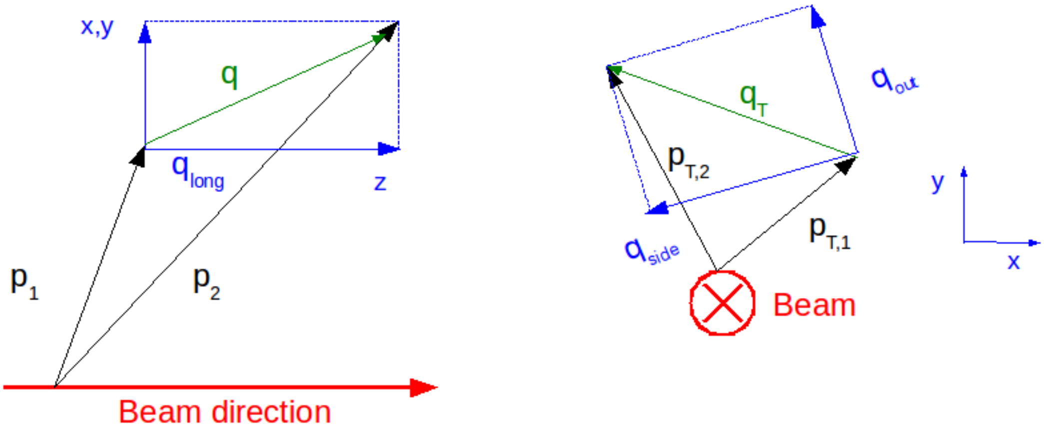

Figure 2.3.: Schematic diagram of the Bertsch-Pratt 3D parameterization of q.

2.2.1. Bertsch-Pratt parameterization

The onshell approximation allows us to solve for q^0 so that

$$q^0 = \overrightarrow{\beta}.\overrightarrow{q} \tag{2.32}$$

where $\beta \approx \frac{\overrightarrow{K}}{E_K}$
and therefore:

$$q^0 = \beta_x q_x + \beta_y q_y + \beta_z q_z \tag{2.33}$$

thereby eliminating the temporal component from equation 2.31. Note that the approximation $\beta \approx \frac{\overrightarrow{K}}{E_K}$ is only valid where $|\overrightarrow{q}| << E_K$ [50]. The Besch-Pratt parameterization has been adopted as a standard in HBT analysis. In this parameterization, q is decomposed into its three components on the Cartesian coordinate system. These are *out*, *side*, and *long* where *long* is defined in the beam direction or z, *out* is defined parallel to the average transverse momentum of the pair, k_T,

$$k_T = (\frac{p_T^1 + p_T^2}{2}) \tag{2.34}$$

p_T^i is the transverse momentum of a particle in the pair.
and *side* is perpendicular to both *long* and *out*.
We fit the correlation function in 2.31 with the form:

$$C(\overrightarrow{K}, \vec{q}) = 1 + exp\left[-\sum_{i,j} R_{ij}^2(\overrightarrow{K}) q_i q_j\right] \tag{2.35}$$

Here, i, j are *out*, *side*, and *long* and R_{ij}^2 can be expressed in term of the variances as:

$$R_{ij}^2(\overrightarrow{K}) = \left\langle(\tilde{x}_i - \beta_i\tilde{t})(\tilde{x}_j - \beta_j\tilde{t})\right\rangle - \left\langle\tilde{x}_i - \beta_i\tilde{t}\right\rangle\left\langle\tilde{x}_j - \beta_j\tilde{t}\right\rangle \tag{2.36}$$

Rewriting equation 2.35:

$$C(\overrightarrow{q}, \overrightarrow{K}) = 1 \pm \lambda exp\left[-q_{out}^2 R_{out}^2(\overrightarrow{K}) - q_{side}^2 R_{side}^2(\overrightarrow{K}) - q_{long}^2 R_{long}^2(\overrightarrow{K}) - X\right] \tag{2.37}$$

$$X = 2q_{out}q_{side}R_{os}^2(\overrightarrow{K}) - 2q_{out}q_{long}R_{ol}^2(\overrightarrow{K}) - 2q_{side}q_{long}R_{sl}^2(\overrightarrow{K}) \tag{2.38}$$

Here we introduce λ, the chaoticity parameter which quantifies coherence effects and the contribution to the correlation function of secondary pions from long-lived resonance decays [65]. λ is two for a fully chaotic source and one for a fully coherent source. Assuming a system with azimuthal symmetry, the correlation function will have cylindrical symmetry so that $q_{side} = -q_{side}$ and we can eliminate the two cross terms R_{os}^2 and R_{sl}^2 which both go to zero. The function then reduces to:

$$C(\overrightarrow{q}, \overrightarrow{K}) = 1 \pm \lambda exp\left[-q_{out}^2 R_{out}^2(\overrightarrow{K}) - q_{side}^2 R_{side}^2(\overrightarrow{K}) - q_{long}^2 R_{long}^2(\overrightarrow{K}) - T\right] \tag{2.39}$$

with T as $2q_{out}q_{long}R_{ol}^2(\overrightarrow{K})$.
and where,

$$R^2_{out}(\overrightarrow{K}) \;=\; \left\langle (\tilde{x} - \beta_T \tilde{t})^2 \right\rangle \tag{2.40}$$

$$R^2_{side}(\overrightarrow{K}) \;=\; \left\langle \tilde{y}^2 \right\rangle \tag{2.41}$$

$$R^2_{long}(\overrightarrow{K}) \;=\; \left\langle (\tilde{z} - \beta_l \tilde{t})^2 \right\rangle \tag{2.42}$$

$$R^2_{ol}(\overrightarrow{K}) \;=\; \left\langle (\tilde{x} - \beta_T \tilde{t}) \right\rangle \left\langle (\tilde{z} - \beta_l \tilde{t}) \right\rangle \tag{2.43}$$

As can be seen from these expressions of the lengths of homogeneity, we are able to extract both space and time information about the emitting system from HBT measurements.

In this analysis, the Longitudinal co-moving system (LCMS) was selected as the reference frame. In this frame, $\overrightarrow{q}$ is defined on the rest frame of the pion pair. This means that the reference frame is different for each pair. Since $p^1_z + p^2_z \;=\; 0$ in the LCMS frame, the relative energy is zero and the magnitude of the relative momentum is Lorentz-invariant [94]. Choosing the LCMS as the reference frame allows for the elimination of the remaining cross-term in equation 2.39 due to reflection symmetry along z at midrapidity.

2.2.2. Analytical parameterization: Blastwave model

The blastwave model provides a link between the measured HBT parameters and physical observables of the system at freeze-out. It makes several assumptions in its application [96]:

(1) The model approximates a high-energy expanding source as an extended cylindrical source, dominated by a boost-invariant longitudinal flow.

(2) At freeze-out, the particles all decouple at the same time, and this happens instantaneously ($\triangle\tau \;=\; 0$).

Based on the blastwave model, we can derive expressions for the measured HBT radii, in the LCMS frame, relating them to physical observables of the system [51, 72].

$$R^2_{out} \;=\; \frac{R^2_{geom}}{1 + \frac{m_T}{T} v^2} + \frac{1}{2}\left(\frac{T}{m_T}\right)^2 \beta^2_T \tau^2_0 \tag{2.44}$$

$$R^2_{side} \;=\; \frac{R^2_{geom}}{1 + \frac{m_T}{T} v^2} \tag{2.45}$$

$$R^2_{long} \;=\; \tau^2 \frac{T}{m_T} \frac{K_2(\frac{m_T}{T})}{K_1(\frac{m_T}{T})} \tag{2.46}$$

Where R_{geom} is the geometrical size of the system in the transverse, T is the temperature of the system at freeze-out, v is the transverse flow, β_T the pair's transverse velocity, and τ_0 the expansion time of the system. K_2 and K_1 are modified Bessel functions and m_T is the transverse mass defined as:

$$m_T \;=\; \sqrt{k_T + m_\pi} \tag{2.47}$$

Since R^2_{side} only encodes the spatial information about the system while R^2_{out} carries information about the transverse size as well as the emission duration of the system,

$R_{out}^2 - R_{side}^2 \propto \Delta\tau^2$ and both $R_{out}^2 - R_{side}^2$ and the ratio R_{out}/R_{side} have traditionally been used as proxies for the emission duration.

2.3. Final State Interactions (FSI)

The derived equation 2.39 for the two-particle correlation function is made with the assumption that the particles do not experience any final state interactions. In reality, that is hardly the case. There are two possible sources of FSI influence on the Bose-Einstein signal: The strong interaction and the Coulombic interactions.

2.3.1. FSI contribution from strong interactions

The contribution of the strong force to the FSI in proton-proton correlation functions has been shown to be significant, providing an attractive force that counteracts the Coulombic repulsion of same-charge pairs [43]. In the case of two-pion correlations, the range of the repulsive s-wave interaction, ~0.2 fm, is much smaller than the average interaction distance of pion pairs (about 5 fm) and therefore the effects of the strong force are negligible in pion-pion correlations [44]. For this reason, strong interactions were not considered in the corrections applied in the study detailed here.

2.3.2. Coulomb interactions

The Coulomb effect plays a significant role in pion-pion interactions, especially at small q. Understanding these interactions and correcting for them is an important part of the analysis of Bose-Einstein correlations. At small q, Coulomb interactions between the pions in a pair have the effect of accelerating them relative to each other, consequently decreasing the same-charge pion-pair distribution at small q. This is observed as a dip in the correlation function.

Estimation of the Coulomb interaction

In the center-of-mass (CM) system, the Schroedinger equation for the Coulomb wave functions is given as [37]:

$$(\tfrac{\nabla^2}{2m} - E + \tfrac{e^2}{r})\psi_c(\overrightarrow{q}, \overrightarrow{r}) \;=\; 0 \tag{2.48}$$

Where q is the relative momentum of the pair, r is their position, ψ_c is their relative wave function, and E describes the particle energy in the CM frame where $E \;=\; q^2/2m_{red}$ and m_{red} is the reduced mass, $(m_1 m_2/m_1 + m_2)$.

In the CM frame, the solution to this equation is [94]:

$$\phi(\overrightarrow{q}, \overrightarrow{r}) \;=\; \Gamma(1 + i\gamma)e^{-\pi\gamma/2}e^{iqr}\Phi(-i\gamma; 1; iqr - i\overrightarrow{q}.\overrightarrow{r}) \tag{2.49}$$

Here, $\gamma \;=\; me^2/q$ and Φ is the confluent hypergeometric function.

The symmetrized Coulomb wave function is then:

$$\psi_r(\overrightarrow{q}, \overrightarrow{r}) \;=\; \frac{1}{\sqrt{2}}(\psi_c(\overrightarrow{q}, \overrightarrow{r}) + \psi_c(\overrightarrow{q}, -\overrightarrow{r})) \tag{2.50}$$

and the strength of the Coulomb interaction can be calculated from:

$$P_c(\overrightarrow{p}_1, \overrightarrow{p}_2) \; = \; \frac{1}{2} \int d^3 r \rho(\overrightarrow{r}) |\psi_r(\overrightarrow{q}, \overrightarrow{r})|^2 \tag{2.51}$$

This expression would normally be integrated numerically but since the source function is not known beforehand, one has to make approximations.

One approximation is based on the assumption that the pair of identical particles are produced in a relative Coulomb state at zero separation, and can therefore be approximated to come from a point-source [37]. The square of the Coulomb wave function then reduces to the Gamow factor,

$$|\psi_c(0)| \; = \; (\frac{2\pi\eta}{e^{2\pi\eta} - 1}) \tag{2.52}$$

η is the dimensionless Sommerfeld factor,

$$\eta \; = \; \frac{z^1 z^2 e^2}{v_{rel}} \tag{2.53}$$

Here, $z^1 e$ and $z^2 e$ are particle charges and v_{rel} is their relative velocity calculated as q/m_{red}.

The Coulomb corrected function is obtained from dividing the measured correlation function by the Gamow factor,

$$C_2(\overrightarrow{p}_1, \overrightarrow{p}_2) \; = \; C_2^{measured}(\overrightarrow{p}_1, \overrightarrow{p}_2) G^{-1}(\eta) \tag{2.54}$$

For same charge particles, the suppression effect of the Gamow factor tends to $2\pi\eta e^{-2\pi\eta}$ at small q ($q \rightarrow 0$).

While the point-source approximation is computationally desirable, it overestimates the Coulomb interactions in heavy-ion collions. For heavy-ion collisions, it is necessary to take the extended source approach where we integrate the Coulomb wave function iteratively, with initial estimates obtained by application of the Gamow factor.

3. The experiment

3.1. RHIC

The **R**elativistic **H**eavy-**I**on **C**ollider (RHIC) located on the Brookhaven National Laboratory campus is a Department of Energy run facility for studies in nuclear physics, and currently one of only two collider facilities doing research in heavy-ion collisions.

RHIC was commissioned in 2000 together with four detectors: BRAHMS, PHENIX, PHOBOS, and STAR. The BRAHMS and PHOBOS detectors have as of this date wound up operations [11, 34, 70].

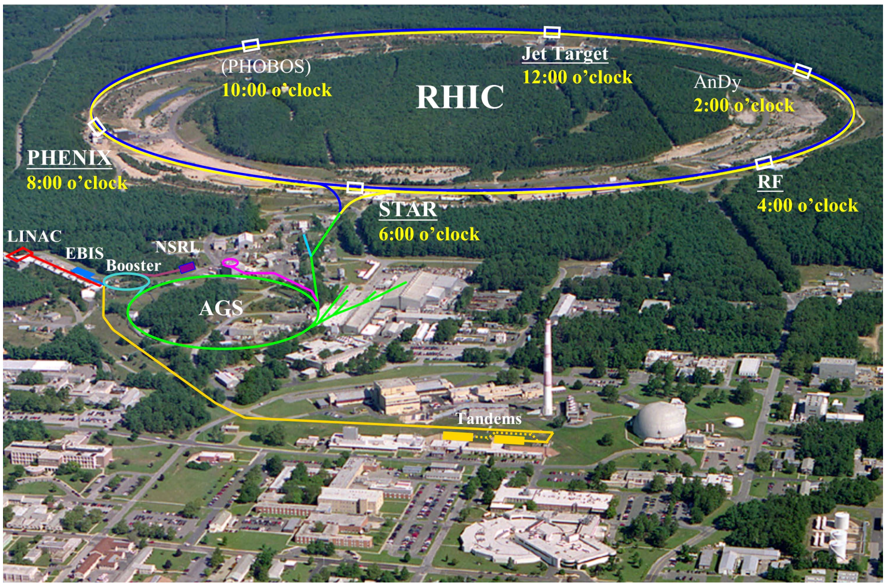

Figure 3.1.: Aerial view of the RHIC facility with overlays to show the positions of the four detectors and the auxiliary accelerator facilities.

With its commissioning, RHIC has two main physics objectives:

(1) Study the phase diagram and investigate the phase transitions of hadronic matter to QGP as well as identify and study the properties of QGP.

(2) As the only collider able to collide spin-polarized protons due to the addition of Siberian Snakes, investigate the proton spin structure over different beam energies.

The RHIC facility consists of the collider rings and its complimentary set of detectors, as well as the Alternating Gradient Synchotron, the Tandem Van de Graff, and the Booster which act as heavy-ion injectors. For proton-proton collisions, polarized protons are injected from the Proton Linac. With its design, RHIC is able to operate over a wide range of beam energies and particle species. Due to the two collider rings being completely autonomous and therefore able to run at different magnetic fields, the RHIC facility is also able to uniquely collide beams of unequal species, for example deuterium and gold, and therefore provides for an opportunity to study asymmetric systems [67].

3.1.1. Acceleration process for Au+Au collisions

- The Pulsed Spitter Ion Source at the Van de Graff provides beams of negatively charged gold ions.
- These ions are stripped off some of their electrons to give them a positive charge and an acceleration.
- The ions then enter the Booster Synchotron where they are stripped of more electrons and accelerated to give them a +32 charge and an energy of 95 MeV/u
- Before injection into the AGS, the ions are stripped off even more electrons, leaving them with a charge of +77. They then enter the AGS where they are accelerated to 10.8 GeV/u which is the RHIC rings injection energy.
- On exiting AGS, the ions are stripped off the remaining electrons giving them a charge of +79. Transfer to the RHIC rings is achieved through the AGS-to-RHIC Beam Transfer Line.
- At the collider, the ion beams are injected into either beam lines labeled “blue” or “yellow”. This is done through a switching magnet. Each ring carries 60 bunches with 1×10^9 ions/bunch and with 63.9 m spacing between bunches.
- Two Radio Frequency (RF) systems are used at RHIC:
    1. A 28 MHz RF system to get the bunches from AGS and accelerate them to full energy.
    2. A 197 MHz RF system for storage and collision

It takes about two minutes from injection to achieve top energy. After each injection cycle, each ring has about 6×10^{10} ions for gold (and about 6×10^{12} for protons and deuterons) .

3.1.2. STAR

The **S**olenoidal **T**racker **A**t **R**HIC (STAR), Figure 3.2, is one of two currently operational detectors at RHIC, designed to study and characterize the properties of QGP. It is a solenoidal detector of full azimuthal symmetry ($\Delta\phi = 2\pi$) and its large acceptance makes it well suited for performing measurements of hadron production at large solid angle, with the Time Projection Chamber (TPC) able to provide up to 4π solid angle tracking for charged hadrons.

While the TPC provides the primary 3-D tracking capability ($\Delta\phi = 2\pi$ azimuthal coverage; $|\eta| \leq 1.8$ in pseudorapidity), the Silicon Vertex Detector (SVT) is also used in the tracking of particles with short lifetimes and the Forward TPC (FTPC) allows for tracking of charged particles at forward rapidity ($2.5< |\eta| < 4$) [9].

3.1.3. PHENIX

The **P**ioneering **H**igh **E**nergy **N**uclear **I**nteraction e**X**periment (PHENIX) is one of the other major experiments at RHIC and the focus of this work. Complementary to the STAR detector with regard to its physics objectives, the PHENIX detector consists of three magnetic spectrometers for the measurement of direct probes of heavy-ion collisions. A more detailed discussion of the PHENIX detector is provided in section 3.2.

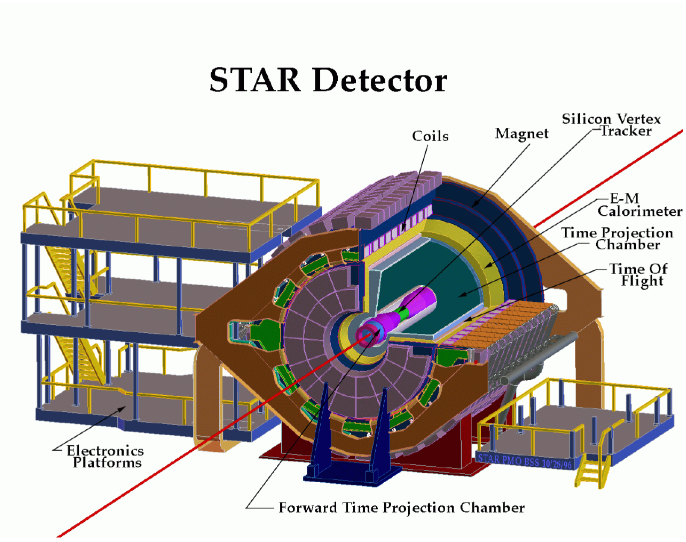

Figure 3.2.: The STAR detector at RHIC showing the main subsystems.

3.2. The PHENIX Experiment

The PHENIX experiment is a multinational collaboration comprising of more than 500 scientists and engineers from 56 institutions in 12 countries. Its primary physics objective is to identify and study the characteristics of QGP as well as the phase transitions leading to its formation. In addition, the PHENIX experiment aims to develop an understanding of the proton's spin.

To meet its physics objectives, the experiment utilizes the PHENIX detector–a highly sophisticated and versatile multisystem detector, with the ability to measure a wide range of particles at very good energy and momentum resolution. Figures 3.3a and 3.3b show the PHENIX detector configurations for RHIC Run-year 2007 and 2010 respectively whose results are covered in this work.

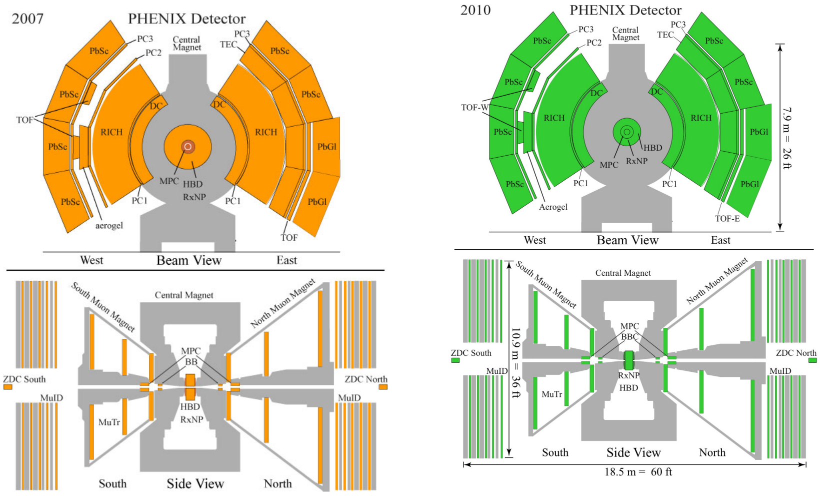

(a) PHENIX run-7 detector configuration

(b) PHENIX run-10 detector configuration

Figure 3.3.: PHENIX detector configurations for some of the analysis covered in this thesis.

The detector discussion is organized in the following manner: Section 3.2.1 dicusses the global (inner) detectors. These comprise of the Beam Beam Counter (BBC) and the Zero Degree Calorimeter (ZDC) which provide measurements for event characterization and are also an integral part of the PHENIX Level-1 trigger for data acquisition. Section 3.2.2 is a discussion of the magnet system, with particular emphasis on the Central Magnets which provide the field for the central arm spectrometers. Section 3.2.2 gives a detailed discussion of the subystems that constitute the central arm spectrometers. These subystems include the Drift Chamber and the Pad Chamber that provide tracking information, and the Electromagnetic Calorimeter, Time-of-Flight detector, and Ring Imaging Cherenkov detector used for particle identification. The muon spectrometers found at forward rapidity as well as other subsystems that make up the central arm spectrometer, but not utilized in this analysis, will not be discussed. Additional details on the PHENIX susbsystems can be found at [18]

3.2.1. Global subsystems

Beam Beam Counter (BBC)

The BBC, as shown in Figure 3.4, consists of two identical counters, one on the north side and the other on the south side around the beam pipe at the collision points. They cover $3.0 < |\eta < 3.9$ in pseudorapidity and $\Delta\phi = 2\pi$ in azimuthal, and are located about 1.44 m from the center of the interaction [27].

Figure 3.4.: The Beam Beam Counter.

The role of the BBC is to provide the start time for events in time-of-flight measurements. The precision of these measurements is especially important for obtaining a clean hadron PID and the BBC has very good timing resolution of 52 ± 4 ps. Figure 3.5 shows how T_0 and the Z-vertex are determined by taking into account the hit times recorded in BBC North and BBC South. The BBC is also used to provide measurements of the collision vertex point along the beam which then become the starting point for charged particle tracking. In addition, the detector is an important part of the Level-1 trigger used to select for events of interest before they are digitized.

$Z - Vertex\ = \frac{T_S - T_N}{2} \times c$; $T_0 = \frac{T_S + T_N - 2L/c}{2}$

where T_S and T_N are the arrival times at the south and north counters respectively. L is the separation distance from the interaction point (1.44 m) and c is the speed of light.

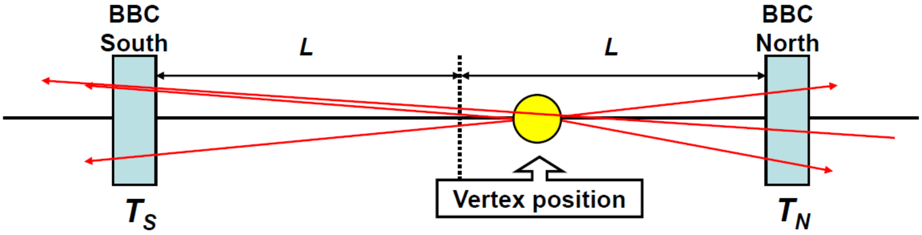

Figure 3.5.: Cartoon showing the determination of T_0 and $Z - vertex$ using the BBC.

Determination of centrality Using the charge sum measured in the BBC, we are able to determine the collision centrality and define the centrality classes as described in the analysis section.

Design Each of the counters is made up of 64 PhotoMultiplier Tubes (PMT). Each of these PMTs carries a 3 cm quartz on its head which acts as a Cherenkov radiator. Its total outer diameter is 30 cm and it has an inner diameter of 10 cm. For this dimensions, we are able to get 15 particles per BBC element for a $Au + Au$ collision at $\sqrt{s_{NN}} = 200$ GeV.

Zero Degree Calorimeter

Situated about 18 m from the interaction point, and with a horizontal acceptance of ±5 cm, the ZDC is a hadron calorimeter designed to measure neutron fragments of heavy-ion collisions within a $\theta \leq 2$ mrad cone of the beam in both directions (Figure 3.6) . In this so called zero degree region, the energy contribution from other particles is insignificant as compared to that from free “spectator” neutrons. The total energy measured is used in the determination of multiplicity. The ZDC’s sensitivity to fragmentation neutrons of collision therefore makes it useful as a minimum bias event trigger and for measurements of luminosity. The detector can also be used in centrality determination since there is a strong correlation between the neutron multiplicity and the collision geometry [20].

3.2.2. Magnet System

The PHENIX magnet system comprises of three sub-systems all with full azimuthal coverage ($\Delta\phi = 2\pi$). These are:

(1) Central Magnets providing a magnetic field at the interaction vertex.

(2) The north and (3) south Muon Magnets which provide a magnetic field for muon studies at forward rapidity [31].

Figure 3.7 is a schematic of the magnets while Figure 3.8 shows their fieldmap.

Central Magnet

This is an axial magnet sitting at $|\eta| < 0.35$ pseudorapidity and with a polar angle coverage of $70° < \theta < 110°$. Weighing more than 500 tons and rising to a height of 9 m, the central magnet consists of warm iron yokes and water-cooled copper coils wrapped around a cylindrical surface. It provides an integral field of ablut 0.8 Tesla-meter at 90°to the beam line.

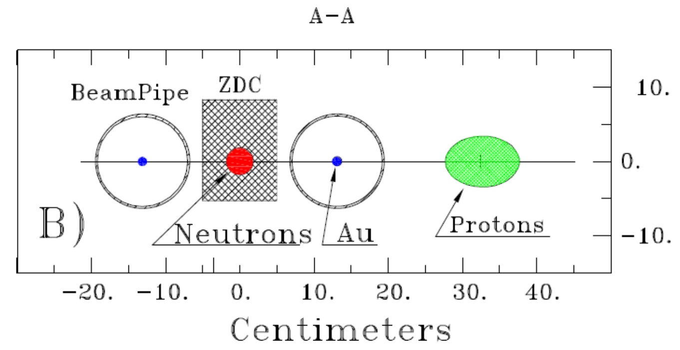

(a) Cross-section view of the ZDC along the beam.

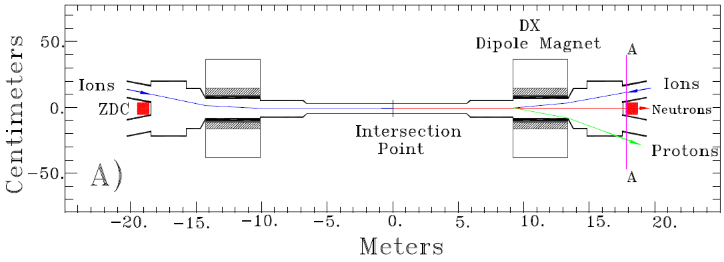

(b) Top view of the ZDC location with respect to the Dipole Magnets.

Figure 3.6.: Schematic diagrams of the Zero Degree Calorimeter.

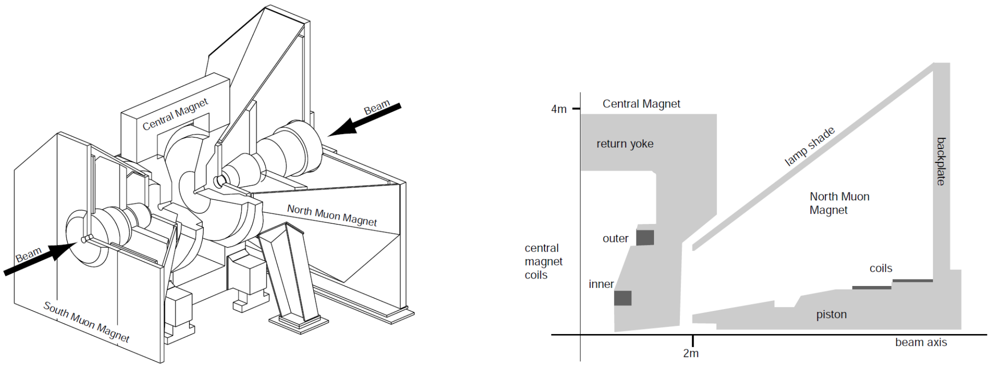

(a) Schematic diagram of the PHENIX magnets.

(b) A Vertical Slice view of the PHENIX magnets as seen along the beam axis.

Figure 3.7.: Central and Muon PHENIX magnets.

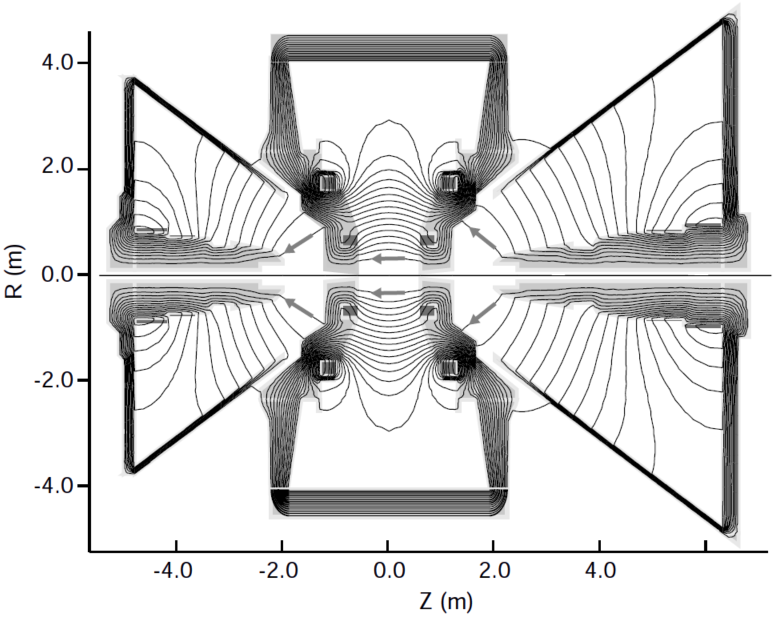

Figure 3.8.: Central and Muon magnets field map.

North and south Muon Magnets

The north and south Muon Magnets are 355 ton (248 ton for south) radial magnets consisting of solenoid coils wound around a tapered piston. With a height of 10 m, the north(south) magnet covers $1.1 < |\eta| < 2.4$ ($-2.2 < |\eta| < -1.1$) in pseudorapidity and $10° < |\theta| < 37°$ ($12° < |\theta| < 37°$) in polar angle. Each magnet provides a field integral of about 0.75 Tesla-meter at 15° to the beam line.

3.2.3. Central Arm Subsystems

The central spectrometer consists of subsystems used for charged particles tracking and identification of both hadrons and leptons. Covering $|\eta| = 3.5$ in pseudorapidity, the magnetic field of the central arm is provided by the central magnet discussed in section 3.2.2.

Tracking systems

In PHENIX, the tracking information is provided by two susbystems: The Drift Chamber (Figures 3.9, 3.10, and 3.11) and the Pad Chambers (Figures 3.12 and 3.13). These two subsystems allow for accurate momentum determination of charged particles as well as providing position information used in track reconstruction and in the PHENIX Level-2 trigger [19].

Drift Chamber (DC)

The DCs are cylindrically shaped multiwire detectors found on both east and west PHENIX central arms. They are found between 2.0 m and 2.46 m in radial distance from the interaction point, 1.8 m in the z direction, and with a combined $\Delta\phi = \pi$ in azimuthal coverage. The DCs determine the transverse momentum of charged particles by making accurate measurements of their trajectory in the $r - \phi$ plane. This information is then used to determine the invariant mass of particle pairs. In addition, the DCs also provide initial tracking position information used to reconstruct tracks through the various subsystems.

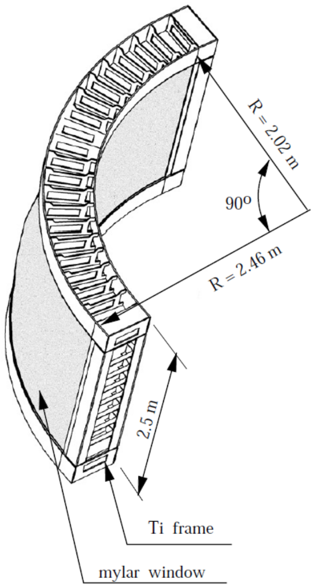

Figure 3.9.: Schematic diagram of the Drift Chamber.

Design and operation Each DC is made up of a titanium frame to which is attached a five-mil Al-mylar window, effectively defining a cylindrical gas volume as shown in Figure 3.9. Each gas volume consists of 20 equal-sized sectors of $\Delta\phi = 4.5°$ in azimuthal. In each sector are six types of radially aligned modules in the sequence X1, U1, V1, X2, U2, and V2. A single module carries four anode and four cathode wire nets. The X1 and X2 wire cells, each with 12 anode wires, make precise measurements in the $r - \phi$ direction and are therefore aligned parallel to the beam. To obtain z direction measurements, U1, V1, U2, and V2 wires with stereo angles of 6° with respect to the X wires are utilized. This stereo angle was selected to be comparable to the z resolution of the Pad Chambers for better tracking efficiency. The chambers are filled with a working gas mixture of 50% argon and 50% ethane, chosen due to its low diffusion coefficient, uniform drift velocity, and high gas gain.

The Drift Chambers tracks particles by measuring the drift time of electrons formed from gas ionization when a charged particle passes through it. The signal created is read out by electronic circuit cards located on each sector. Each sector carries 4 ASD/TMC cards. The ASD (Amplification, Shaping, and Discrimination) is the analog part of the card that receives the charge signal from the wires. The TMC (Time Memory Cell) is the digital part responsible for time digitization of the signal. The ASD/TMC cards are controlled by one Front End Module (FEM) card mounted on top of them.

Tracking $Au + Au$ collisions are high multiplicity events and the typical occupancy in each of the DCs is about 200 tracks. To effectively determine tracks from the numerous hits to the detector, PHENIX utilizes a tracking algorithm based on the Hough transform

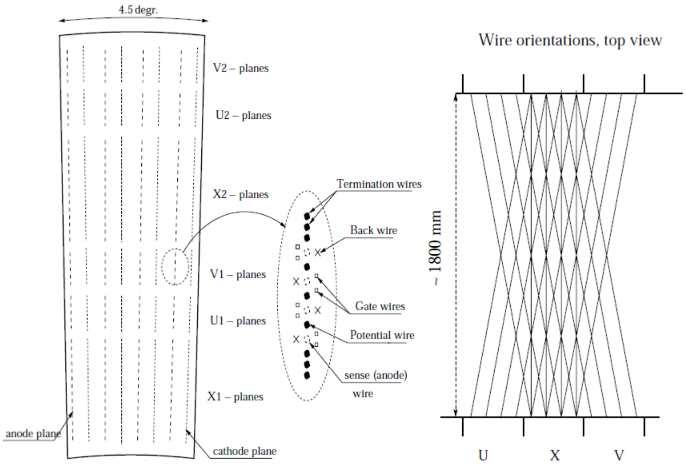

Figure 3.10.: DC wire configuration as shown for one sector and seen from the side (top) in the left (right) schematic diagrams.

of the ϕ and α for every single combination in hits. ϕ and α are as defined in Figure 3.11. These values are binned in a Hough array and a 2-D histogram generated. Each of these binned combinations is a viable track candidate. A true track is expected to have many hits in the detector, therefore tracks are selected from the 2-D histogram by looking for a local maxima that meets the requirements of a set threshold value.

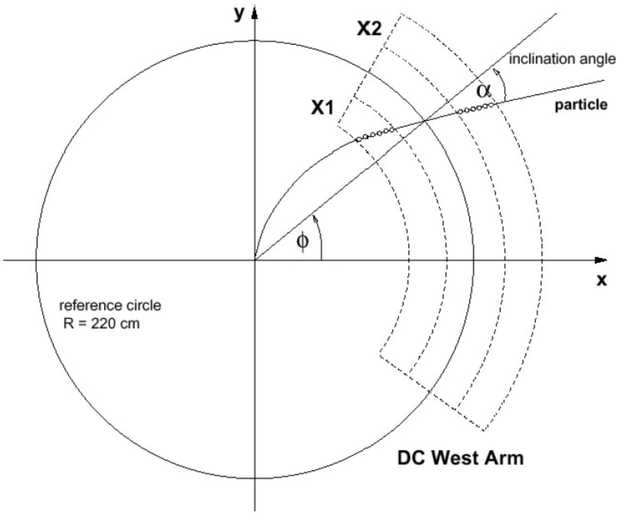

Figure 3.11.: A schematic diagram of the DC in the $r-\phi$ plane, describing the α and ϕ space variables used in the Hough transform. Hits in the DC are shown as small open circles.

Pad Chambers (PC)

The PCs consist of three layers of pixel detectors – PC1, PC2, and PC3 – on both central arms east and west. PC1 is found right behind the DC and in front of the Ring-Imaging Cherenkov detector (RICH), PC2 is located immediately behind RICH, but only on the west arm, and PC3 is found in front of the Electromagnetic Calorimeter (EMCal) in both east and west arms (see Figures 3.3a and 3.3b).

Each of the PC layers is made up of a gas volume containing a mixture of argon and ethane in which is suspended a single plane of anode bound by two cathode planes.

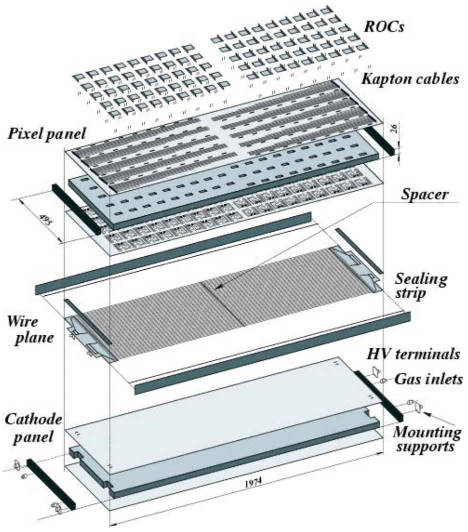

Figure 3.12.: Expanded schematic of PC1 showing the various components.

One of the cathodes is a solid block of copper while the other consists of an array of pixels. Each single pixel is connected to eight others making a pad with the signal from each pad read out by a single discriminant. A hit on the detector creates an avalanche in the anode and the resulting current is read out by the Readout Cards (ROCs). The ROCs are controlled by FEMs found at the edge of the detector. Each hit triggers a response in three neighboring pads. The track can then be uniquely identified by tracking it to three neighboring pixels in what is known as a cell. A track is only accepted if an avalanche is detected in all three pixels of the cell. The PCs architecture is described in Figure 3.12 while Figure 3.13 shows the layout of the pad and cell.

Within the PHENIX experiment, the PCs play several crucial roles. PC1 provides the z coordinate needed in measurements of the 3-D momentum vector for tracks as well as tracking of charged particles to RICH and the EMCal in e^+ and e^- PID. PC2 and PC3 provide for track matching necessary in suppressing products of particle decay and secondary interactions [89].

Particle Identification (PID)

The Time-of-Flight detectors (TOF) at PHENIX are composed of two separate systems. The TOF in the central east arm and the TOF-West in the central west arm. They both provide for a charged hadron PID over a wide p_T range, and with very good timing resolution.

TOF

Located 5.1 m from the collision vertex, the TOF detector is based on scintillator technology. It covers $\pi/4$ in azimuthal and $70° \leq \theta \leq 110°$ in pseudorapidity, and has a

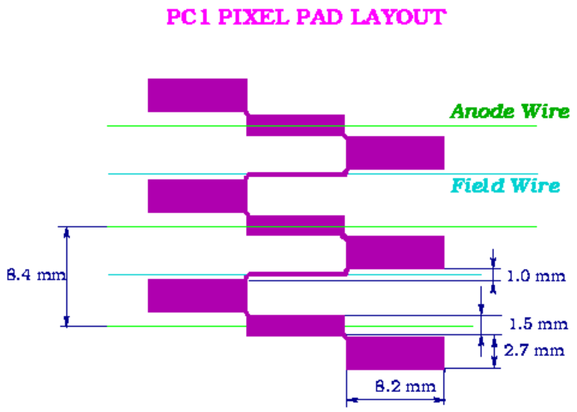

(a) A pad consists of nine interconnected pixels.

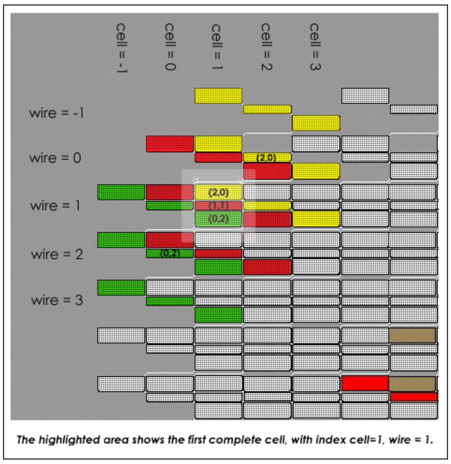

(b) Three pixels constitute a cell where each pixel in a cell is connected to a different but adjoining channel.

Figure 3.13.: Pad and pixel geometry of the Pad Chamber.

timing resolution of 100 ps. This very good timing resolution allows for a clean π/K PID up to 2.4 GeV/c and $K/proton$ PID up to 4.0 GeV/c at 4 σ.

The detector is composed of 10 panels oriented in the $r - \varphi$ direction with each panel carrying 96 slats which are the functional units of the system. Each slat, shown in Figure 3.14, consists of a plastic scintillator with read out PMTs on each end. The slats are glued to a honeycomb scafford made of carbon fiber to provide the necessary support [26].

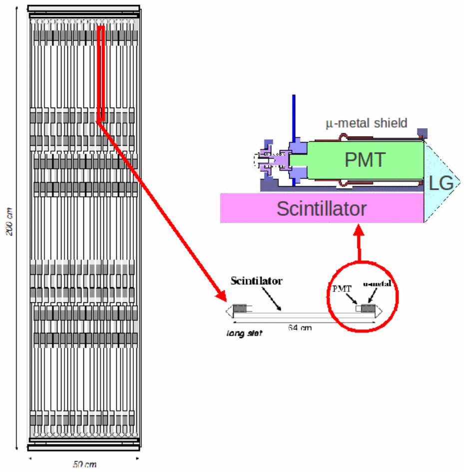

Figure 3.14.: Schematic drawing of a slat for the TOF detector.

Timing Mechanism The time-of-flight is obtained from precise measurements of start/stop time. The start time, T_0, is provided by the BBC. Figure 3.15 shows how the time-of-flight is measured using the TOF detector.

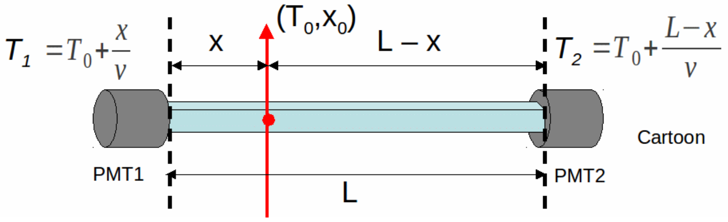

Figure 3.15.: Details of the timing mechanism in the TOF detector.

$$TOF = \frac{((T_1 + T_2) - L/v)}{2}$$

$$Y_{position} = \frac{T_1 - T_2}{2} v$$

T_1 and T_2 are obtained from PMT1 and PMT2 respectively. L is the slat length and v is the speed of light in the scintillator. T_0 is the start time obtained from the BBC.

TOF-West

The TOF-West detector installed for RHIC Run-2006 is a Multi-Gap Resistive Plate Chamber (MRPC) located on the west central arm of the PHENIX detector, about

4.8 m from the collision vertex. It consists of two subsectors: The first subsector at $-6.3° < \phi < 3.5°$ in azimuthal coverage is located behind the Aerogel detector. The position of this subsector allows for efficient PID coordination with the Aerogel. The second subsector is located at $11.5 < \phi < 26$ in azimuthal, a position that is especially important for jet correlation studies since it allows for measurements of back-to-back jet particles at high p_T. TOF-West provides for an intrinsic timing resolution of 69 ps (acounting for $\sigma = 40$ ps timing resolution of the BBC, which provides the start time). With this excellent timing resolution π/K separation to 3 GeV/c and K/p separation to 5 GeV/c can be obtained.

Structure and Operation The TOF-West detector is made up of 128 MRPC chambers with four strips per chamber. Each gaseous ion chamber is partitioned into six parallel gaps by five glass plates. A schematic diagram of an MRPC is shown in Figure 3.16.

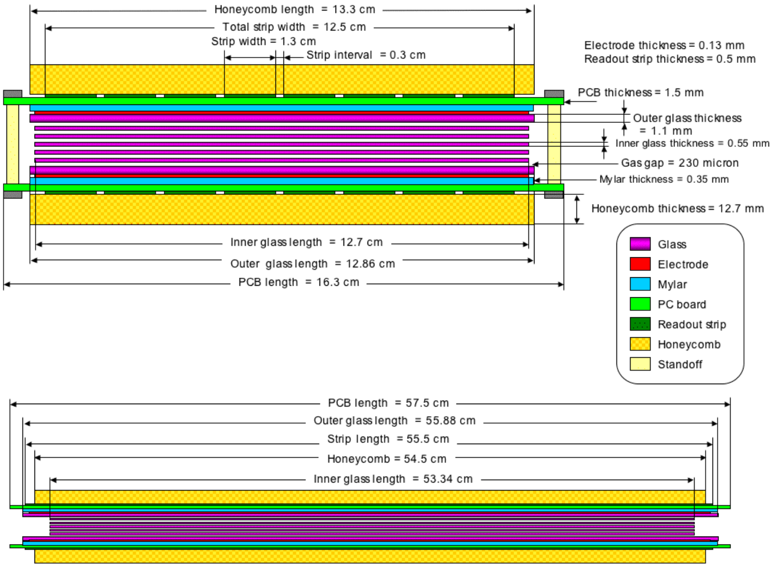

Figure 3.16.: A cross-sectional view of the TOF-West MRPC.

A working gas mixture of R-134a (Freon) at 90% volume, iosbutane (5% by volume), and sulfur hexafluoride (5% by volume) occupies the chamber.

When a particle hits the detector, it induces an avalanche of charge separation and a current is transmitted between the pad anode and cathode. The raw signal generated is carried, through a six-inch twisted pair cable, to the Front End Electronics (FEE) attached to the outside of the gas volume. One FEE board provides low-level signal processing for all eight channels of one MRPC chamber. The primary role of the FEEs is to amplify the signal before it is transmitted to the FEM. The TOF-West FEMs are similar to those in the TOF detector and they provide signal discrmination and digitization before the signal is passed on to PHENIX data acquisition [86].

Electromagnetic Calorimeter (EMCal)

The Electromagnetic Calorimeter or EMCal is located 5.1 m from the collision vertex. Consisting of a total of six sectors, the EMCal primary role is to measure the spatial position of photons and electrons. It is also used in measuring the hadronic energy at mid-rapidity and is an integral part of the PHENIX Level-1 trigger due to its ability to trigger at high p_T for photons and electrons.

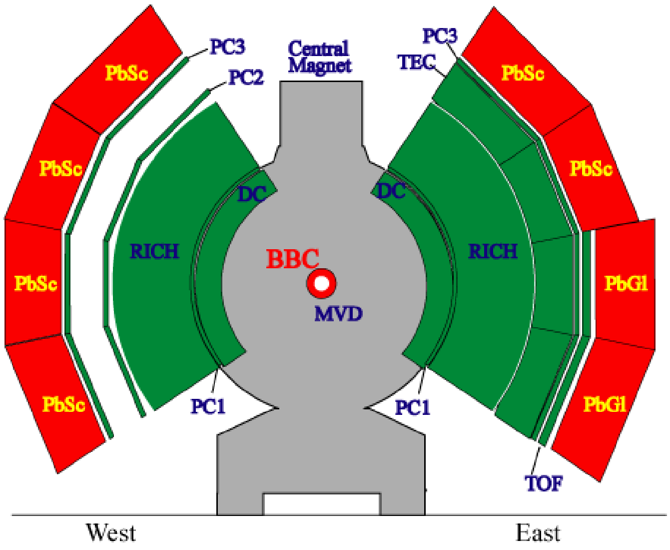

Figure 3.17.: The PHENIX detector with the PbSc and PbGl sectors highlighted in red.

The EMCal sits at $|\eta| = 0.375$ pseudorapidity and covers $\Delta\phi = 90° \times 2$ in azimuthal. The west arm ($\Delta\phi = 90°$) consists of four sectors of the Lead Scintillator (PbSc) sampling calorimeter. The east arm is made up of two PbSc sectors ($\Delta\phi = 45°$) and two Lead-Glass (PbGl) calorimeter sectors. This combination of two complimentary technologies with significantly varying properties provides for different systematics and therefore a necessary cross-check for physics results [30]. Figure 3.17 shows the location of the EMCal relative to the other subsystems in the PHENIX detector.

Lead-Scintillator (PbSc) PbSc is a sampling calorimeter consisting of alternating slabs of 1.5 mm lead absorber and 4.0 mm scintillator forming one sampling cell. The scintillator is made through injection molding from a mixture of polystyrene, 1.5 % p-terphenyl which is a fluorescent additive, and the organic scintillator p-bis[2-(5-phenyloxazollyl)]-benzene or POPOP at 0.01%. A single PbSc tower contains 66 layers of these cells with a wavelength-shifting, fibre-optic cable running through them and connected to PMT tubes at the end of the tower, as shown in Figure 3.18.

Four towers are grouped together to form a module, and 36 of these modules are then attached to a support scaffold forming a supermodule which is readout by one FEM. One sector comprises of 18 supermodules. The PbSc has an intrinsic timing resolution of $\sigma = 100$ ps for electromagnetic showers and $\sigma = 270$ ps for hadronic showers. It has energy resolution capabilities of 8% at 1 GeV. In general, the PbSc provides better timing capabilities and better linearity in response as compared to the PbGl.

Lead-Glass (PbGl) The PbGl is a homogeneous lead-glass Cherenkov radiation detector. There are two PbGl sectors located in the east central arm behind TOF and covering

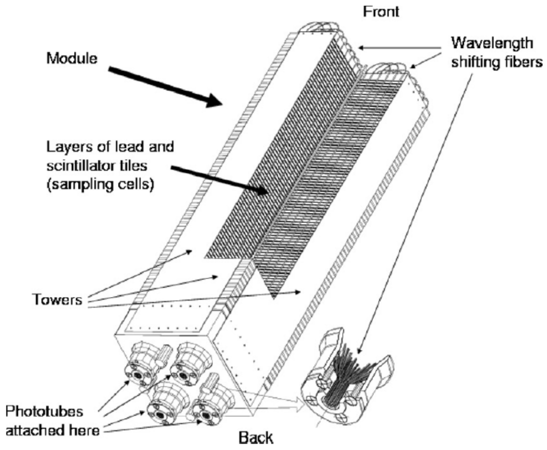

Figure 3.18.: Diagram of the parts of a PbSc tower, including the sampling cells and the PMTs attached to its end.

a total of $\Delta\phi = 45°$ in azimuthal. The functional unit of the PbGl detector is a 40 mm × 40 mm × 400 mm Pb-Glass tower wrapped in alumnized mylar foil, and then encased in a shrink tube. A single PMT is attached at the end of the tower. Twenty-four towers are glued together to form a supermodule, and 192 supermodules form one sector of the PbGl. Figure 3.19 shows the parts of a PbGl tower while Figure 3.20 shows how the towers are put together to form a supermodule.

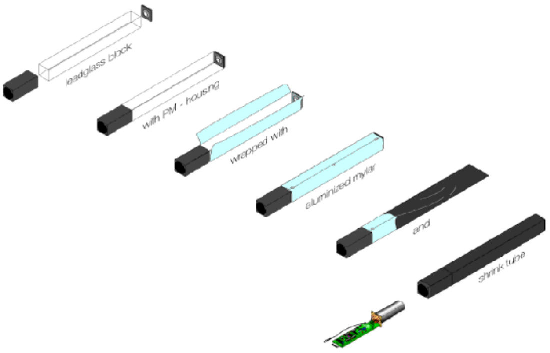

Figure 3.19.: A schematic diagram of a PbGl tower and its parts.

Like the PbSc, the PbGl sectors of the EMCal are designed for the identification of electrons and protons. Charged particles incident on the detector generate Cherenkov radiation which is then collected by the PMTs. Distinguishing hadrons from electrons and protons is facilitated by the fact that the detector only collects Cherenkov light and hadrons have a Cherenkov threshold momenta (27, 36, and 241 MeV for muons, pions, and protons respectively) and will therefore cease to produce any Cherenkov radiation when their momenta falls under those thresholds. The PbGl provides for an energy resolution of 5.95% $\sqrt{E}$ (GeV) and an intrinsic timing resolution of $\sigma = 100$ ps for both electromagnetic showers and hadronic showers . While the PbSc sectors excel in timing measurements, the PbGl sectors provide for better energy measurements.

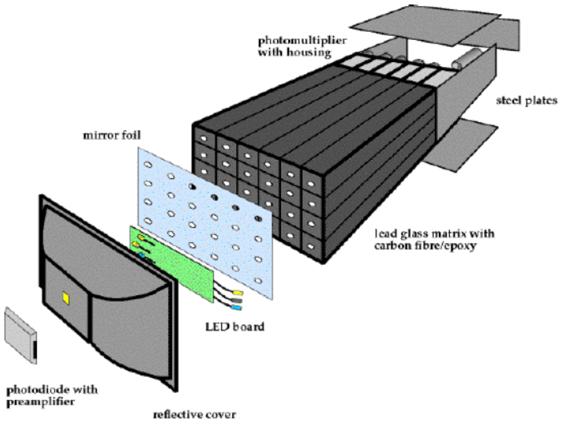

Figure 3.20.: A PbGl supermodule showing the arrangement of towers and PMTs.

The Ring-Imaging Cherenkov Detector (RICH)

The RICH detector is the primary electron PID detector at PHENIX. It consists of two identical detectors in the west and east arms, sitting right behind PC1 at a radial region $2.575 < r < 4.1$ m. As a threshold gas Cherenkov detector, RICH is designed to allow for e/π separation below the working gas Cherenkov threshold. This threshold is 4.9 GeV/c for a CO_2 radiator and 3.5 GeV/c for ethane. It can identify electrons from 0.02–4.9 GeV/c in momentum and it aims to keep the misidentification of hadrons as e^+ and e^- to less than 1 per 10^4. The detector consists of a 40 m^3 gas vessel filled with either CO^2 or ethane at 1 atm. The gas volume has entrance and exit windows of 8.9 m^2 and 21.6 m^2 respectively made of 125 μm alumnized kapton and covered in absorber sheet. Each of the gas volumes has two arrays of spherical mirrors for a total of 48 panels and a total reflective surface in each detector of 20 m^2. The array of mirrors focus the generated Cherenkov radiation on to two arrays of PMTs. The cutaway diagram in Figure 3.21 shows the various parts of the RICH detector.

When e^+ and e^- enter the gas volume, they induce the creation of Cherenkov radiation. This radiation is reflected by the mirrors and focused on to the PMTs in a ring-like fashion. In conjunction with the PHENIX tracking system, an electron is identified from a match in its direction in the tracking system and that in the ring, as determined from the ring position. In this study, the RICH detector was used to suppress the misidentified electrons by applying a RICH based e^+/e^- veto cut [26].

3.2.4. The PHENIX Data Acquisition (DAQ) and Online System

The PHENIX DAQ and online system, outlined in Figure 3.22, is responsible for taking the digitized signals from the Front End Modules associated with the different subsystems and processing them to wholesome events available for physics analysis. It is a fully pipelined system designed to digitize, transfer, and record event signals continously. This makes it a highly versatile system able to accomodate detector upgrades in luminosity [95].

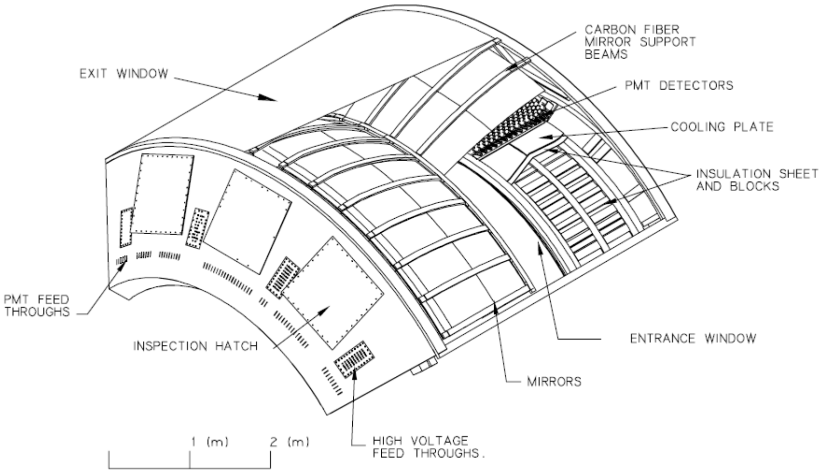

Figure 3.21.: RICH detector cutaway diagram showing its various components.

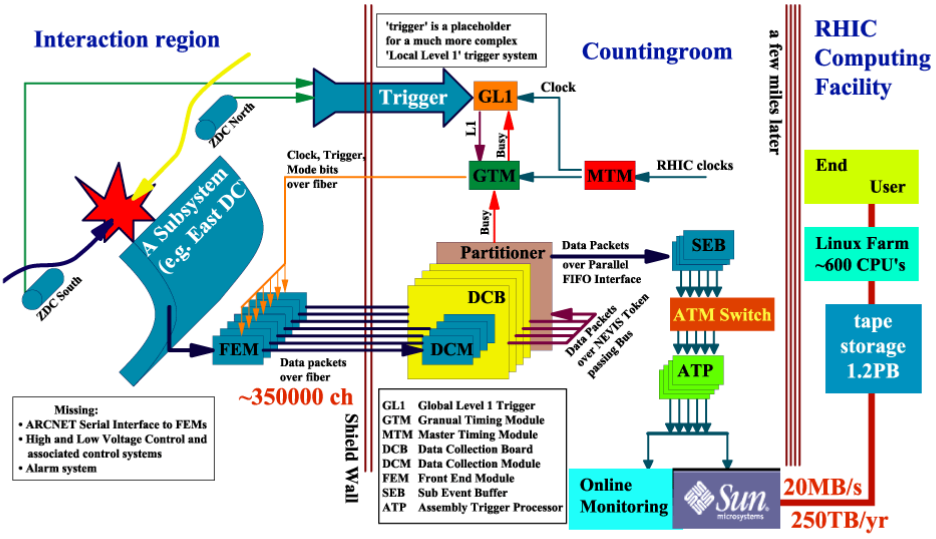

Figure 3.22.: The PHENIX on-line system.

Data Flow

Figure 3.23 is a block diagram of the data flow in PHENIX. In synchrony with the RHIC beam clock, the Front End Electronics (FEE) accept raw analog signals from their respective subsystems and convert them into digital event fragments at all beam crossings. The data is buffered long enough for the Level-1 trigger (LVL1) to accept or reject a signal. The accepted data fragments are then transferred to the Front End Modules (FEM). The primary role of the FEMs is to collect the digitized data after the LVL1 trigger and format it in preparation for transfer to the Data Collection Module (DCM). Four FEMs are connected to one DCM. Transfer of the data from the FEMs to the DCMs located in the Counting House is achieved by fibre optic cable.

Once the uncompressed event fragments are received by the DCMs, they are reformatted and checked for errors. The DCMs are also responsible for performing zero suppression on the data. From the DCMs, the data fragments are sent to the Event Builder (EvB) where they are assembled to complete events. During this prcoess, the Level-2 trigger (LVL2) selects for desired events, consequently reducing the total number of accepted events by a factor of six. The final accepted full events are logged and monitored by the PHENIX On-Line Control Monitoring (ONCS).

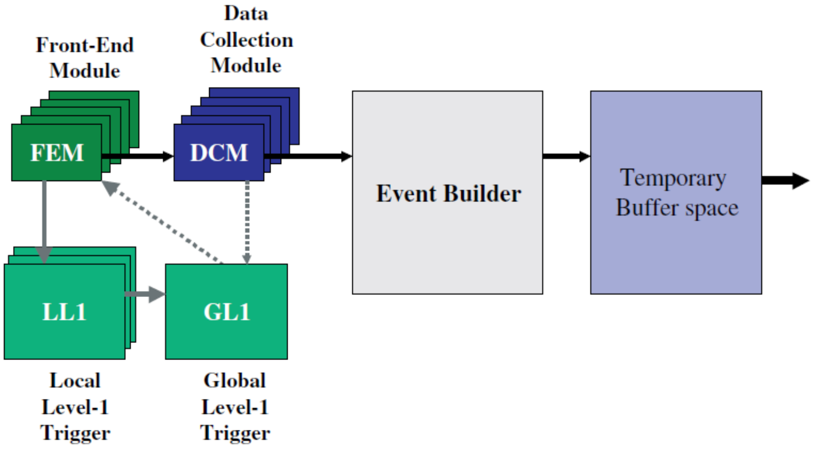

Figure 3.23.: Block diagram showing data flow in PHENIX.

Event Builder (EvB)

The final task of putting together the event data fragments to full events is done by the PHENIX Event Builder. The Level-2 trigger, which is tasked with reducing the data rate to one that is disk-archivable, also operates under the EvB. The EvB can handle data input at a rate of 12.5 kHz and perform event aggregation at a rate of 500 Mbyte/s.

The PHENIX trigger system

The PHENIX Level-1 and Level-2 triggering systems evolved from the need to maintain the high interaction rate at the PHENIX detector while still been able to make measurements, especially in the low p_T region that is characterized by huge backgrounds.

LVL1 Trigger

The LVL1 trigger is a fully pipelined triggering system with the primary role of reducing the number of events passed on to DAQ to a manageable data rate. This is accomplished by only selecting events that are of interest and also by excluding empty beam crossings. It consists of two different systems: The Local Level 1 (LL1) interacts directly with the BCC, ZDC, EMCal, MUID, and RICH subsystems. Input data from these detectors is bit-reduced and transferred to the second system, the Global Level 1 (GL1), which puts together the data so as to arrive at a trigger decision. LV1 trigger decisions are generated every 106 ns with an adjustable latency of 40 beam crossings.

LVL2 Trigger

The LVL2 trigger runs as part of the EvB. It is designed to reduce the data rate to that which can be written to disk. This is about 35 Mbyte/s for archiving, down from about 224 Mbyte/s . The LVL2 trigger does this by only accepting events that are deemed to be of physics importance. The selected events, as well as a sample of the minimum bias events, are then written to disk, together with the trigger decisions.

4. Analysis

4.1. Run summary

Run	Run year	Species	$\sqrt{s}$ GeV	No. of events	Trigger efficiency (%)
Run-5	2005	$Cu + Cu$	200	800 M	92
Run-7	2007	$Au + Au$	200	4.0 B	92
Run-8	2008	$d + Au$	200	1.85 B	88
Run-10	2010	$Au + Au$	39	200 M	86
Run-10	2010	$Au + Au$	62	550 M	86

Table 4.1.: Data summary for the datasets used in this analysis.

Table 4.1 is a summary of the datasets used in this study from RHIC Run-year 2005, 2007, 2008, and 2010 [57, 91, 92, 61].

4.2. Centrality Calibration

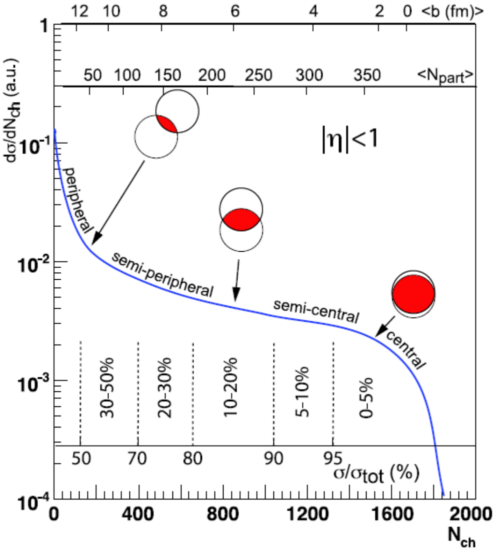

Figure 4.1.: Cartoon depiction of how the experimental observable sum of charges (N_{ch}) is related to the MC Glauber obtained variables of N_{part} and b after defining the centrality classes.

In heavy-ion collision studies, results are regularly expressed as a function of the collision geometry of the two nuclei. Unfortunately, none of the parameters used to characterize the collision geometry can be measured directly. Centrality definition is the process by which we connect the experimental observables sensitive to the impact parameter to the desired collision geometry parameters obtained by modeling so as to get a measure of the centrality of a collision. The experimental observable in this case is the number of charged particles as measured from the charge sum in the BBC. The parameters obtained from theoretical models are the number of participants (N_{part}) and the number of binary collisions (N_{coll}). The determination of centrality, and the relationship between the experimental measurables and the model derived parameters is shown in Figure 4.1.

Several different methods have been used in PHENIX for centrality determination :

- Applying perpendicular cuts to the BBC charge sum vs ZDC energy sum plot also known as the perp method.
- Until Run-5, the clock method was used extensively in PHENIX. For this method, we define a fixed origin, usually defined as (BBC, ZDC) = (0.2, 0) and calculate the angle ϕ relative to this point for a given value of ZDC, BBC. Centrality classes are determined by dividing the full ϕ range into equal count bins with the upper limit as the minimum bias trigger .
- Since Run-7, the BBC percentile method has been the preferred method of centrality definition in PHENIX, and the method used for the results presented here. With the BBC percentile method, centrality is defined by only cutting in the BBC charge sum to give bins with the same number of events. The application of the method for centrality definition is discussed in more detail in section 4.2.2.

The BBC percentile method uses the Negative Binomial Distribution (NBD) to relate the Glauber model derived parameters to the hits recorded in the BBC.

There are several steps involved in the determination of centrality. In brief, these are:

1. Run a Monte Carlo (MC) Glauber model for minimum bias events to calculate N_{part} and N_{coll}.
2. Obtain the integrated BBC total charge distribution for minimum bias events for the entire run.
3. Estimate the trigger efficiency by fitting the total multiplicity from contributions from each N_{part}, both in the data and the model, with a Negative Binomial Distribution (NBD).
4. Use the trigger efficiency value to set the upper limit of the centrality range, and define the centrality classes by dividing the BBC total charge distribution into equal-sized bins.
5. Use the defined centrality to estimate Glauber model parameters for each centrality bin.

These steps are covered in more detail in the following sections.

4.2.1. Monte Carlo Glauber Simulation

The MC Glauber simulation is built on a couple of assumptions. One assumption is that the total geometric cross-section is a good approximation of the total inelastic cross-section. Another assumption is that the colliding nuclei travel in straight line trajectories, and that the inelastic nucleon-nucleon collisions are independent of the nucleon's collision history. These assumptions are not intended to provide a complete picture of the dynamics of heavy-ion collisions, but rather a scaffold for the study of the collision geometry, without introducing medium effects.

For this analysis, MC Glauber simulation was used in two instances. First, MC Glauber simulation was used to generate the N_{part} distribution used to extract the trigger efficiency. Once the centrality classes had been defined, MC Glauber simulation was applied again to determine the geometric quantities N_{part}, N_{coll}, and $\overline{R}$ for each centrality class. $\overline{R}$ is the initial transverse size of the system, defined as:

$$\frac{1}{\overline{R}} = \sqrt{\frac{1}{\sigma_x^2} + \frac{1}{\sigma_y^2}} \tag{4.1}$$

with σ_x and σ_y as the rms widths of the distribution [41].

How it works Nuclei are assigned a random impact parameter based on the distribution

$$\frac{dN}{db} = 2\pi b \tag{4.2}$$

where N is the number of events and b is the impact parameter

Once the impact parameter is determined, each nucleon is assigned a position vector based on the nuclear density distribution as described by the Woods-Saxon function:

$$\rho(r) = \frac{\rho_0}{1 + e^{\frac{r-R}{a}}} \tag{4.3}$$

Where r is the distance to the center of gravity of the nucleus, a is the diffusion parameter, and ρ_0 is some normalization.

Two nucleons are allowed to collide if the distance of separation between them, d, is such that:

$$d \leq \sqrt{\sigma_{inel}^{NN}}/\pi \tag{4.4}$$

σ_{inel}^{NN} is the total inelastic nucleon-nucleon cross section.

A nucleon is considered a participant if it undergoes at least one inelastic nucleon-nucleon collision. One thing to note too is that the model as was applied in the determination of N_{part} in this analysis allows for overlap between the nucleons in the colliding nucleus. The case without any nucleon overlap was used in the estimation of the systematc errors.

4.2.2. Trigger Efficiency

$Au + Au$ collisions at PHENIX are very high multiplicity events. Nevertheless, the lower multitplicity at peripheral collisions means that there will be cases where no hits are registered in the trigger detectors which in turn leads to dropped events. The trigger efficiency will therefore decline in the more peripheral events. Calculation of the trigger efficiency is a necessary and crucial step in centrality determination. The trigger efficiency value is consequently used as the upper limit of centrality for inclusive minimum bias events.

For all the runs, the Negative Binomial Distribution (NBD) was used to make an estimate of the trigger efficiency. The method was employed based on the following assumptions:

- Each participant nucleon creates particles independently. One can therefore treat the multiplicity for each event as a linear summation from the contribution of each nucleon.
- It is assumed that the distribution is independent of the pseudorapidity and therefore the only dependence is that on centrality.
- The slope of the the N_{part} distribution from real data is similar to that obtained from the MC Glauber model.
- Hits contribution from each nucleon obey NBD statistics.

Minimum bias events were used to determine the trigger efficiency under the following trigger conditions:

- Two or more hits in both BBC north and BBC south
- Two or more hits in both ZDC north and ZDC south
- A ZDC vertex cut of $|z| < 30$ cm

Summary of the steps in trigger efficiency calculation

To determine the trigger efficiency, the N_{part} distribution for each beam energy is obtained using Monte Carlo Glauber as detailed in section 4.2.1. Using this N_{part} distribution, the number of hits associated with each participant are generated by applying the NBD. The total number of hits in the detector is simply a summation of the hits contribution from all the participants, i.e.,

$$N_{hits} = \sum_{i=1}^{N_{part}} n_i \tag{4.5}$$

where n_i is the number of hits contribution from the i^{th} participant.

The simulated distribution for a particular detector is compared to the measured distribution and the trigger efficiency is expressed as:

$$\epsilon = \frac{\text{total } N_{hits} \text{ from data}}{\text{total } N_{hits} \text{ from simulation}} \tag{4.6}$$

Run-5 This was the first application of the BBC method for centrality determination as opposed to the previously used CLOCK method. The trigger efficiency was determined from the distribution of the number of hits in both BBC North and BBC South and found to be 92% ± 0.65. Figure 4.2 shows the BBC distribution and the calculated trigger efficiency.

Run-7 The trigger efficiency in Run-7 was calculated from the hits distribution in BBC North and BBC South and found to be 92% ± 0.4 (stat) ± 1.6 (sys). The BBC distributions can be seen in Figure 4.3.

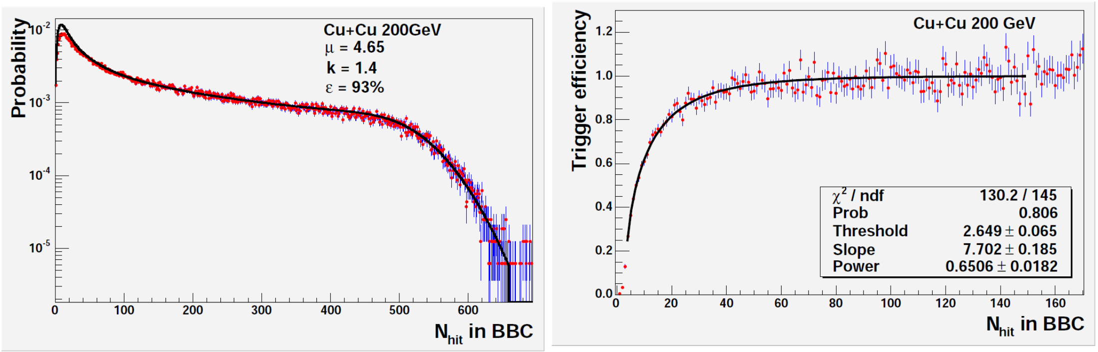

Figure 4.2.: (Left panel) Distribution of the total number of hits in the BBC detector, with the NBD fit shown in red. (Right panel) the trigger efficiency calculated from the total number of hits in the BBC for Run-5 $Cu + Cu$ $\sqrt{s_{NN}} = 200$ GeV.

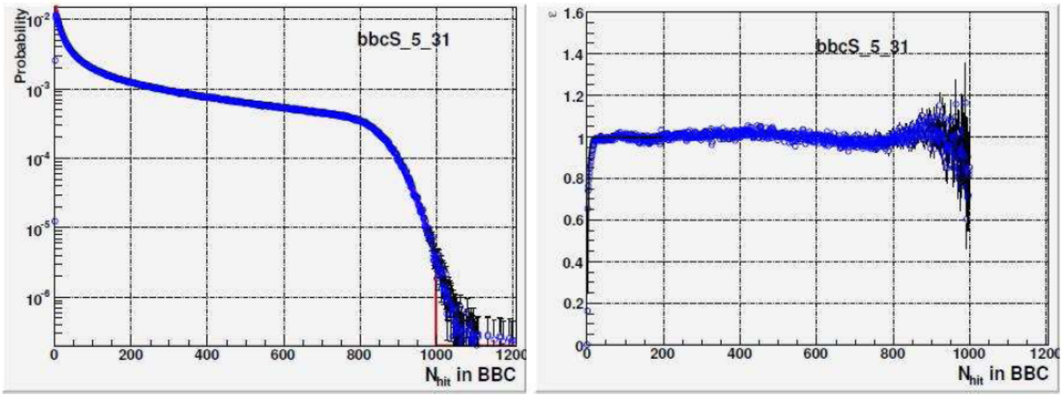

Figure 4.3.: (Left panel) A comparison of the simulated hits distribution to the real data for the BBC in $Au + Au$ $\sqrt{s_{NN}} = 200$ GeV. (Right panel) trigger efficiency from taking the rations of the real data to the simulated data. The dip at small N_{hit} is due to a drop in efficiency in the real data.

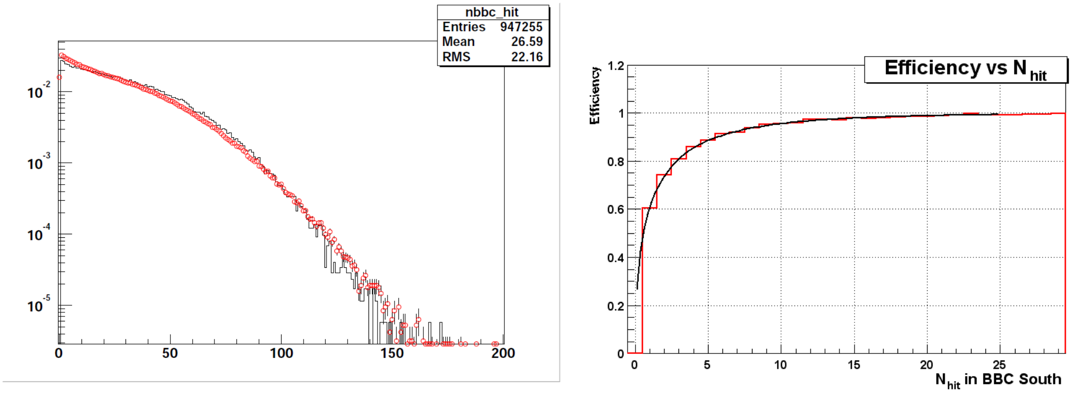

Figure 4.4.: (Left panel) BBC distribution of the total number of hits. (Right panel) The trigger efficiency as obtained using BBC South in Run-8 $d + Au$ $\sqrt{s} = 200$ GeV.

Run-8 For Run-8, the trigger efficiency was determined using only BBC South and found to be 88% ± 2.0. This determination is shown in Figure 4.4

Run-10 For Run-10, the trigger efficiency was found by averaging the response from PC1, PC3, Reaction Plane in (RXNin), and Reaction Plane out (RXNout). As mentioned previously, one of the assumptions made in the NBD method is that there is no pseudorapidity dependence on the hits distribution for real events. From studies done, it was found that the low energy runs BBC hits distributions shows a pseudorapidity dependence. For this reason, the BBC was excluded from studies of the trigger efficiency for $\sqrt{s_{NN}}$ = 39 GeV and 62 GeV. Tables 4.2 and 4.3 provides a summary of the trigger efficiency values, and their averages for $\sqrt{s_{NN}}$ = 39 GeV and 62 GeV respectively while Figures 4.5 and 4.6 show a comparison of the simulated hits distribution to the real data in PC1.

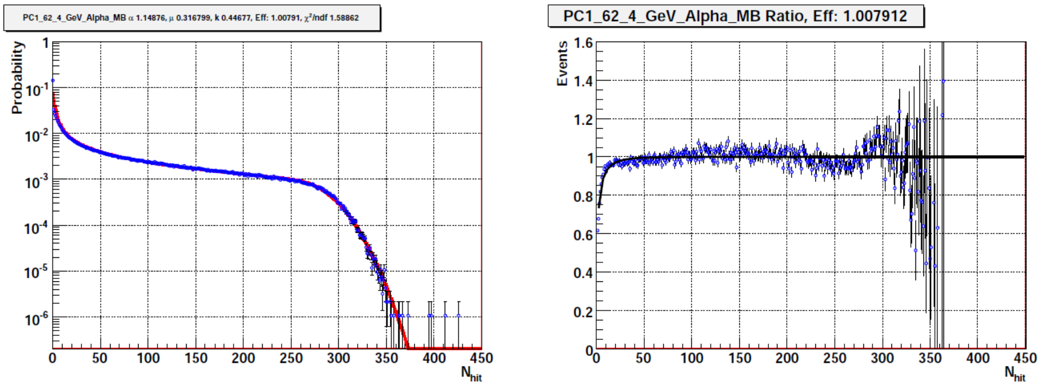

Figure 4.5.: (Left panel) A comparison of the simulated hits distribution to the real data for PC1 in $Au + Au$ $\sqrt{s_{NN}}$ = 62 GeV. (Right panel) trigger efficiency from taking the ratio of the real data to the simulated data. The trigger efficiency was determined from the avergage efficiency values of PC1, PC3, and Reaction Plane in and out.

Detector	χ^2/ndf	$Trigger\ Efficiency$
$PC1$	1.53	85.84± 0.23
$PC3$	1.73	84.72± 0.84
RXN_{In}	1.35	86.03± 0.14
RXN_{Out}	1.35	86.09± 0.20
$Mean$		85.67± 0.56

Table 4.2.: Trigger efficiency values calculated for $\sqrt{s_{NN}}$ = 62 GeV using the NBD method.

Centrality classes determination

To determine the centrality classes, the trigger efficiency is rounded off to the nearest integer and used as the upper limit for the total number of bins. The BBC charge distribution, taken as a sum of the north and south arms minimum bias events, is divided

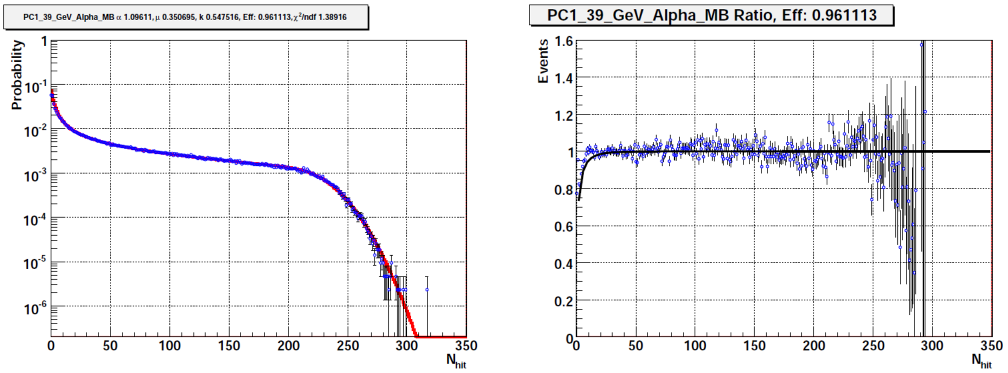

Figure 4.6.: (Left panel) A comparison of the simulated hits distribution to the real data for PC1 in $Au + Au$ $\sqrt{s_{NN}} = 39$ GeV. (Right panel) trigger efficiency from taking the ratio of the real data to the simulated data. The trigger efficiency was determined from the avergage efficiency values of PC1, PC3, and Reaction Plane in and out.

Detector	χ^2/ndf	$Trigger\ Efficiency$
$PC1$	1.40	85.16± 0.31
$PC3$	1.18	85.56± 0.36
RXN_{In}	1.06	85.59± 0.26
RXN_{Out}	2.54	87.41± 0.25
$Mean$		85.90± 0.86

Table 4.3.: Trigger efficiency values calculated for $\sqrt{s_{NN}} = 39$ GeV using the NBD method.

into bins with equal number of events. Therefore the total number of bins, N_{bins}, is such that $N_{bins} = Trigger\ Efficiency$.

Since the BBC charge distribution is known to vary with the collision vertex, the centrality classes are defined for different z vertex values. For Run-7 and Run-10, the vertex was divided into 12 bins in 5 cm increments from -30 cm to +30 cm.

Determination of Glauber Parameters

Once the centrality classes are defined, MC Glauber simulation is used to obtain the geometric quantities $< N_{part} >$, $< N_{coll} >$, and $<\overline{R}>$ at each centrality class, and for each run. Figure 4.7 shows a representative distribution of N_{part} and $\overline{R}$ as obtained in different centrality bins. < ... > here denotes that this is the averaged quantity for all events. Tables 4.4, 4.5, and 4.6 gives a summary of the input parameters used for the simulation.

$Radius$	$Diffuseness$	$Inelastic\ nucleon - nucleon\ cross - section$	$Total\ nucleon - nucleon\ cross - section$
4.21 fm	0.598 fm	42 mb	40 mb

Table 4.4.: Woods-Saxon input parameters used in MC Glauber simulation for Run-5 $Cu + Cu$ $\sqrt{s_{NN}} = 200$ GeV.

$Radius$	$Diffuseness$	$Inelastic\ nucleon - nucleon\ cross - section$	$Total\ nucleon - nucleon\ cross - section$
6.38 fm	0.54 fm	34 mb	40 mb

Table 4.5.: Woods-Saxon input parameters used in MC Glauber simulation for Run-7 and Run-10 $Au + Au$.

$Radius$	$Diffuseness$	$Inelastic\ nucleon - nucleon\ cross - section$	$Total\ nucleon - nucleon\ cross - section$
6.38 fm	0.54 fm	42 mb	40 mb

Table 4.6.: Woods-Saxon input parameters used in MC Glauber simulation for Run-8 $Au + Au$ $\sqrt{s} = 200$ GeV with the deuteron described using a Hulthén wave function [74].

Tables 4.7, 4.8, 4.9, 4.10, and 4.11 show the Glauber parameters for Run-5, Run-7, and Run-10 in 10% centrality bins, as well as Run-8 in 20% centrality bins.

4.3. Event Selection

For the analysis detailed in this thesis, events were selected with the following global parameters of centrality and collision vertex.

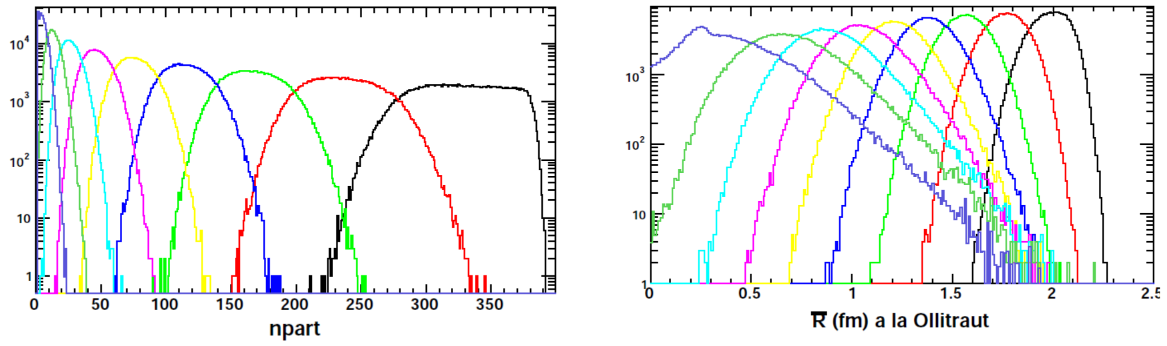

(a) N_{part} as determined for 10% centrality bins. (b) $\overline{R}$ as determined for 10% centrality bins.

Figure 4.7.: MC Glauber parameters for different centrality bins (shown in color) in $Au+Au$ Run-7 $\sqrt{s_{NN}}$ =200 GeV.

Centrality bin %	$< N_{part} >$	$< N_{coll} >$
0–10	98.2 (2.4)	182.7 (20.7)
10–20	73.6 (2.5)	121.1 (13.6)
20–30	53.0 (1.9)	76.1 (8.5)
30–40	37.3 (1.6)	47.1 (5.3)
40–50	25.4 (1.3)	28.1 (3.4)
50–60	16.7 (0.9)	16.2 (1.9)
60–70	10.4 (0.6)	9.0 (1.0)
70–80	6.4 (0.5)	4.9 (0.6)
80–92	3.6 (0.3)	2.4 (0.3)

Table 4.7.: Glauber parameters for $\sqrt{s_{NN}} = 200$ GeV $Cu + Cu$ in Run-5. Systematic errors are shown in parentheses.

Centrality bin %	$< N_{part} >$	$< N_{coll} >$
0–20	15.6 (0.9)	14.9 (1.1)
20–40	11.1 (0.6)	10.4 (0.7)
40–60	7.7 (0.4)	6.9 (0.5)
60–88	4.2 (0.3)	3.2 (0.4)

Table 4.8.: Glauber parameters for $\sqrt{s} = 200$ GeV $d + Au$ in Run-8. Systematic errors are shown in parentheses.

Centrality bin %	$< N_{part} >$	$< N_{coll} >$
0–10	325.8 (3.81)	960.2 (96.14)
10–20	236.1 (5.517)	609.5 (59.81)
20–30	167.6 (5.811)	377.6 (36.39)
30–40	115.5 (5.841)	223.9 (23.2)
40–50	76.15 (5.502)	124.6 (14.94)
50–60	47.07 (4.726)	63.9 (9.359)
60–70	26.72 (3.669)	29.75 (5.41)
70–80	13.67 (2.492)	12.55 (2.822)
80–90	6.153 (1.359)	4.688 (1.252)

Table 4.9.: Glauber parameters for $\sqrt{s_{NN}} = 200$ GeV $Au + Au$ in Run-7. Systematic errors are shown in parentheses.

Centrality bin %	$< N_{part} >$	$< N_{coll} >$
0–10	319.6 (4.093)	843 (100.5)
10–20	229.7 (4.501)	535.8 (58.1)
20–30	163.8 (4.99)	337.2 (32.89)
30–40	113.4 (4.711)	203.3 (20.07)
40–50	74.64 (3.659)	114.3 (11.83)
50–60	45.19 (3.358)	57.78 (6.693)
60–70	24.06 (2.559)	25.2 (3.538)
70–86	8.034 (0.7579)	6.608 (0.7984)

Table 4.10.: Glauber parameters for $\sqrt{s_{NN}} = 62$ GeV $Au + Au$ in Run-10. Systematic errors are shown in parentheses.

Centrality bin %	$< N_{part} >$	$< N_{coll} >$
0–10	316.6 (4.346)	777.2 (94.99)
10–20	227.2 (5.273)	496.7 (54.84)
20–30	161.7 (5.377)	313.8 (31.91)
30–40	112.2 (4.491)	191 (21.16)
40–50	73.77 (4.181)	108.1 (12.74)
50–60	44.83 (3.17)	55.39 (6.291)
60–70	23.68 (3.298)	24.15 (4.385)
70–86	7.71 (1.362)	6.198 (1.404)

Table 4.11.: Glauber parameters for $\sqrt{s_{NN}} = 39$ GeV $Au + Au$ in Run-10. Systematic errors are shown in parentheses.

4.3.1. Run-5 200 GeV $Cu + Cu$

- Centrality range: 0–92%
- |bbcz|<30cm

4.3.2. Run-7 200 GeV $Au + Au$

- Centrality range: 0–92%
- |bbcz|<30cm

4.3.3. Run-8 200 GeV $d + Au$

- Centrality range: 0–88%
- |bbcz|<30cm

4.3.4. Run-10 39 GeV and 62 GeV $Au + Au$

- Centrality range: 0–86%
- |bbcz|<30cm

4.4. Track Selection

4.4.1. Background rejection by matching cuts

Once tracks are reconstructed in the DC and $PC1$, as detailed in section chapter 3, they are projected to the outer detectors. To suppress background (resulting from ghost tracks and other erroneously reconstructed tracks), a requirement is made that each projected track should have an associated cluster hit in the outer detectors. This process is known as track matching.

To obtain the associated hit on a projected track, an area around the intersection point is scanned for possible track hits. The track hit closest to the projected track becomes the the associated track. A matching distribution is built from the difference between the projected hit and the associated hit. This is done in both the ϕ and z coordinates. The mean and width of the distribution are extracted using a Gaussian fit and parameterized as a function of p_T. From the fit parameters of the mean and width of the matching distribution, sigmalized variables are calculated as:

$$sdz = \frac{dz - < dz >}{\sigma_{dz}} \tag{4.7}$$

$$sdphi = \frac{dphi - < dphi >}{\sigma_{dphi}} \tag{4.8}$$

Radial cuts in σ were applied in $PC3$, TOF, and EMC to suppress background. The radial cut is defined as :

$$\sigma_{det} = \sqrt{(sdphi)^2 + (sdz)^2} \tag{4.9}$$

where σ_{det} denotes the sigma value for a particular detector. Therefore, for example, σ_{PC3} is calculated from $pc3sdphi$ and $pc3sdz$.

4.4.2. Summary of track selection cuts

Run-5 200 GeV $Cu+Cu$ and Run-7 200 GeV $Au+Au$

- p_T cut: 0.3–1.0 GeV/c
- Drift Chamber fiducial cut: $|zed|< 75$ cm is applied to the DC to remove edge effects
- RICH *veto* cut: $n_0 \leq 3$. This cut is applied in the $RICH$ detector to suppress electrons misidentified as hadrons; n_0 refers to the number of phototubes that fired in the ring area.
- Matching cut:
  - PC3: ≤ 2.0 σ_{PC3} radial matching
  - EMC: ≤ 2.0 σ_{EMC} radial matching
- Tower cut for EMC (no two tracks with the same tower number for pairs)
- Sector cut in EMC (track pairs were selected within the same sector)

Run-8 200 GeV $d+Au$

- p_T cut: 0.3–1.0 GeV/c
- Drift Chamber fiducial cut: $|zed|< 75$ cm
- RICH *veto* cut: $n_0 \leq 3$.
- Matching cut:
  - PC3: ≤ 3.0 σ_{PC3} radial matching
  - EMC: ≤ 3.0 σ_{EMC} radial matching
- Tower cut for EMC
- Sector cut in EMC

Run-10 62 GeV $Au+Au$

- p_T cut: 0.3–1.0 GeV/c
- Drift Chamber fiducial cut: $|zed|< 75$ cm
- RICH *veto* cut: $n_0 \leq 3$
- Matching cut:

  - PC3: $\leq$2.5 σ_{PC3} radial matching
  - TOF: $\leq$2.0 σ_{TOF} radial matching

- Track selection from TOF east only
- Slat cut (no two tracks with the same slat number for pairs)

Run-10 39 GeV $Au + Au$

- p_T cut: 0.3–1.0 GeV/c
- Drift Chamber fiducial cut: $|zed|<$ 75 cm
- RICH *veto* cut: $n_0 \leq$ 3
- Matching cut: $\leq$2.5 σ_{TOF} radial matching in TOF
- Track selection from TOF east only
- Slat cut

4.5. PID

In PHENIX, PID determination is based on the simultaneous measurement of the momentum in the *DC* and the time-of-flight in the *TOF* or *EMC* detectors.

Particles were identified from the calculated mass-squared (m^2) distribution

$$m^2 = p^2[(\frac{ct}{L})^2 - 1] \tag{4.10}$$

Where p is the particle momentum; t is the time-of-flight as measured by either the TOF detector or the EMC, and where the start time, T_0, is provided by the BBC; L is the length of the time-of-flight as measured from the collision vertex to the hit position in the PID detector; c is the speed of sound.

Pions were then selected for using the number of standard deviations ($\sigma_{measured}$) from which the m^2 deviated from the presumed ideal m^2 of the pion.

$$\sigma^2_{measured} \equiv |m^2_{measured} - m^2_{centroid}| \tag{4.11}$$

$m^2_{centroid}$ is the mass-squared distribution centroid position for the pion peak and $\sigma^2_{measured}$ is the width of the distribution which defines the resolution of the mass-squared distribution. $\sigma^2_{measured}$ depends on both the momentum and resolution σ_p of the *DC* as well as the timing resolution, σ_{tof}, of either *TOF* or *EMC*. σ_p is a combination of the intrinsic angular momentum, σ_α, as well as the angular displacement, σ_s, resulting from multiple scattering of particles within the detector.

4.5.1. PID in TOF

In the TOF detector, the time-of-flight was used to calculate the mass-square distribution (see eqn 4.10). This distribution was then fit with a Gaussian to extract $\sigma_{measured}(p)$, the momentum dependent mass-squared resolution, as well as the centroids for pion, kaon, and protons. The momentum dependent mass-squared sigma was parameterized with the following form:

$$\sigma^2_{m^2} = \frac{\sigma^2_{\alpha^2}}{K_1^2}(4m^4p^2) + \frac{\sigma^2_s}{K_1^2}[4m^4(1 + \frac{m^2}{p^2})] + \frac{\sigma^2_{tof}c^2}{L^2}4p^2(m^2 + p^2) \tag{4.12}$$

from this paramaterization, the timing resolution, σ_{tof}, was found to be about 120 ps.

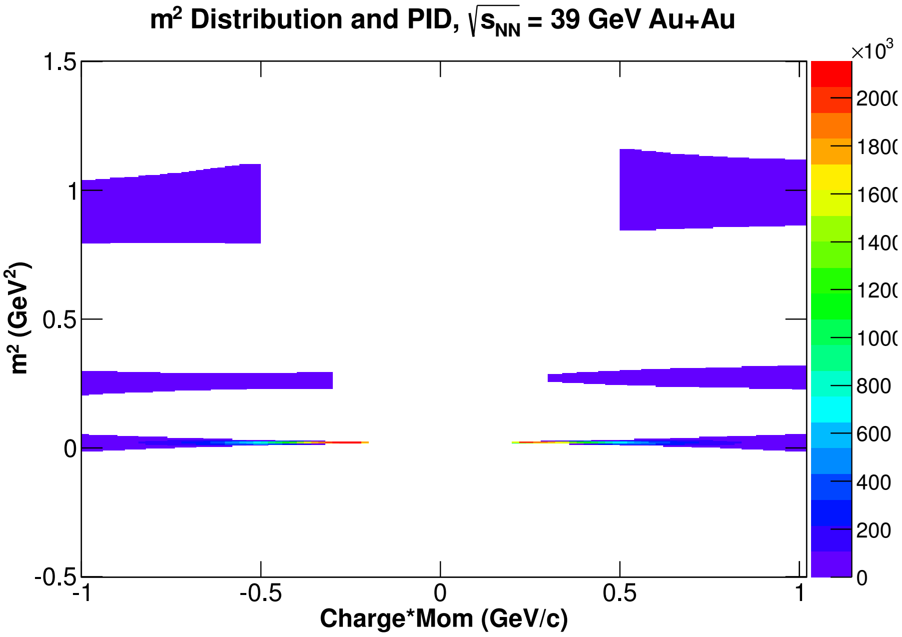

Figure 4.8.: m^2 distribution and PID for $\sqrt{s_{NN}} = 39$ GeV $Au + Au$.

In this analysis, the TOF detector was used for PID in Run-10 39 and 62 GeV. The m^2 plots for the two energies, which demonstrate very good particle separation, are shown in Figures 4.8 and 4.9.

4.5.2. PID in EMC

To obtain the m^2 resolution for EMC and consequently the PID, it is necessary to first know the timing resolution for hadrons. The process involved three main corrections to the EMC measured time-of-flight, t_{EMC}:

1. *Run-by-run correction* This involved shifting the centroid of the difference between the measured time-of-flight to the expected time-of-flight for pions to zero $\Delta t_{run-by-run} = t_{EMC} - t(expected\, for\, \pi)$. The Δt distribution was fitted with a Gaussian and the Gaussian centroid was used as the run-by-run correction to t_{EMC}.

2. *Time slewing (time walk) correction* Time slewing is a feature commonly found in timing detection systems where there is a variation of the output time signal with the input signal amplitude. To correct for this, the difference was found between the

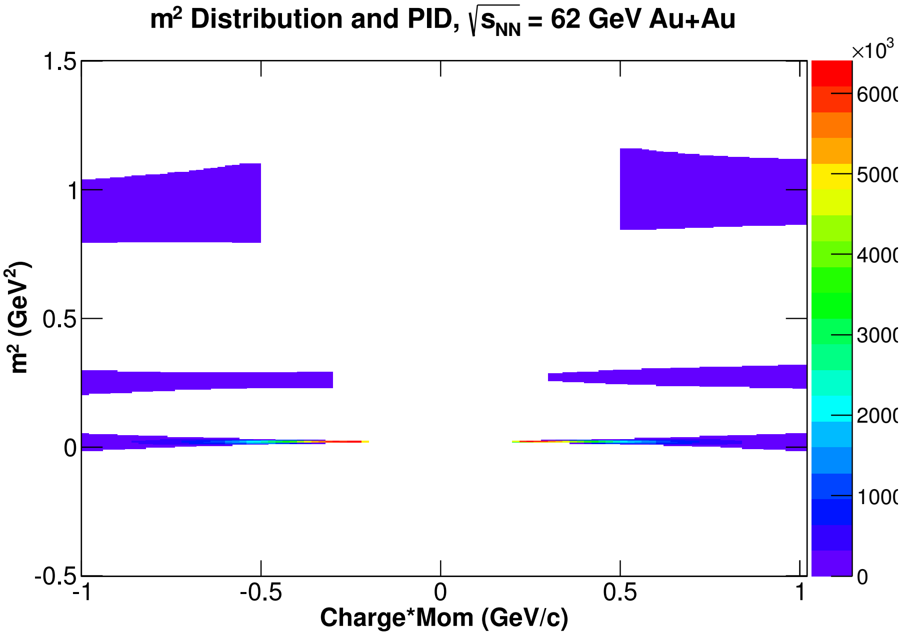

Figure 4.9.: m^2 distribution and PID for $\sqrt{s_{NN}} = 62$ GeV $Au + Au$.

time-of-flight, corrected for run-by-run variation, and the expected time-of-flight, i.e., $\Delta t_{slewing} = t_{EMC}(run\, corrected) - t(expected\, for\, \pi)$. This distribution was fit with a Gaussian to extract the centroid that was then used as a correction to t_{EMC}.

3. *Momentum correction on* t_{EMC} A momentum dependent distribution of the timing offset was obtained after applying the slewing correction, i.e, $\Delta t(p) = t_{EMC}(slewingcorr.) - t(exp.\, for\, \pi)$. This distribution was also fit with a Gaussian to extract the centroid and parameterized to obtain the momentum dependent timing correction. The final corrected t_{EMC} is given by $t_{EMC}^{corrected} = t_{EMC}(with\, slewing\, corr.) - f_p$, where f_p is the momentum dependent correction.

Using the corrected t_{EMC}, the mass-squared distribution was obtained using equation 4.10. This distribution was fit with triple Gaussians for the pion, kaon, and proton peaks to get the mass-squared centroid and the resolution, $\sigma_{measured}$. Particles were selected using a 2.0 $\sigma_{measured}$ cut for pions and with an additional 3.0 $\sigma_{measured}$ rejection cut for kaons to ensure a clean PID.

Figures 4.10, 4.11, and 4.12 show m^2 plots for 200 GeV $Cu+Cu$, $Au+Au$, and $d+Au$ with PID in the EMC. Very good particle separation was obtained in all three systems

4.6. Correlation Functions

In experiment, the Bose-Einstein signal is obtained by taking the ratio of the two-particle inclusive spectra to the product of the two single-particle inclusive spectra. The two-particle inclusive spectra is obtained from pairing same-charge pions taken from the same event. For the single-particle inclusive spectra, we applied the mixing technique. In this method, events used in building the two-particle inclusive spectra are pushed into a pool, classified by their centrality and vertex. Same charge pions are then selected and

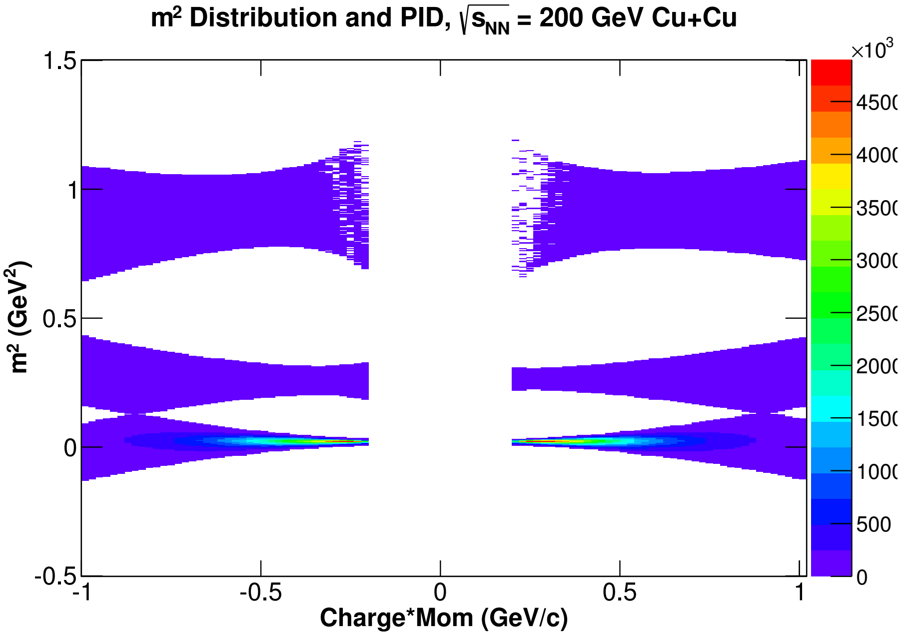

Figure 4.10.: m^2 distribution and PID for $\sqrt{s_{NN}} = 200$ GeV $Cu + Cu$.

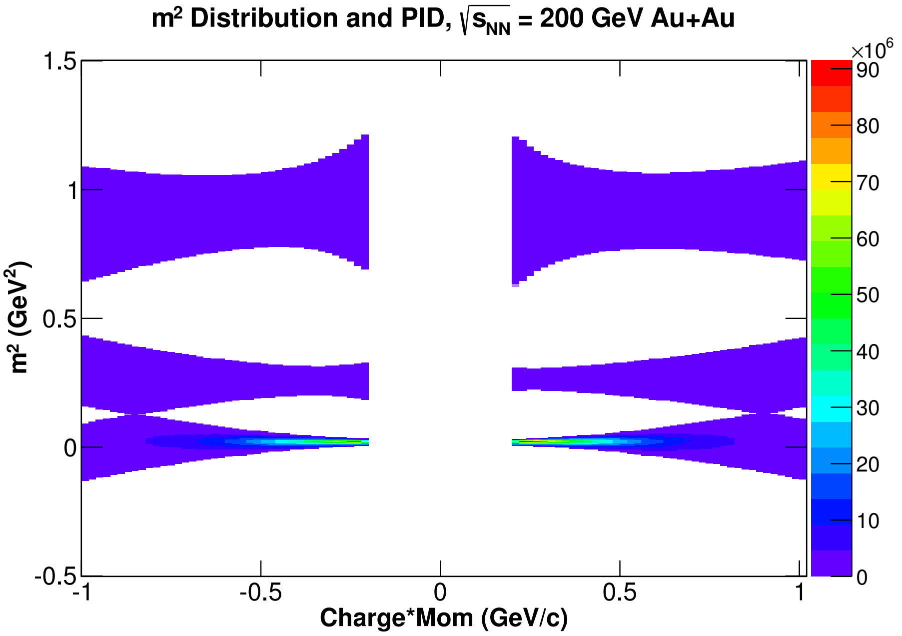

Figure 4.11.: m^2 distribution and PID for $\sqrt{s_{NN}} = 200$ GeV $Au + Au$.

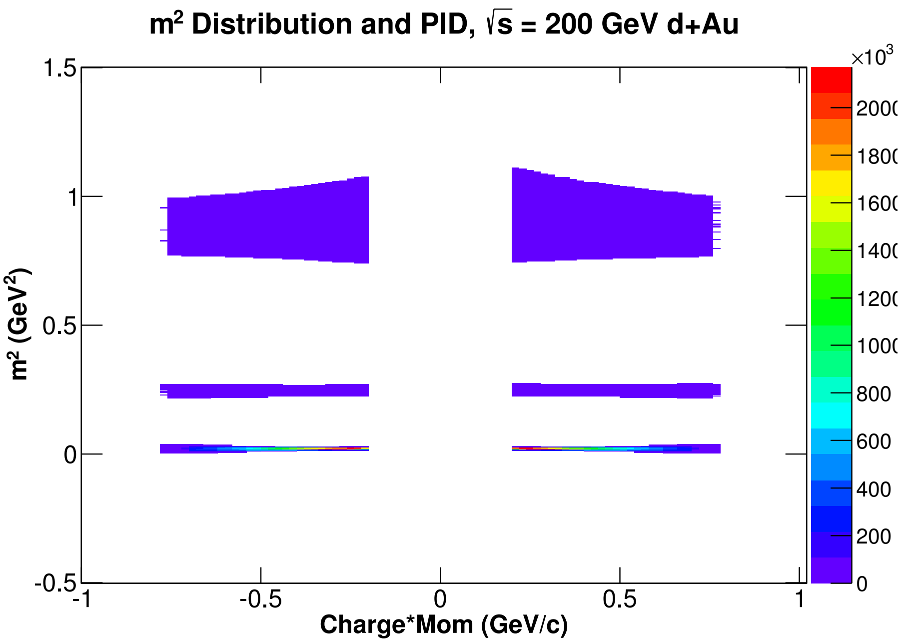

Figure 4.12.: m^2 distribution and PID for $\sqrt{s_{NN}} = 200$ GeV $d + Au$.

paired from different events within the same centrality and vertex class. Once all possible combinations are exhausted from the pool, additional events are added and this is done iteratively for all events utilized for the analysis.

For all energies and collision systems in this study, events were mixed in centrality bins of 5% and bbcz-vertex bins of 3 cm, for a pool depth of 10 events.

$C(q) = \frac{N_{real}}{N_{mixed}}$ where N_{real} is the same-sign charged real pair distribution and N_{mixed} is the same-sign charged mixed pairs distribution.

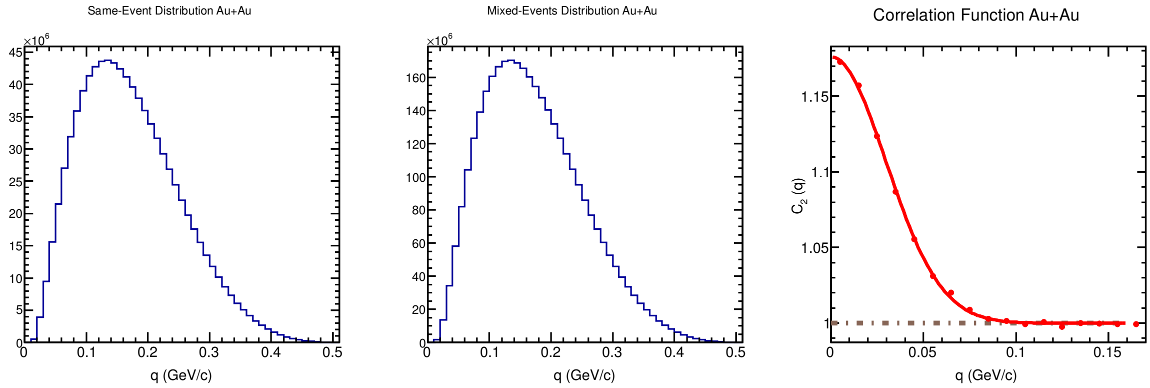

Figure 4.13.: Representation of the real and mixed events distribution. Right most panel is the correlation function $C_2(q)$

4.6.1. Track pair-cut analysis

To remove spurious correlations and other anomalies that degrade the Bose-Einstein signal, it was important to do a thorough analysis of the detection efficiency in different subsystems. Details of how inefficiencies both in detection as well as track reconstruction, and how they were accounted for, are provided in this section.

Track splitting

While the track reconstruction algorithm is highly efficient, it will on occasion reconstruct a track multiple times. These duplicated tracks, known as ghost tracks, share the same physical characteristics as the real track. Particle pairs with ghost tracks will therefore be highly correlated which leads to an artificial enhancement of the Bose-Einstein correlation signal. Since the pairs formed from ghost tracks congregate at small phase-space, one can study, identify, and remove these tracks by building 2-D correlation functions in the $\Delta\phi$:Δz space. $\Delta\phi$ is the difference in ϕ between the tracks in a pair and Δz is the difference in their z-coordinate.

$\Delta z_{DC} = |z_{DC}(track\,1) - z_{DC} track\,2|$

$\Delta\phi_{DC} = |\phi_{DC}(track\,1) - \phi_{DC} track\,2|$

A detailed study of the $\Delta\phi_{DC}$:Δz_{DC} correlation functions was done for the three energies and three collision systems studied to identify and remove ghosting. For each energy and collision system, several cuts were studied for their effect on the resulting correlation function. The idea was to apply cuts such that one sufficiently suppresses the ghosting without in the process also suppressing the desired Bose-Einstein signal. The selected cuts in *DC* are shown in Figures 4.14, 4.15, 4.16, 4.17, and 4.18, while details of the contribution of the different pair-cuts to the systematics are given in section 4.8.

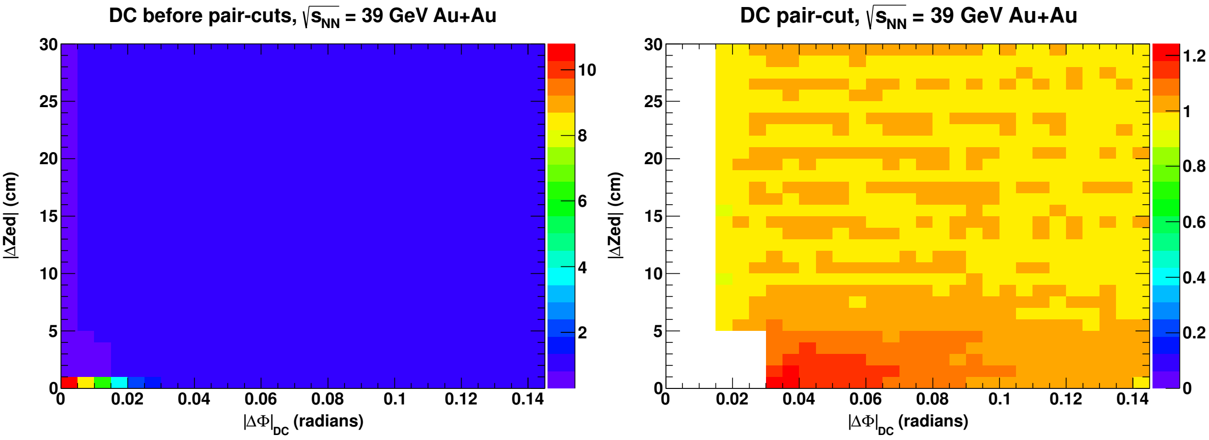

Figure 4.14.: *DC* $\Delta\phi_{DC}$:Δz_{DC} correlation function in $\sqrt{s_{NN}}$ = 39 GeV $Au + Au$ before cuts (left) and with the selected cut (right).

The studies were done for different centrality selections but there was no strong centrality dependence found in any of the energies or collision systems. The $\Delta\phi_{DC}$:Δz_{DC} cuts are therefore applied uniformly across all centralities.

Track Merging

Due to limitations in the detector resolution, tracks that are very close together and therefore below the resolving capability of the detector will sometimes be reconstructed as a single track. This is referred to as track merging and it has the effect of artificially depressing the Bose-Einstein signal.

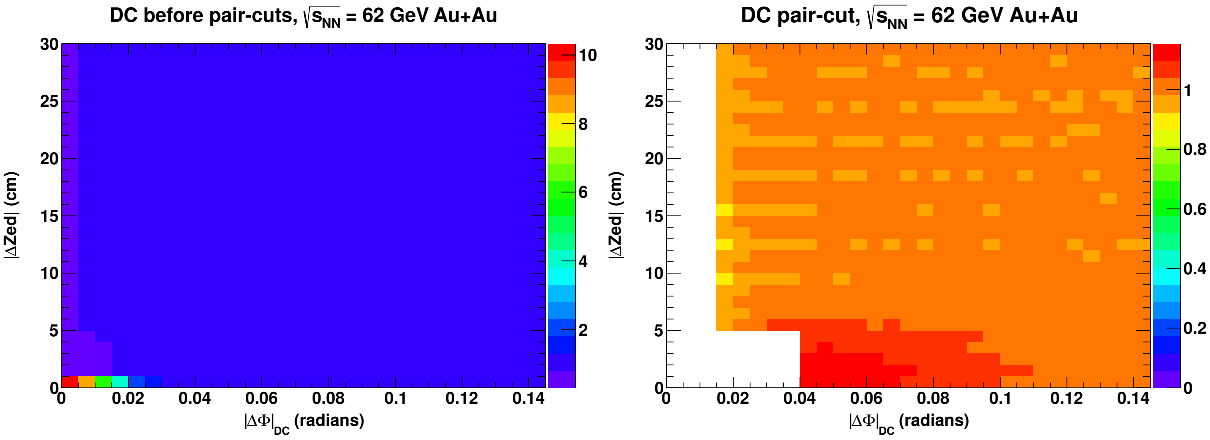

Figure 4.15.: *DC* $\Delta\phi_{DC}$:Δz_{DC} correlation function in $\sqrt{s_{NN}} = 62$ GeV $Au + Au$ before cuts (left) and with the selected cut (right).

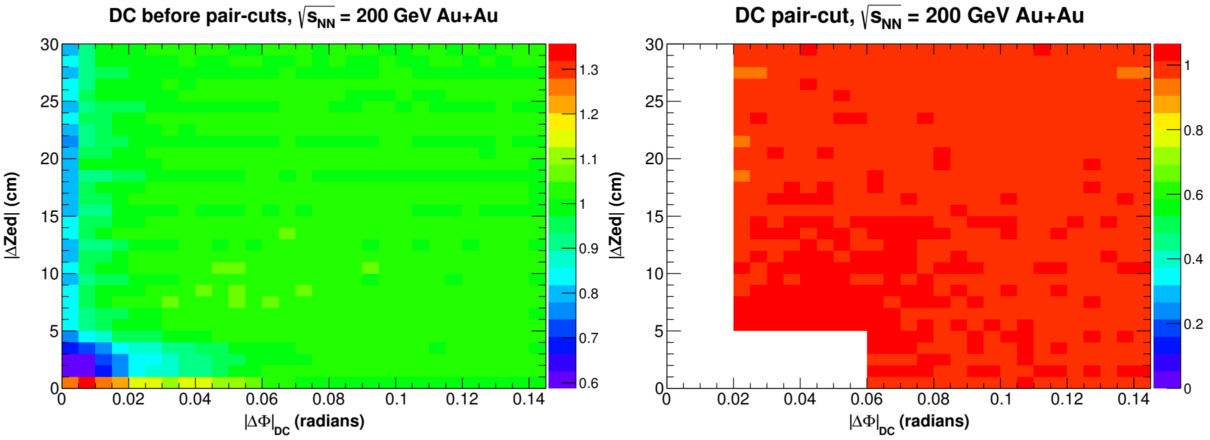

Figure 4.16.: *DC* $\Delta\phi_{DC}$:Δz_{DC} correlation function in $\sqrt{s_{NN}} = 200$ GeV $Au + Au$ before cuts (left) and with the selected cut (right).

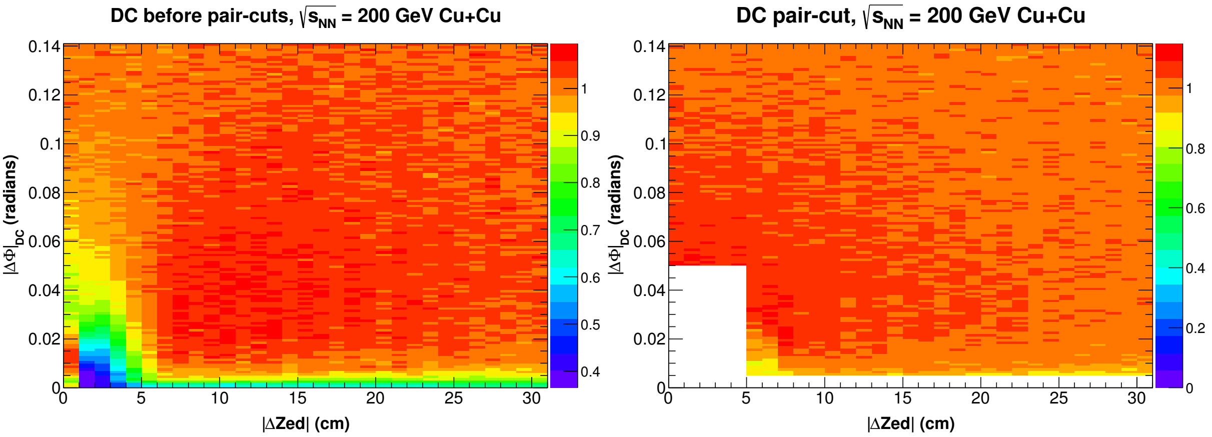

Figure 4.17.: *DC* $\Delta\phi_{DC}$:Δz_{DC} correlation function in $\sqrt{s_{NN}} = 200$ GeV $Cu + Cu$ before cuts (left) and with the selected cut (right).

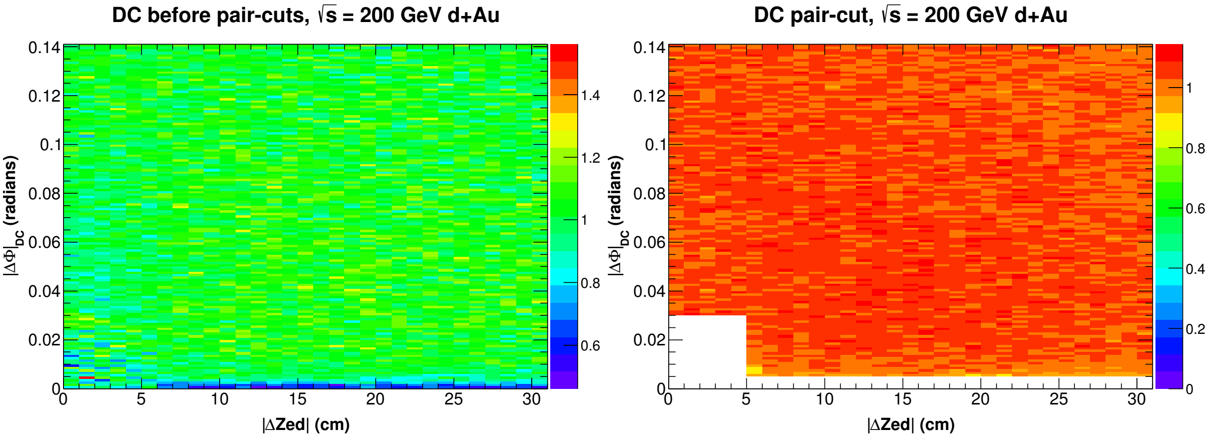

Figure 4.18.: *DC* $\Delta\phi_{DC}$:Δz_{DC} correlation function in $\sqrt{s_{NN}}$ = 200 GeV $d + Au$ before cuts (left) and with the selected cut (right).

Detector inefficiency was investigated in the *DC*, *PC*, *TOF* (for $\sqrt{s_{NN}}$ = 39 and 62 GeV $Au + Au$), and *EMC* (for $\sqrt{s_{NN}}$ = 200 GeV $Au + Au$, $Cu + Cu$, and $d + Au$).

Tracking inefficiency in PC1 In the Pad Chamber, inefficiency was assessed using ΔR_{PC1} which is defined as the relative difference in the track projections to $PC1$ for the particles in the pair.

$$\Delta R_{PC1} = \sqrt{(pPC1x1 - pPC1x2)^2 + (pPC1y1 - pPC1y2)^2 + (pPC1z1 - pPC1z2)^2} \tag{4.13}$$

Where $pPC1xi$, $pPC1yi$, and $pPC1zi$ are the track projections to $PC1$ using the cartesian coordinate system.

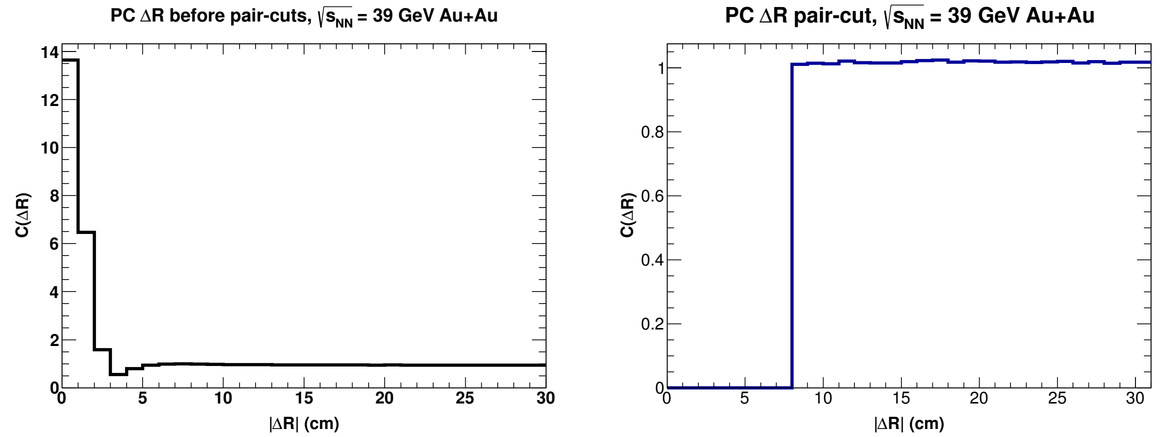

Figure 4.19.: $PC1$ ΔR correlation function in $\sqrt{s_{NN}}$ = 39 GeV $Au + Au$ before applying pair-cuts (left) and with pair-cuts (right).

To get the ΔR_{PC1} correlation function, foreground and background pair distributions in ΔR_{PC1} are built for the same classes in centrality and vertex. Once the optimum cut is identified, it is applied both in the same-event distribution as well as the mixed event distribution to ensure same acceptance. ΔR_{PC1} correlation functions for $\sqrt{s_{NN}}$ = 39 $Au + Au$ (Fig. 4.19), $\sqrt{s_{NN}}$ = 62 $Au + Au$ (Fig. 4.20), $\sqrt{s_{NN}}$ = 200 $Au + Au$ (Fig.

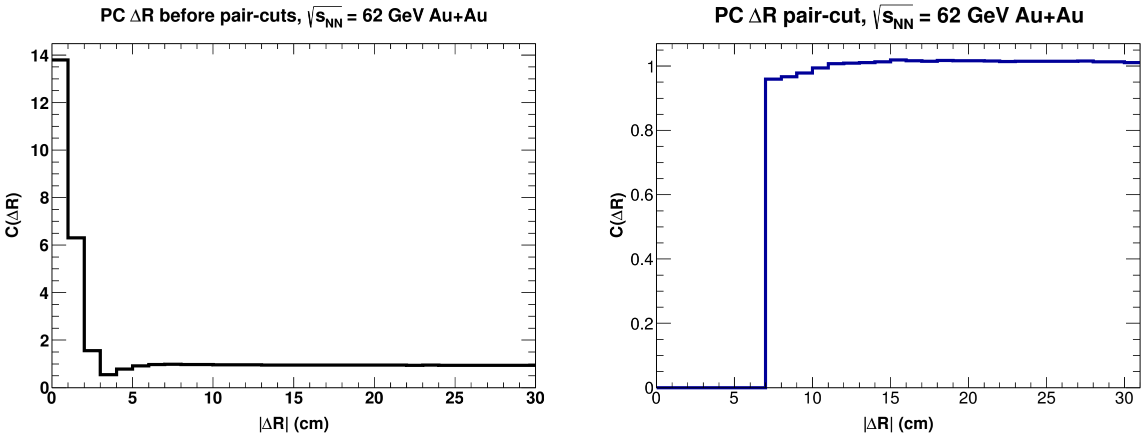

Figure 4.20.: $PC1$ ΔR correlation function in $\sqrt{s_{NN}} = 62$ GeV $Au+Au$ before applying pair-cuts (left) and with pair-cuts (right).

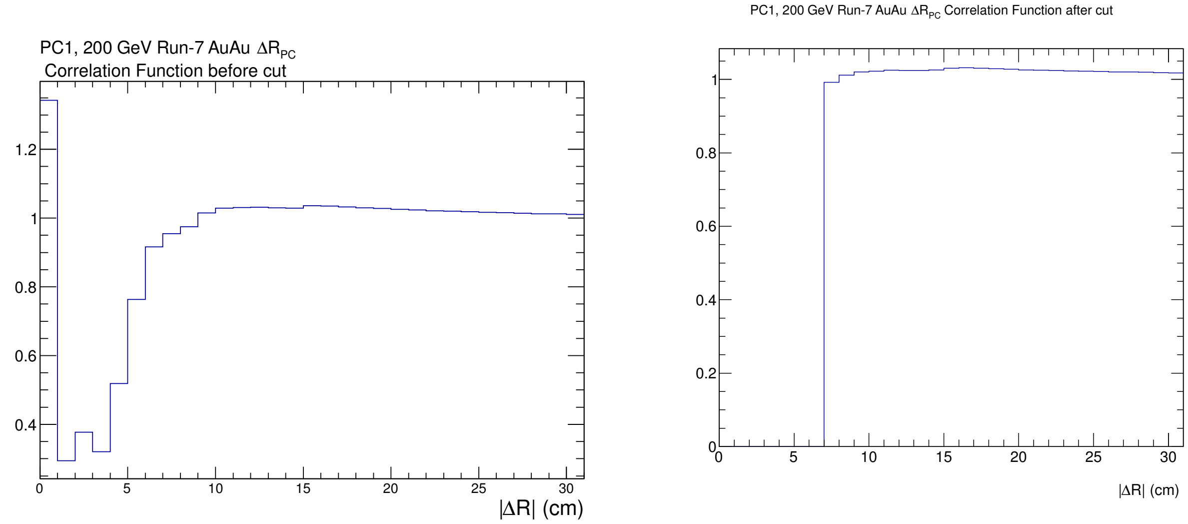

Figure 4.21.: $PC1$ ΔR correlation function in $\sqrt{s_{NN}} = 200$ GeV $Au+Au$ before applying pair-cuts (left) and with pair-cuts (right).

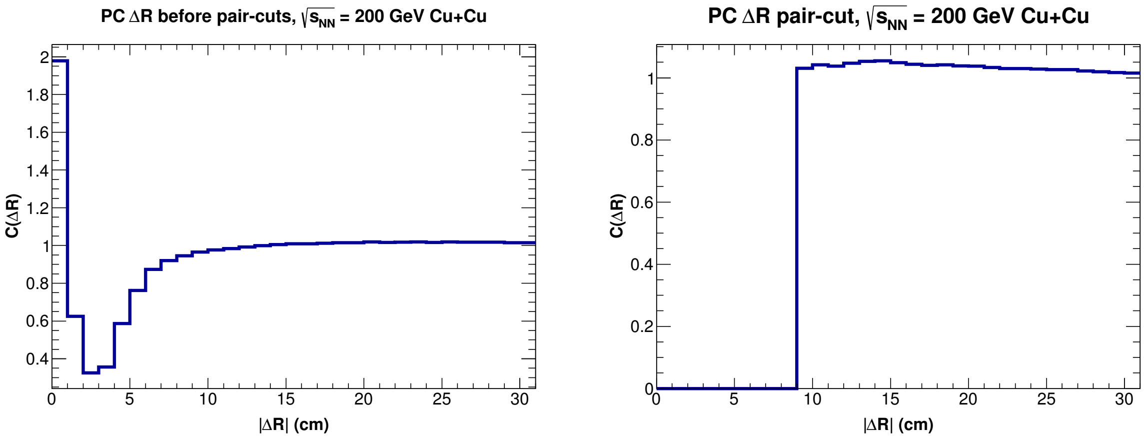

Figure 4.22.: $PC1$ ΔR correlation function in $\sqrt{s_{NN}} = 200$ GeV $Cu+Cu$ before applying pair-cuts (left) and with pair-cuts (right).

4.21), and $\sqrt{s_{NN}} = 200$ $Cu + Cu$ (Fig. 4.22) show the discussed effects of merging seen as a dip in the correlation functions without cuts. A ghosting enhancement can also be seen at small ΔR_{PC1} on the same plots. Appropriate cuts were applied to get rid of both effects, as is shown in the rightmost plots in the above mentioned figures.

Tracking inefficiency in EMC For $\sqrt{s_{NN}} = 200$ GeV Run-5 $Cu + Cu$, $\sqrt{s_{NN}} = 200$ GeV Run-7 $Au + Au$, and $\sqrt{s_{NN}} = 200$ GeV Run-8 $d + Au$ analysis, the EMC was used for the particle identification. To remove autocorrelation and instances where tracks are part of the same cluster leading to ghosting, a requirement was made that the tracks making a pair would have to be from different towers.

In the EMC, inefficiency was investigated by studying the correlation function in the $\Delta\phi_{EMC}$:Δz_{EMC} space.

$\Delta\phi_{EMC}$ and Δz_{EMC} are defined as:

$\Delta\phi_{EMC} = |\phi_{EMC}(track\ 1)\ - \phi_{EMC} track\ 2|$

$\Delta z_{EMC} = |z_{EMC}(track\ 1)\ - z_{EMC} track\ 2|$

ϕ_{EMC} is the phi coordinate of the hit as recorded in the EMC while z_{EMC} is its z coordinate.

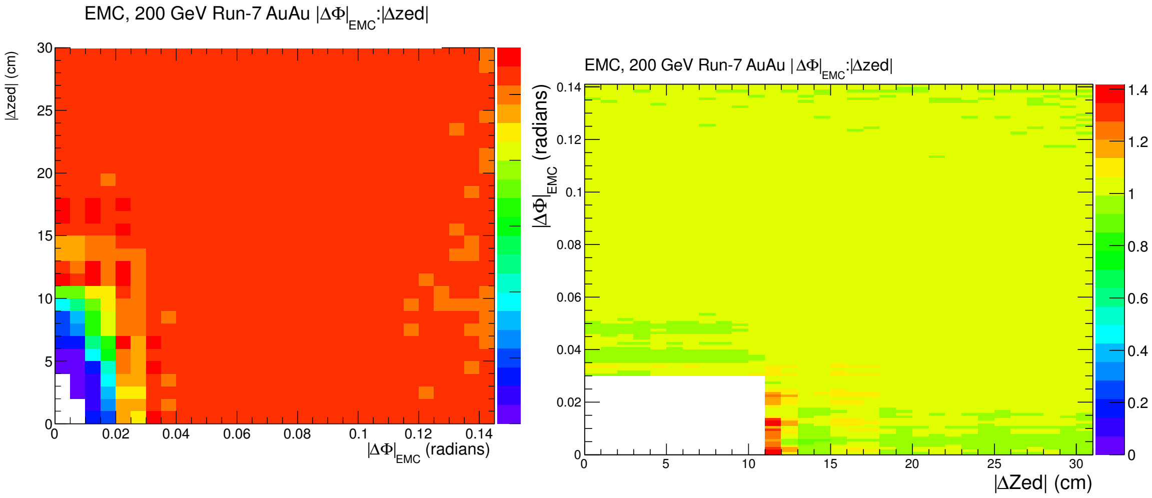

Figure 4.23.: $\Delta\phi_{EMC}$:Δz_{EMC} correlation function in $\sqrt{s_{NN}} = 200$ GeV $Au + Au$ before applying pair-cuts (left) and with pair-cuts (right).

As with the other pair-cuts investigated, the $\Delta\phi_{EMC}$:Δz_{EMC} cuts were studied extensively in different ranges, as well as for their centrality dependence. No centrality dependence was found and therefore the cuts are applied uniformly across all centrality selections. Figures 4.23, 4.24, and 4.25 show the before pair-cuts (leftmost plots) and after pair-cuts (rightmost plots) $\Delta\phi_{EMC}$:Δz_{EMC} correlation functions for $\sqrt{s_{NN}} = 200$ GeV $Au + Au$, $\sqrt{s_{NN}} = 200$ GeV $Cu + Cu$, and $\sqrt{s_{NN}} = 200$ GeV $d + Au$ respectively.

Tracking inefficiency in TOF Pions for the low energy runs of $\sqrt{s_{NN}} = 39$ and 62 GeV were identified in the TOF detector. To account for tracking inefficiency, studies were done of ΔR_{TOF} which is the relative difference in the track projections to the TOF detector, i.e.

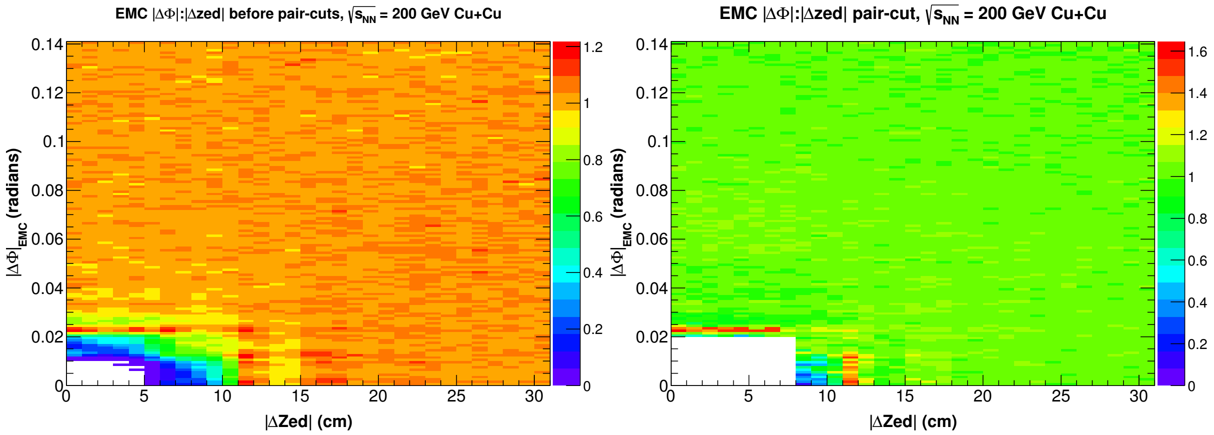

Figure 4.24.: $\Delta\phi_{EMC}$:Δz_{EMC} correlation function in $\sqrt{s_{NN}}$ = 200 GeV $Cu + Cu$ before applying pair-cuts (left) and with pair-cuts (right).

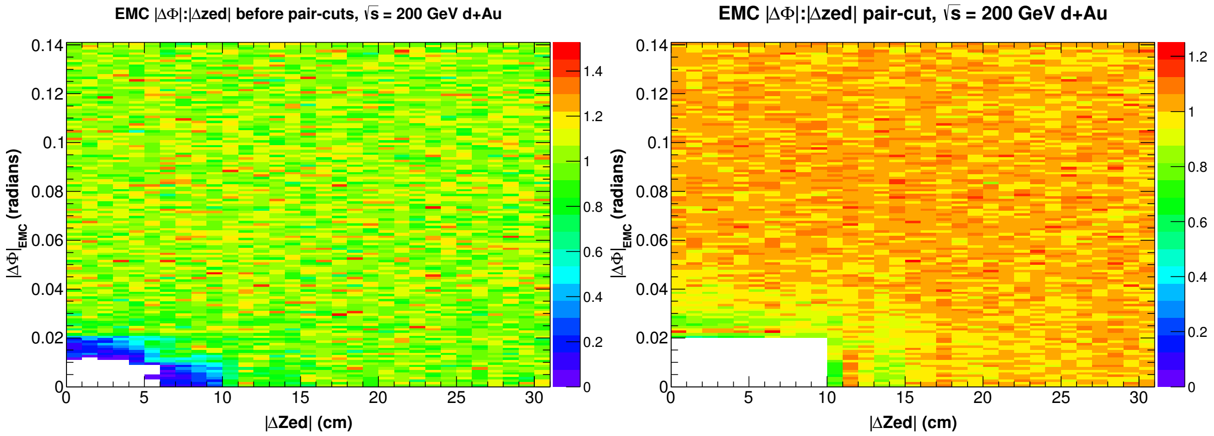

Figure 4.25.: $\Delta\phi_{EMC}$:Δz_{EMC} correlation function in $\sqrt{s_{NN}}$ = 200 GeV $d + Au$ before applying pair-cuts (left) and with pair-cuts (right).

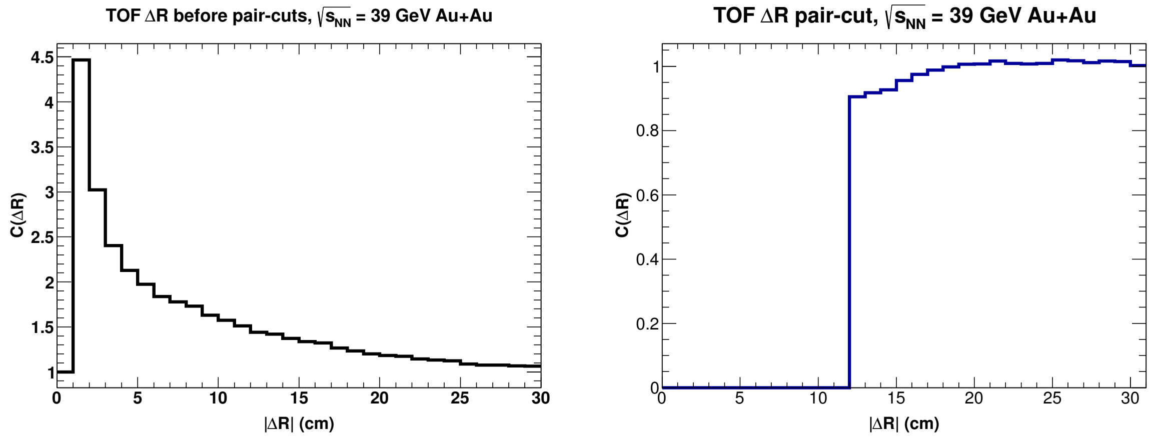

Figure 4.26.: ΔR_{TOF} correlation function in $\sqrt{s_{NN}}$ = 39 GeV before applying pair-cuts (left) and after applying pair-cuts (right).

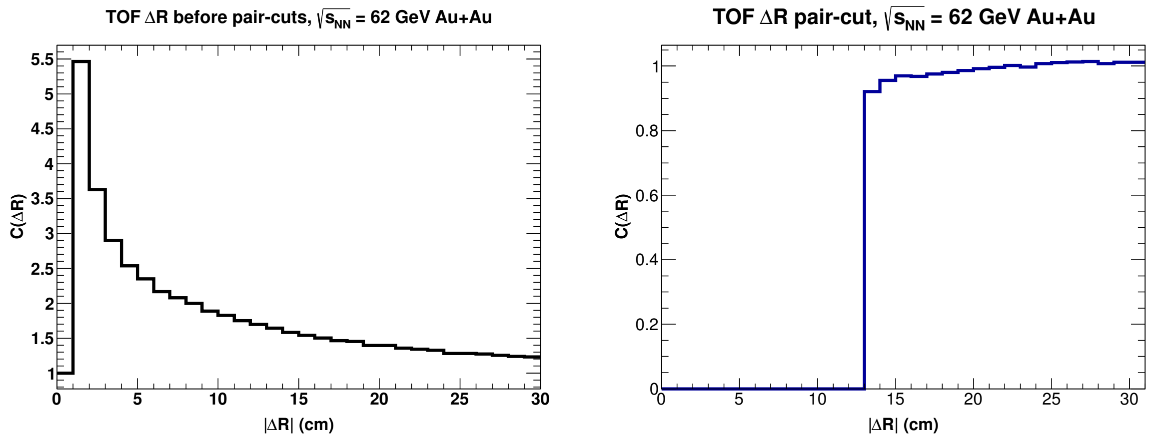

Figure 4.27.: ΔR_{TOF} correlation function in $\sqrt{s_{NN}}$ = 62 GeV before applying pair-cuts (left) and after applying pair-cuts (right).

$$\Delta R_{TOF} = \sqrt{(pTOFx1 - pTOFx2)^2 + (pTOFy1 - pTOFy2)^2 + (pTOFz1 - pTOFz2)^2} \tag{4.14}$$

Where $pTOFxi$, $pTOFyi$, and $pTOFzi$ are the projections to TOF of single tracks in the cartesian coordinate system.

Figures 4.26 and 4.27 show the ΔR_{TOF} correlation function before and after applying cuts to remove the inefficiency at small ΔR_{TOF}.

Run-5 200 GeV $Cu + Cu$ summary of pair-cuts

- Drift Chamber cuts: $|\Delta\phi| < 0.005$ rad for $|\Delta zed| < 60$ cm and $|\Delta\phi| < 0.05$ rad for $|\Delta zed| < 5$ cm
- $PC1$ cuts: $\Delta R_{PC1} < 9$ cm
- EMC cuts: $\Delta\phi_{EMC} : \Delta zed$:$|\Delta\phi_{EMC}| < 0.02$ rad for $|\Delta zed| < 8$ cm

Run-7 200 GeV summary of pair-cuts

- Drift Chamber cuts: $|\Delta\phi| < 0.02$ rad for $|\Delta zed| < 60$ cm and $|\Delta\phi| < 0.06$ rad for $|\Delta zed| < 5$ cm
- $PC1$ cuts: $\Delta R_{PC1} < 7$ cm
- EMC cuts: $\Delta\phi_{EMC} : \Delta zed$:$|\Delta\phi_{EMC}| < 0.03$ rad for $|\Delta zed| < 11$ cm

Run-8 200 GeV $d + Au$ summary of pair-cuts

- Drift Chamber cuts: $|\Delta\phi| < 0.005$ rad for $|\Delta zed| < 60$ cm and $|\Delta\phi| < 0.03$ rad for $|\Delta zed| < 5$ cm
- EMC cuts: $\Delta\phi_{EMC} : \Delta zed$:$|\Delta\phi_{EMC}| < 0.02$ rad for $|\Delta zed| < 10$ cm

Run-10 62 GeV summary of pair-cuts

- Drift Chamber cuts: $|\Delta\phi| < 0.015$ rad for $|\Delta zed| < 60$ cm; $|0.04|$ rad for $|\Delta zed| < 5$ cm
- $PC1$ cuts: $\Delta R_{PC1} < 7$ cm
- TOF cuts: $\Delta R_{TOF} < 13$ cm

Run-10 39 GeV summary of pair-cuts

- Drift Chamber cuts: $|\Delta\phi| < 0.015$ rad for $|\Delta zed| < 60$ cm, $|0.03|$ rad for $|\Delta zed| < 5$ cm
- $PC1$ cuts: $\Delta R_{PC1} < 8$ cm
- TOF cuts: $\Delta R_{TOF} < 12$ cm

4.7. Coulomb Correction

At small separations, in the order in which we see significant Bose-Einstein effects, Final State Interactions (FSI) also become significant. In the case of same-charge two-pion intereference, FSI are dominated by Coulomb repulsion, strong interactions been negligible (see discussion on this in the introduction section). Coulomb repulsion serves to suppresss the Bose-Einstein signal and therefore must be corrected for.

In this analysis, we use a commonly applied procedure to correct for Coulomb interaction at small q [38]. The Coulomb correction is calculated by integrating the squared Coulomb wave function from an assumed Gaussian source. More precisely, we assume our pion source is a volume with a Gaussian distribution and a radius of 5 fm. Pion pairs are assigned random positions in this volume and the Coulomb strength between each pair is calculated using the Coulomb wave function. We then integrate and average over a given number of points in the volume, in this case 20 points. Previous studies have found that these number of sampling points provided a sufficient measure of the Coulomb strength [60]. The Coulomb strength is calculated in the pair center-of-mass frame and therefore takes as inputs an estimate of R_{inv} (5 fm) as well as q_{inv}. The q_{inv} values were obtained by generating a histogram with the mean values of q_{inv} calculated for each bin of q_{side}, q_{out}, and q_{long}.

The correction factor is taken as the ratio of the pair distribution in q_{inv} with the Coulomb correction to a similar pair distribution in q_{inv} without the Coulomb correction.

The core-halo model

Studies have shown that the pion emitting source can be considered as consisting of two parts: The core and the halo [56]. The core is made up of primary pions that are products of the hydrodynamic evolution of the system followed by re-scattering. Surrounding the core is the halo which consists of pion products from the decay of long-lived resonances like K^0, η, η', and ω. Due to their extended mean-decay-length (>20 fm), the halo is characterized by pions of similar momentum found over a very large volume [90]. The core-halo model becomes crucial in the application of the Coulomb correction to the correlation function.

Sinyukov correction procedure

In past HBT studies, the Coulomb effect was accounted for by applying the correction factor uniformly over the measured correlation function in the so called full Coulomb correction method i.e.,

$$C(q) \; = \; K(q)C^{measured}(q) \tag{4.15}$$

$K(q)$ is the correction factor that only depends on q and $C^{measured}(q)$ is the measured correlation function.

Based on the core-halo model, one can argue that the pions produced as decay products of long-lived resonances experience an insignificant Coulomb force due to their wide separation. Applying the Coulomb correction uniformly over all pions therefore overcorrects for the Coulomb effect. λ, the chaoticity parameter can be treated in terms of the multiplicity contribution from the core as compared to that from the halo [90],

$$\lambda \; = \; \frac{< n_{core} >^2}{< n_{total} >^2} \tag{4.16}$$

Consequently, the correlation can be decomposed into two parts:

$$C_2^{measured} \; = \; C_2^{core} + C_2^{halo} \tag{4.17}$$

$$C_2(q) \; = \; N[(\lambda(1 + G(q)))F_c + (1 - \lambda)] \tag{4.18}$$

$$G(q) \; = \; exp(-R_{inv}^2 q_{inv}^2) \tag{4.19}$$

F_c is the Coulomb correction part, applied only to the core, and dependent on q, while N is a normalization factor. Figure 4.28 shows an example plot of the Coulomb correction function.

These correction was originally proposed by Sinyukov and is the method used in the Coulomb correction in this study [103].

4.8. Systematic Uncertainity

4.8.1. Pair-cut selection

As mentioned in section 4.6.1, a detailed study of the pair-cuts was done to arrive at the optimal set of cuts used in this analysis. The importance of this cannot be overstated: An insufficient cut that leaves residual ghosting or merging effects will artificially enhance or suppress the Bose-Einstein signal. On the other hand, too large a cut will suppress the signal and reduce the statistics available for the analysis.

The pair-cuts were applied using an inside-out approach, meaning that cuts were first applied to the inner detector before being applied to the outer detector. These was accomplished in the following order:

$$DC \rightarrow PC1 \rightarrow EMC/TOF$$

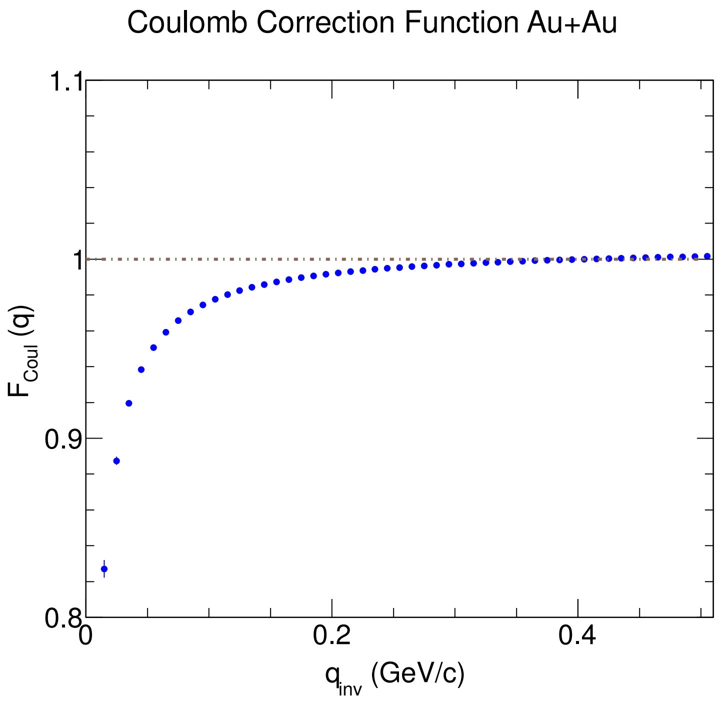

Figure 4.28.: F_{Coul} correction function used in the fit function.

Since the *DC* cuts are applied first, they have the biggest influence on the control of ghosting and merging effects as discussed in section 4.6.1, and a detailed analyis of their effect was of paramount importance.

The approach to the pair-cuts analysis was to select in small increments for cuts in both $\Delta\phi$ and Δz, and study the resulting HBT radii until there was little to no change, within statistical error. The study was done independently for each of the three energies and collision systems.

4.8.2. Systematic error from pair-cuts

The systematic error from pair-cuts was evaluated by varying the cut as detailed in section 4.8.1. The systematic error was calculated by taking the difference in the extracted radii from the largest cut studied to that of the selected cut. This procedure was adopted for the evaluation of the systematic error contribution from cuts in all the detectors.

4.8.3. Systematic error from matching

Errors were studied by varying the matching cut from 2.0 σ in *EMC* and 2.5 σ in *TOF* to 1.0 σ in both *EMC* and *TOF*. In all three beam energies, the contribution of the systematic errors from track matching was about 3% on average.

4.8.4. Systematic errors from PID selection

Systematic errors from PID were determined by varying the pion selection from a 2.0 σ to a 1.0 σ. As with the pair-cut errors, the errors from PID selection were calculated by taking the difference of the extracted radii at 2.0 σ to that at 1.0 σ. These errors were found to be very small, only to about 2% in the different beam energies and collision systems.

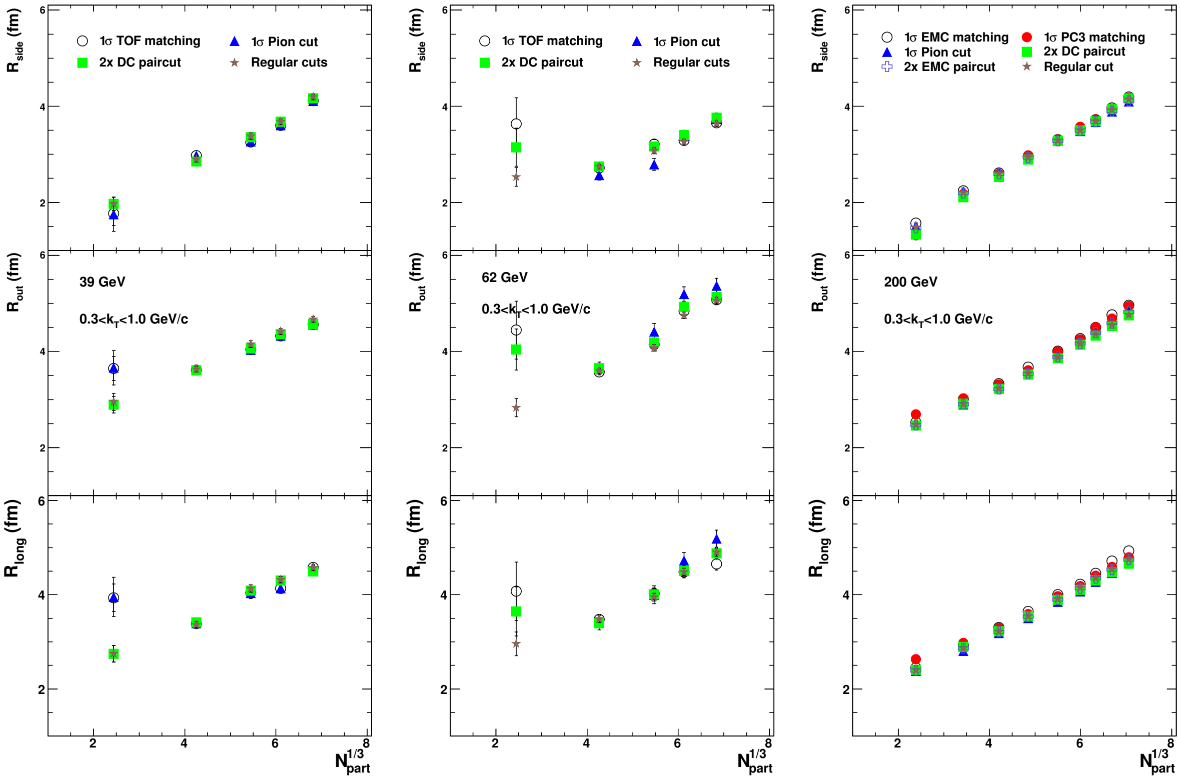

Figure 4.29.: Systematic error analysis for $\sqrt{s_{NN}} = 39$ GeV, 62 and 200 GeV $Au + Au$.

5. Results and Discussion

5.1. Consistency Checks

5.1.1. Consistency check between TOF and EMC for $Au+Au$ at $\sqrt{s_{NN}}$ = 200 GeV

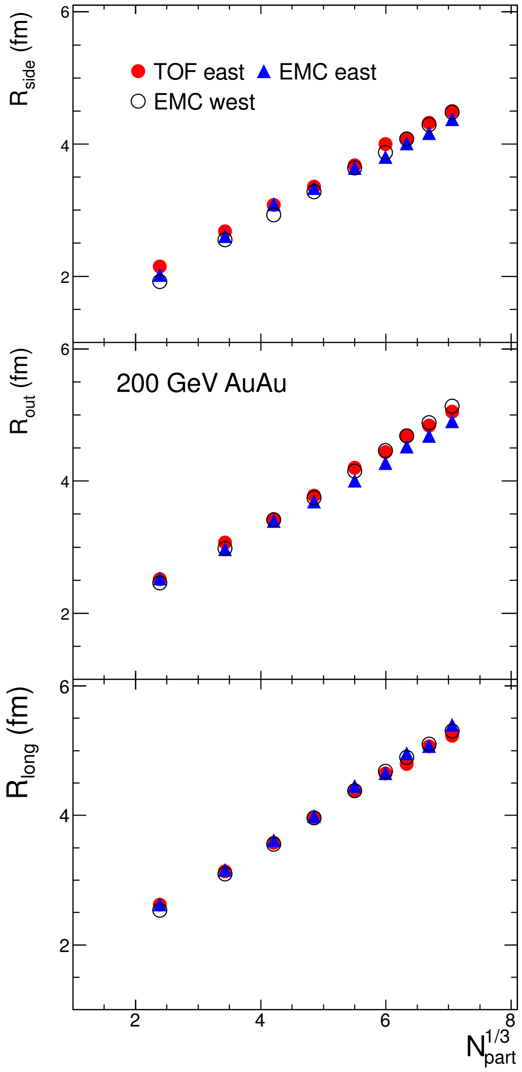

Figure 5.1.: Comparison of HBT measurements for pions identified in TOF, EMC east, and EMC west at $\sqrt{s_{NN}}$ = 200 GeV.

While the TOF east detector provides for better PID capability due to its higher timing resolution, it has a limited acceptance ($\pi/4$ in azimuthal) as compared to the EMC. A comparison between the results from the two subsystems is a necessary check to ensure confidence in the physics results. Figure 5.1 shows HBT radii from pions identified in the two *PbSc* arms of the *EMC*, and compared to HBT radii from PID in the *TOF* east detector. Due to acceptance and callibrations problems with the *TOF* west detector, it was not utilized for this analysis. Results from both arms of the *EMC* compared to the *TOF* east detector show a very good match.

5.1.2. Consistency check with previous PHENIX results for $Au + Au$ at $\sqrt{s_{NN}}$ = 200 GeV

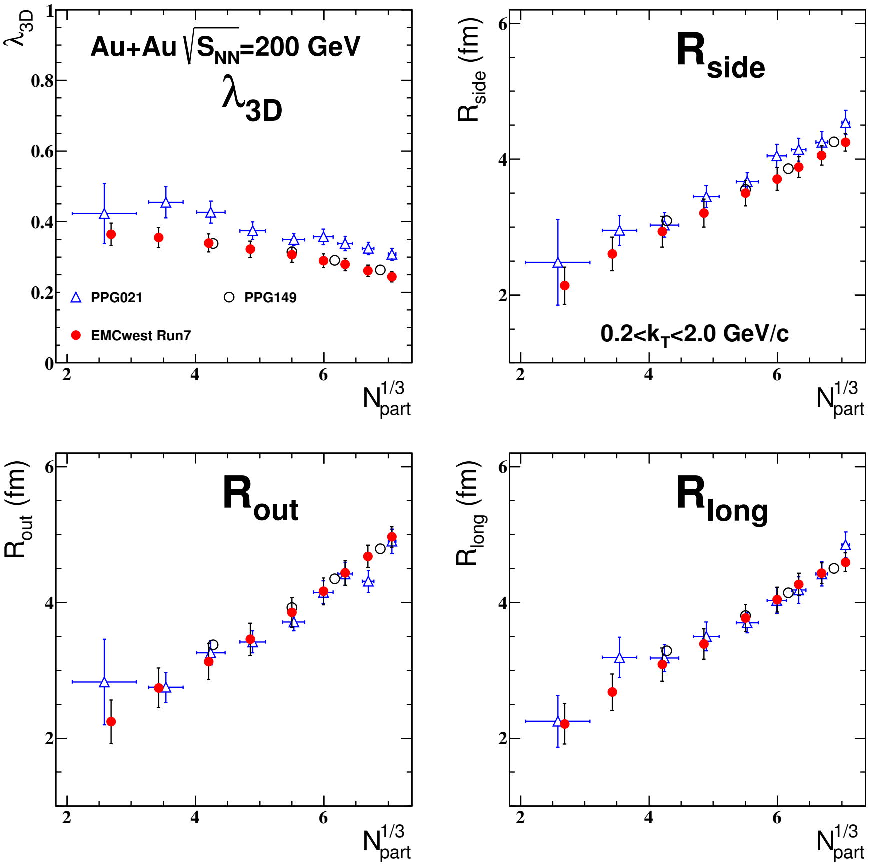

Figure 5.2.: Comparsion of the $N_{part}^{1/3}$ dependence of different PHENIX results at $\sqrt{s_{NN}}$ = 200 GeV.

Figure 5.2 compares $Au + Au$ at $\sqrt{s_{NN}}$ = 200 GeV results from this analysis with PHENIX results from previous studies [22]. A very good match, within systematic error, is found between the two sets of PHENIX results. The increased statistics from the RHIC Run-year 2007 data allowed for a more detailed study of the different dependencies.

5.1.3. Consistency check with previous PHENIX results for $Cu + Cu$ at $\sqrt{s_{NN}}$ = 200 GeV

In figure 5.3, a comparison is done for $Cu + Cu$ at $\sqrt{s_{NN}}$ = 200 GeV results from this analysis and a previous study done at PHENIX (AN Note 565). Both sets of results are

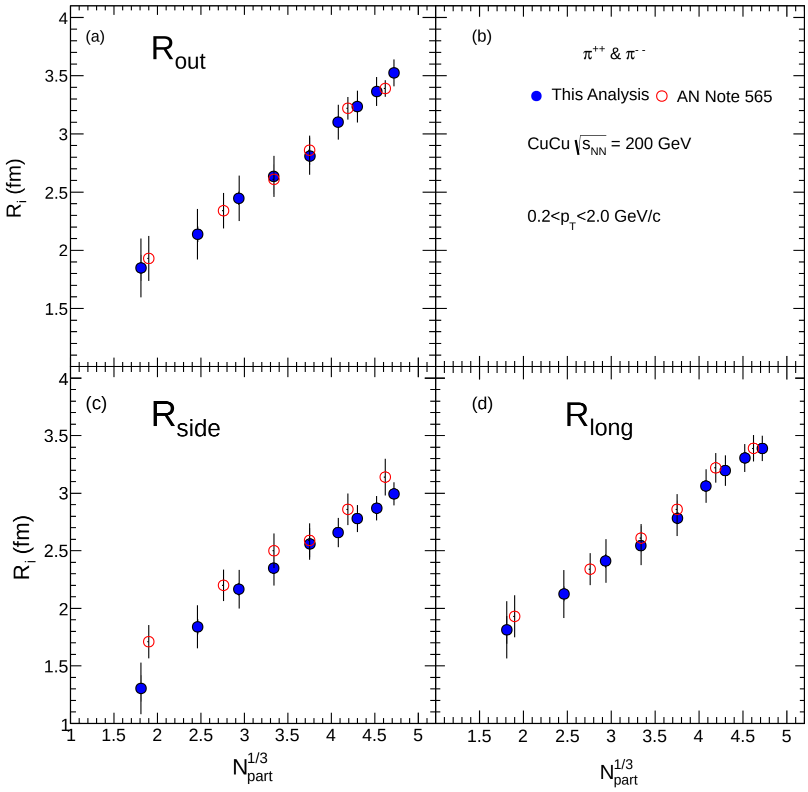

Figure 5.3.: Comparison of these results with previous PHENIX results for $Cu + Cu$ at $\sqrt{s_{NN}} = 200$ GeV.

from RHIC Run-year 2005 but a re-analysis was necessary so as to re-evaluate the cuts as well as obtain new binning for a comparison with the $Au + Au$ data. An excellent match is found in all the HBT parameters to within systematic error.

5.2. Final-State Effects

5.2.1. Collision centrality dependence

The extracted HBT radii was studied for the initial collision geometry dependence in the form of the cube root of the number of participants, $N_{part}^{1/3}$, which acts as a proxy for the initial radius [85].

The $Cu + Cu$ collision system is a much smaller system than the $Au + Au$ (Cu mass number = 63.546 and Au mass number = 196.966) which not only presents a different collision geometry but also the possibility of different expansion dynamics.

Figure 5.4 compares the $Au+Au$ and $Cu+Cu$ collision systems dependence on $N_{part}^{1/3}$ at the same energy of $\sqrt{s_{NN}} = 200$ GeV and a $< k_T > = 0.53$ GeV/c. $Cu+Cu$ demonstrates the same linear dependence with $N_{part}^{1/3}$ as seen in the $Au + Au$ system as well as the same magnitude for similar N_{part} values [7].

In Figure 5.5, a similar comparison of the $d + Au$ and $Au + Au$ systems for the HBT radii dependence on $N_{part}^{1/3}$ is made (panels (a)–(c)).

A comparison of the $d + Au$ and $Au + Au$ systems is especially helpful in providing model constraints to the role of hydrodynamic-driven final-state re-scattering effects in

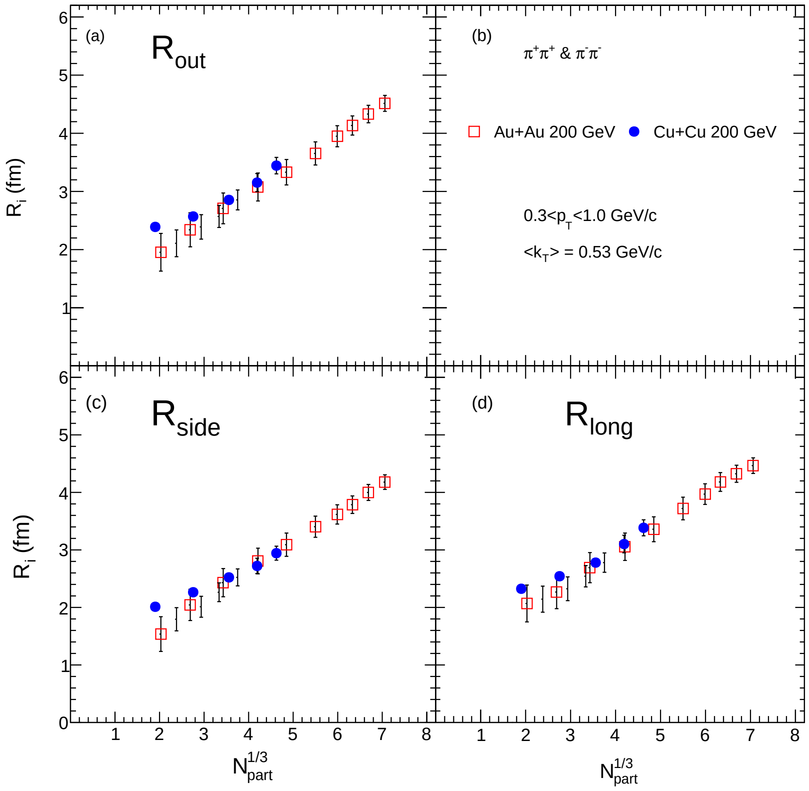

Figure 5.4.: HBT radii for $Cu + Cu$ and $Au + Au$ at $\sqrt{s_{NN}} = 200$ GeV.

the smaller $d + A$ and $p + A$ systems. Here again, a linear increase with $N_{part}^{1/3}$ is observed for the $d+Au$ system but with $Au+Au$ showing a much larger size. While the transverse size shows similar slopes in the two systems, a slight change in the R_{long} slope for $d + Au$ is observed. This difference in slopes can be attributed to differences in longitudinal dynamics between the $d+Au$ and $Au+Au$ systems. The difference in magnitude between the two systems at similar N_{part} values suggests that N_{part} might not be the best variable for studies of initial size in small asymmetric systems.

Panel (d) shows the $(dN/d\eta)^{1/3}$ dependence of the transverse size, R_{side}, for $Au + Au$, $d + Au$, and $p + p$ (at 7 TeV) systems. $dN/d\eta$ is a measure of the number of charged particles at mid-rapidity and therefore studying the HBT radii dependence on $(dN/d\eta)^{1/3}$ provides insight into how the final system size is connected to the particle density at freeze-out [48]. Here too, a linear dependence of R_{side} with $(dN/d\eta)^{1/3}$ is observed in the three systems but with a difference in their magnitudes. The scaling of R_{side} with multiplicity is not at all unexpected since N_{part} also scales with multiplicity [85]. Similar trends in the $(dN/d\eta)^{1/3}$ dependence have been demonstrated for $A+A$ and $p+p$ collision systems [25, 7].

5.2.2. m_T dependence

Studies of the HBT radii dependence on the transverse mass, m_T, can provide us with insight into the expansion dynamics that influence a system.

In this section, I present and discuss the m_T dependence of $Au + Au$, $Cu + Cu$, and $d + Au$ systems at $\sqrt{s_{NN}} = 200$ GeV. Studying these three collision systems would allow us to develop an understanding of the role of the system size in the dynamics of the

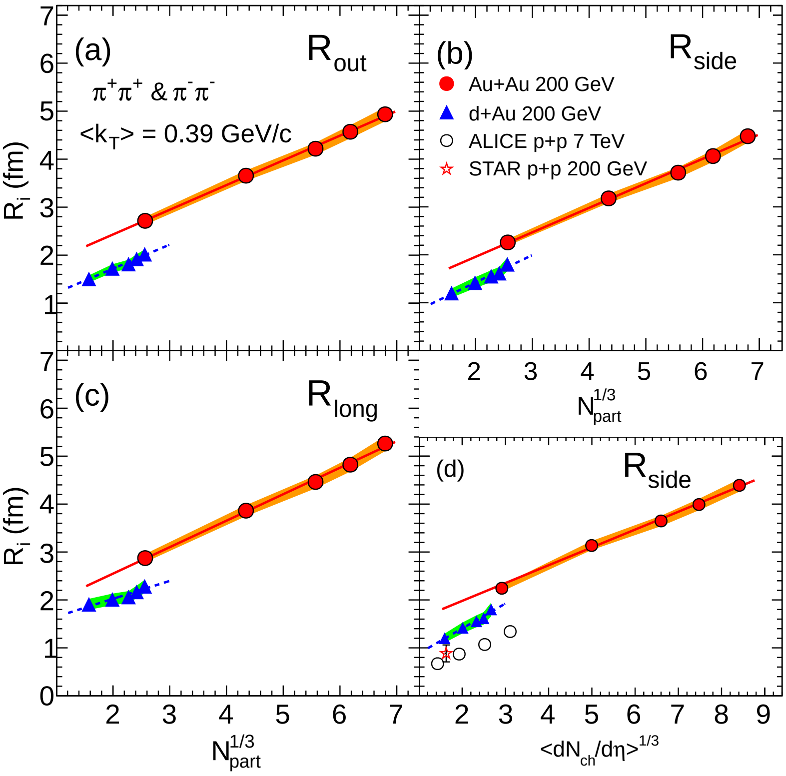

Figure 5.5.: Comparison of the $N_{part}^{1/3}$ and $dN/d\eta^{1/3}$ dependence of $d + Au$ and $Au + Au$ at $\sqrt{s_{NN}} = 200$ GeV.

system. One expectation, for instance, is that a smaller system will have a comparably smaller expansion rate. The $d + Au$ most central collisions are comparable to peripheral $Au + Au$ collisions while the $Cu + Cu$ most central events are comparable, with regard to the number of participants, to the mid-central $Au + Au$ collisions. The expectation therefore is that one will see a smooth scaling with the system size. In addition, been able to compare for the different collision systems at the same energy, and using the same detector, reduces any systematics that might arise from a collision energy dependence or detector-specific anomalies. There are several questions of interest: (1) Do we find the same trends duplicated across different sized systems? (2) What is the origin of any final system size dependence on m_T for different systems? (3) How much of an influence does the system size play in the expansion dynamics?

$Cu + Cu$ **versus** $Au + Au$

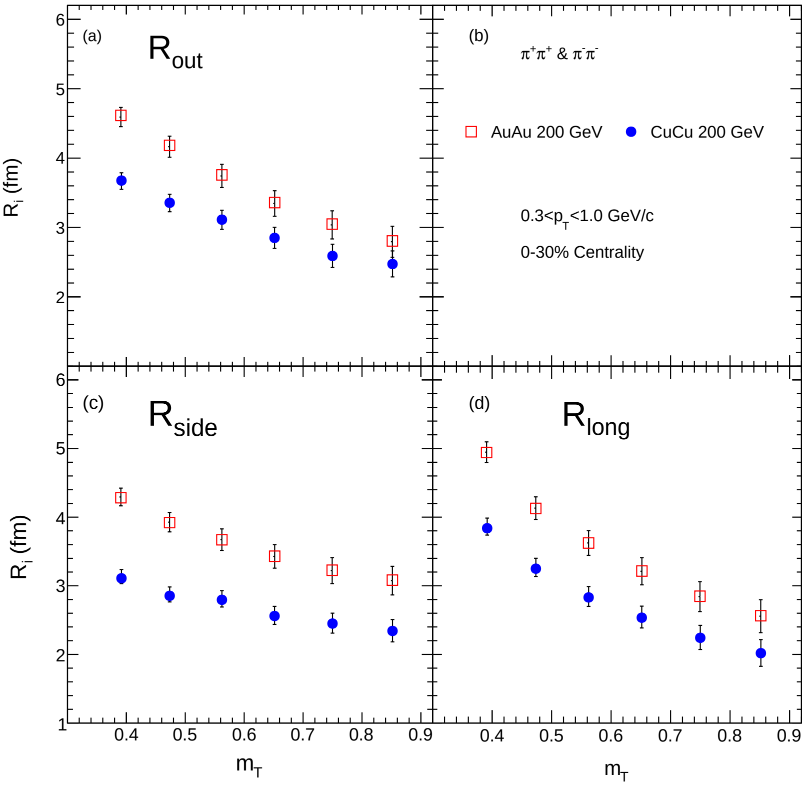

Figure 5.6.: HBT radii dependence in m_T for $Cu + Cu$ and $Au + Au$ systems at $\sqrt{s_{NN}}$ = 200 GeV and 0–30% in centrality.

Figure 5.6 shows the m_T dependence of $Cu + Cu$ and $Au + Au$ systems at $\sqrt{s_{NN}}$ = 200 GeV, taken for the most central 0–30% events (N_{part}= 75.12 and 243.16 for $Cu + Cu$ and $Au + Au$ respectively). Both systems show a decrease of R_{out}, R_{side}, and R_{long} with m_T but with the $Cu + Cu$ system showing a much smaller size. This can also be seen in the freeze-out volume dependence on m_T as well as the R_{out}/R_{side} ratio for the two systems as shown in Figures 5.7 and 5.8 respectively. As previously discussed, R_{side} carries information about the transverse geometric size while R_{out} encodes information about both the transverse size and the emission duration. The R_{out}/R_{side} ratio has therefore been widely used as a proxy measure of $\Delta\tau$ [22, 1, 14]. $Cu + Cu$ is also found

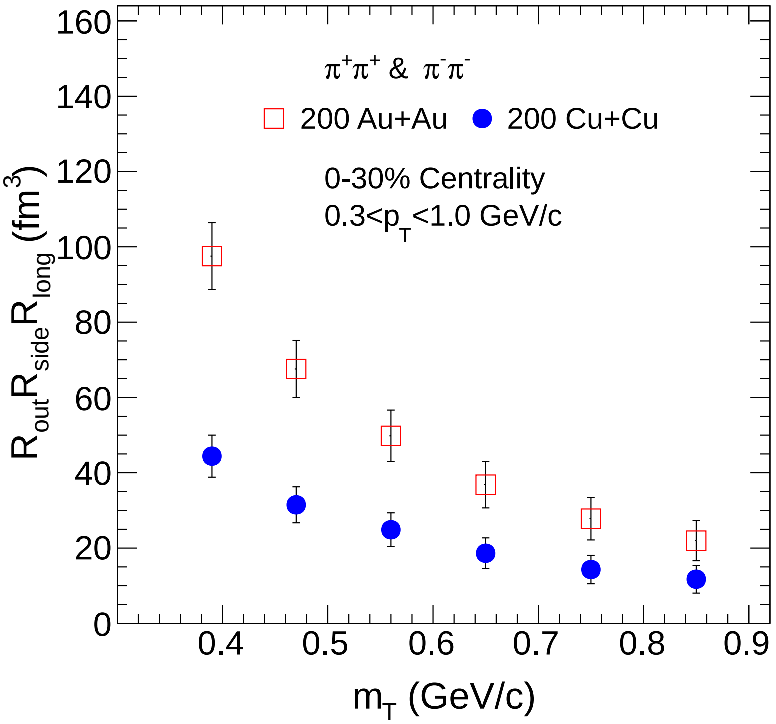

Figure 5.7.: Freeze-out volume dependence in m_T for $Cu + Cu$ and $Au + Au$ systems at $\sqrt{s_{NN}} = 200$ GeV and 0–30% centrality.

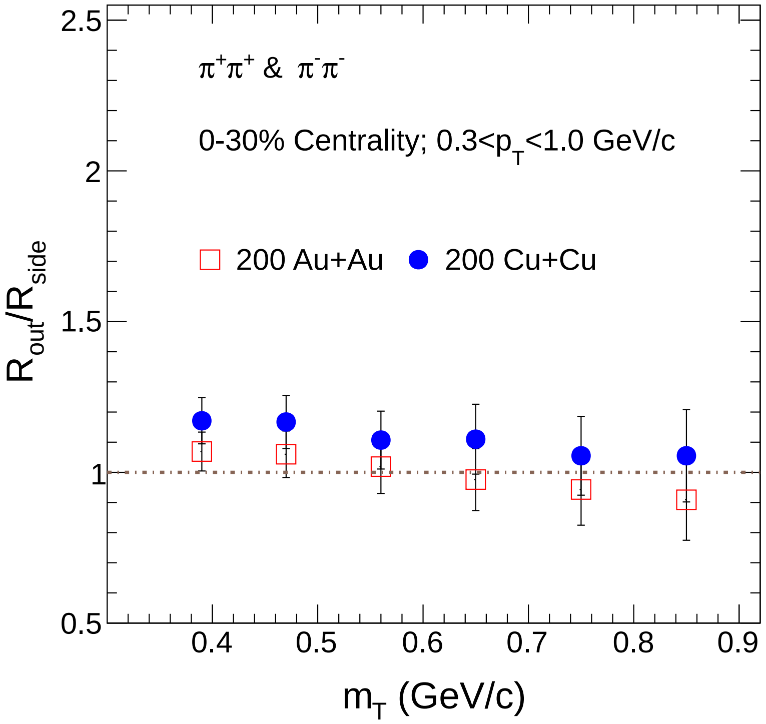

Figure 5.8.: R_{out}/R_{side} ratio for $Cu + Cu$ and $Au + Au$ at $\sqrt{s_{NN}} = 200$ GeV and 0–30% centrality.

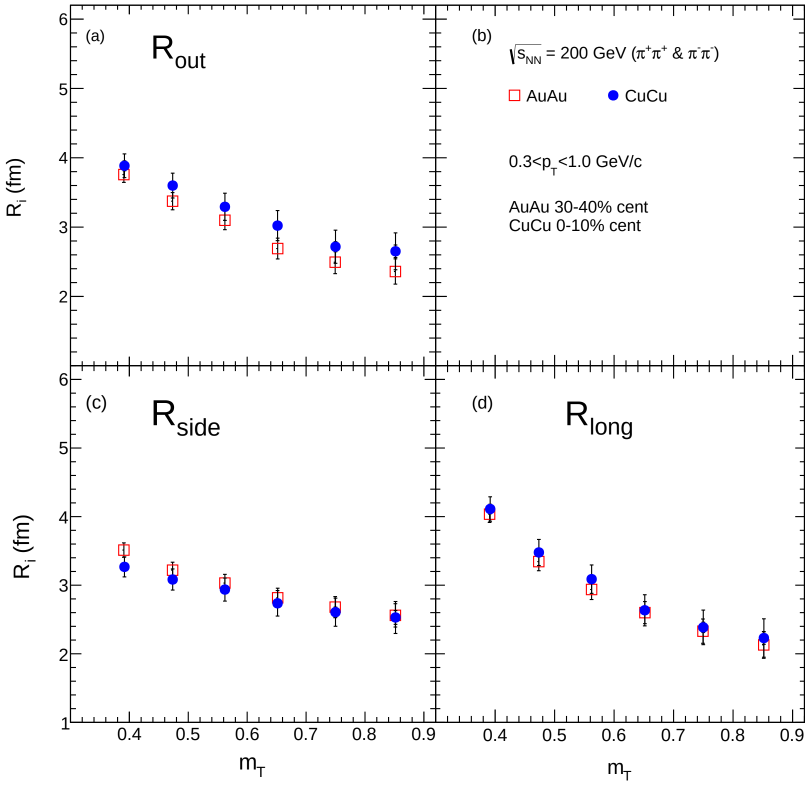

Figure 5.9.: HBT radii dependence in m_T for $Cu + Cu$ and $Au + Au$ systems at $\sqrt{s_{NN}}$ = 200 GeV and similar N_{part} values.

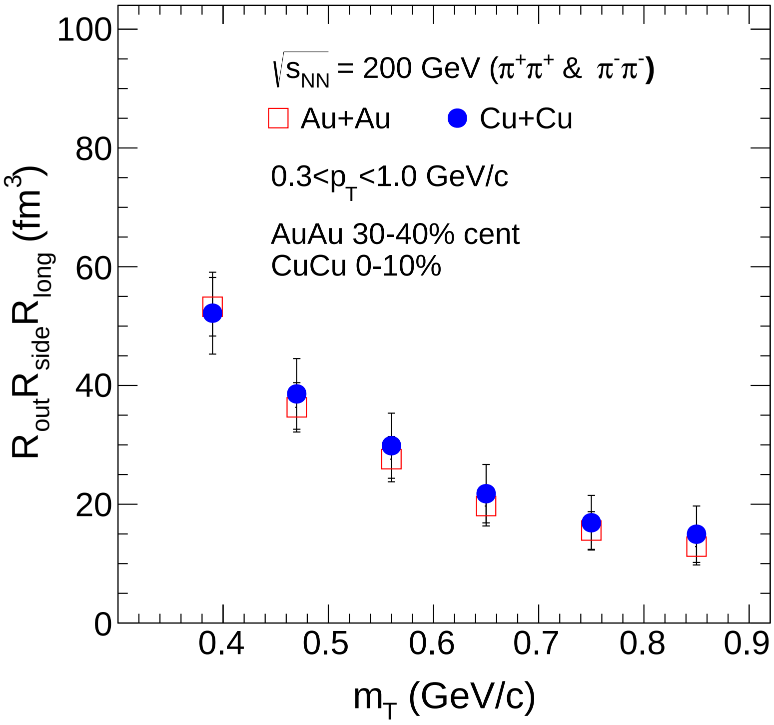

Figure 5.10.: Freeze-out volume dependence in m_T for $Cu + Cu$ and $Au + Au$ systems at $\sqrt{s_{NN}}$ = 200 GeV and similar N_{part}.

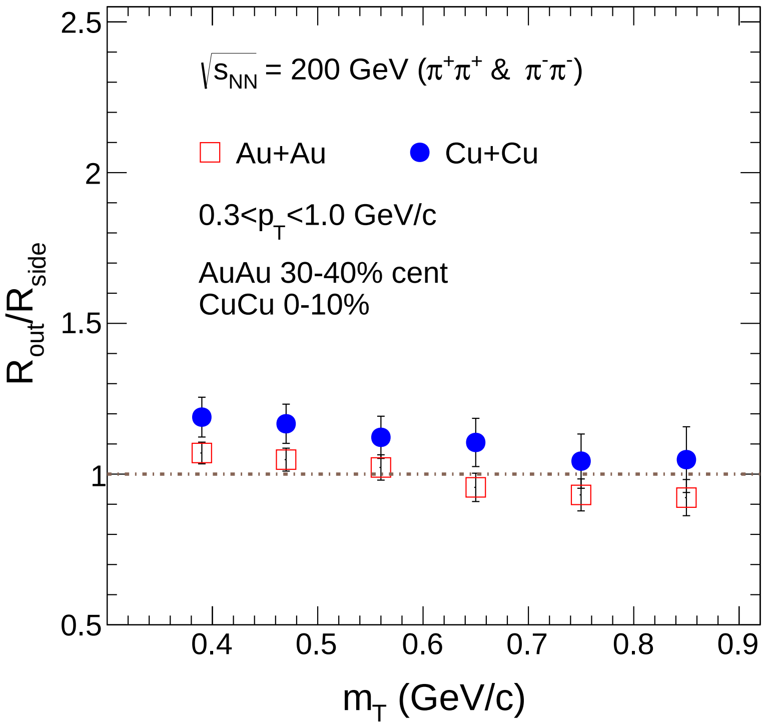

Figure 5.11.: R_{out}/R_{side} ratio for $Cu+Cu$ and $Au+Au$ at $\sqrt{s_{NN}}$ = 200 GeV and similar N_{part}.

to show a smaller freeze-out volume but a comparable very short emission duration as the $Au+Au$ system.

In Figure 5.9, is a comparison of the two systems' HBT radii at similar N_{part} values, corresponding to the most central 0–10% centrality events in $Cu+Cu$ and mid-central 30–40% centrality events in $Au+Au$. Within error, the two systems show strong similarities both in size and trend which suggests that regardless of the collision species, comparable initial geometry at collision will give rise to similar expansion dynamics and final system size at freeze-out. This again is strongly emphasised by the very good match seen in the freeze-out volume in Figure 5.10, as well as the R_{out}/R_{side} ratio in Figure 5.11 which in both systems is flat to slightly declining at the higher m_T values.

$d+Au$ versus $Au+Au$

Figure 5.12 is a plot of the HBT radii for $d+Au$ and $Au+Au$ collision systems at $\sqrt{s_{NN}}$ = 200 GeV, and at comparable N_{part} values. Both energies show a similar decline of the HBT radii with increasing m_T, with the size of the radii in $d+Au$ smaller. To get a more quantitative measure of how the two systems compare, blast-wave fits were made to R_{side} to extract the geometrical radius, R_{geom}, and to R_{long} to extract the expansion time, τ_0, using the following functions:

$$R_{side} = R_{geom}/\sqrt{(1+\beta^2(m_T/T))} \tag{5.1}$$

$$R_{long} = \tau_0\sqrt{(T/m_T)[(K_2(m_T/T))/(K_1(m_T/T))]} \tag{5.2}$$

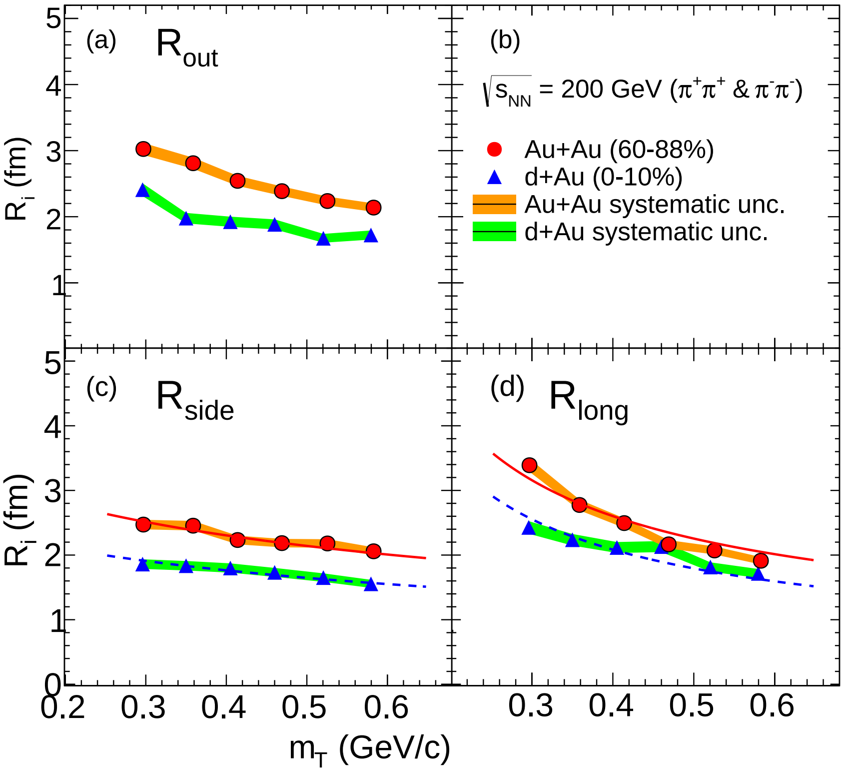

Figure 5.12.: m_T dependence of HBT parameters from $Au + Au$ (60–88% centrality) and $d + Au$ (0–10% centrality) at $\sqrt{s_{NN}} = 200$ GeV, obtained at comparable N_{part}values. Solid and dashed lines are blast-wave fits to the data.

where β is the expansion velocity, T is the freeze-out temperature, and K_1 and K_2 are modified Bessel functions. T and β were obtained from blast-wave fits to the p_T spectra for identified hadrons [108]. These input values are summarized in table 5.1. Table 5.2 shows the extracted values for R_{geom} and τ_0. These values quantitatively show that $d+Au$ has a smaller transverse freeze-out size as well as a shorter system expansion time as compared to $Au+Au$.

	$d+Au$	$Au+Au$
T (GeV)	0.118 ± 0.02	0.123 ± 0.02
β (c)	0.42 ± 0.03	0.38 ± 0.08

Table 5.1.: Temperature (T) and expansion velocity (β) input parameters for blast-wave fits to figure 5.12.

	$d+Au$	$Au+Au$
τ_0 (fm/c)	3.2 ± 0.04 ± 0.4 (syst)	3.8 ± 0.04 ± 0.3 (syst)
χ^2/ndf	26/5	24/5
R_{geom} (fm)	2.2 ± 0.03 ± 0.2 (syst)	2.8 ± 0.03 ± 0.2 (syst)
χ^2/ndf	6/5	4/5

Table 5.2.: R_{geom} and τ_0 extracted values for $d+Au$ and $Au+Au$ at $\sqrt{s_{NN}} = 200$ GeV from blast-wave fits to Figure 5.12.

In Figure 5.13, the R_{out}/R_{side} ratio (panel (a)) and the freeze-out volume (panel (b)) are calculated at the same N_{part} value as in Figure 5.12. Just as in Figures 5.8 and 5.11, the freeze-out volume is obtained as the product $R_{side} \times R_{out} \times R_{long}$. In panel (a), we find that the R_{out}/R_{side} ratio displays the same dependence in m_T as found with the $Au+Au$ and $Cu+Cu$ systems at the same beam collision energy, *i.e.,* a flat dependence at low m_T values that tapers to a gentle decrease at higher m_T values. A comparison of the freeze-out volume of the two systems as in panel (b) shows that $Au+Au$ has a much larger system size as also seen with the HBT radii. Despite this, the fall-off of the freeze-out volume with m_T is the same in both $d+Au$ and $Au+Au$ as is emphasised by the ratio in panel (c). The obvious similarities in patterns between the $d+Au$ and $Au+Au$ systems is a strong indication that the expansion dynamics of the $d+Au$ system are driven by the same final state-rescattering effects that are well understood for the bigger $A+A$ systems [85, 22, 23, 1].

The initial transverse size, $\overline{R}$, has previously been shown to be proportional to the expansion time, τ [102, 83]. Since the final system size as measured using HBT is as a result of contributions from the initial size, the system expansion, and the effects of space-momentum correlations, it is expected that the final transverse size should scale as a function of $\overline{R}$. Figure 5.14 explores this theme by looking at the scaling of (a) R_{side} with respect to $\overline{R}$ for $Pb+Pb$, $Au+Au$, and $d+Au$ collision systems and (b) R_{inv} scaling with $\overline{R}$ for $Pb+Pb$ and $p+Pb$. Note that the dashed lines are linear fits to the data. In all systems, it is found that there is a linear scaling of the final size with $\overline{R}$. Similar scaling patterns with $\overline{R}$ for collective anistropic flow have also been reported in other studies [84, 83]. The $d+Au$ and $Au+Au$ systems at RHIC energies and the $p+Pb$ and $Pb+Pb$ systems at LHC energies were observed to have comparable slopes, suggesting similar expansion rates. The difference in slopes between the RHIC results and LHC

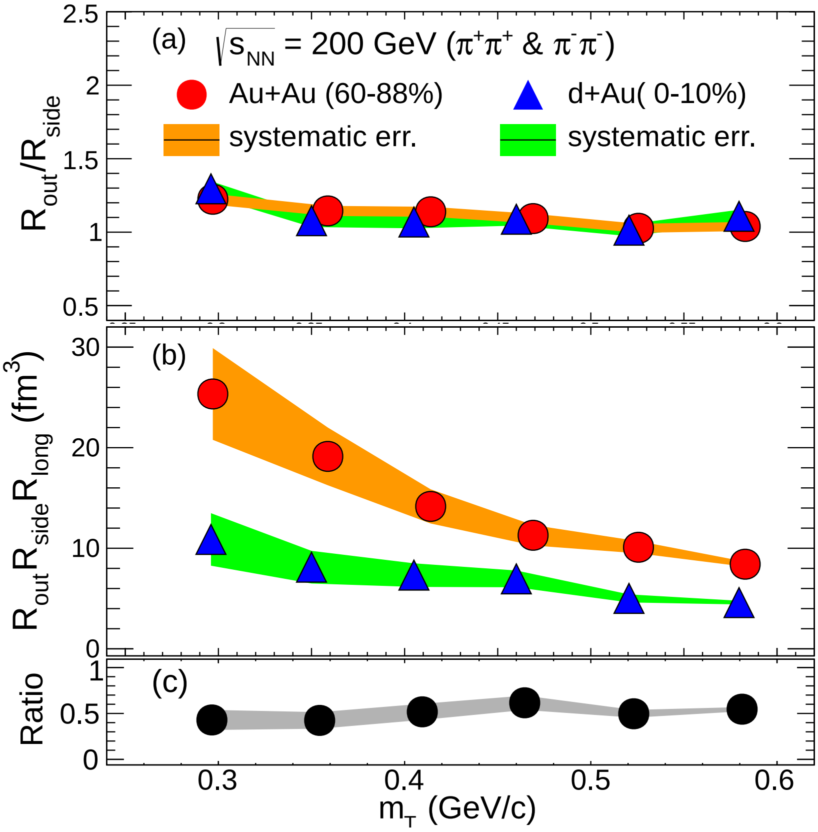

Figure 5.13.: A comparison of the R_{out}/R_{side} ratio as well as the freeze-out volume ($R_{out} \times R_{side} \times R_{long}$) for $Au + Au$ and $d + Au$ at $\sqrt{s_{NN}} = 200$ GeV.

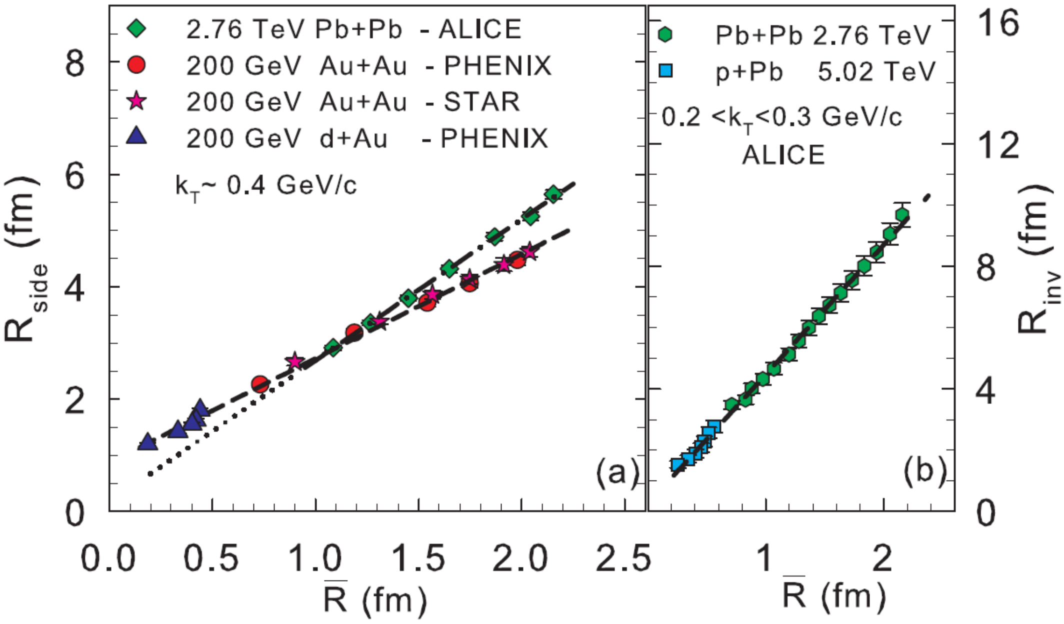

Figure 5.14.: R_{side} scaling with $\overline{R}$ for $Pb+Pb$, $Au+Au$, and $d+Au$ collision systems. (b) R_{inv} scaling with $\overline{R}$ for $Pb+Pb$ and $p+p$ collision systems at LHC beam energies. The ALICE and STAR data were obtained from Refs. [1][15] and [5] respectively.

results can be attributed to the difference in expansion rates at the higher LHC energies. The observed similarities between the $d(p)+A$ and $A+A$ systems is a reaffirmation of the previous conclusion that hydrodynamic-driven final-state effects play a key role in the evolution of small asymmetric systems.

5.3. Scaling Patterns

In this section, I present results for three different beam energies – $\sqrt{s_{NN}}$ = 39, 62, and 200 GeV – as well as three collision systems: $Cu+Cu$, $Au+Au$, and $Pb+Pb$. Using these results, I will discuss various scaling properties observed to be universal across different energies and collision systems. As was shown in Fig. 5.14, the final transverse size (R_{side}) scales with $\overline{R}$ at a fixed m_T . This argument can be extended to all the HBT radii at each m_T bin since the three radii have the system lifetime, τ, in common and τ is proportional to the initial size. Similarly, since the final size is also related to the space-momentum correlations, scaling of the HBT radii with m_T would also be expected.

5.3.1. $N_{part}^{1/3}$ dependence

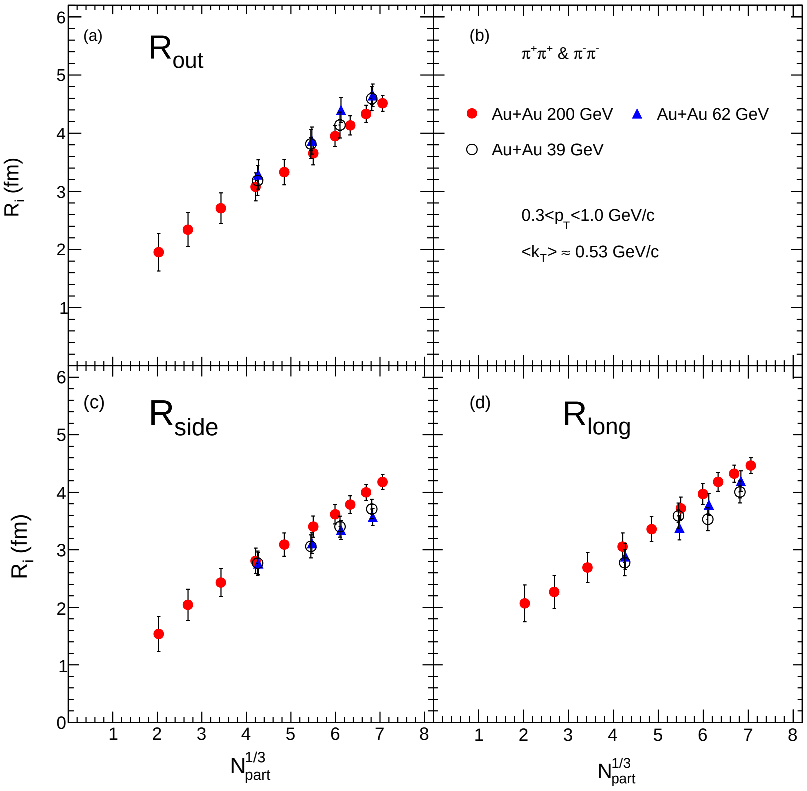

Figure 5.15.: $N_{part}^{1/3}$ dependence of R_{out}, R_{side}, and R_{long} for $Au+Au$ collisions at three beam energies of $\sqrt{s_{NN}}$ = 39, 62, and 200 GeV at $<k_T> = 0.53$ GeV/c.

Figure 5.15 shows the $N_{part}^{1/3}$ dependence of $Au+Au$ collisions at three beam energies of $\sqrt{s_{NN}}$ = 39, 62, and 200 GeV. All three energies show an approximate linear dependence with $N_{part}^{1/3}$.

To understand these results, it is instructive to look at how the freeze-out density varies with changes in centrality and collision energy. The pion free path at freeze-out, λ_f^π, is defined as:

$$\lambda_f^\pi = \frac{1}{\rho_f \sigma} = \frac{V_f}{N\sigma} \tag{5.3}$$

Where ρ_f is the density at freeze-out, σ is the pion total cross section, V_f is the freeze-out volume, and N is the number of particles within the freeze-out volume [12]. At a fixed energy, studies have shown that λ_f is constant at about 1 fm. This suggests that the freeze-out density is also a constant. Since the multiplicity scales with the number of participants [29], it is expected that the HBT radii will also increase linearly with the same number of participants, which is what Figure 5.15 demonstrates. This findings are consistent with previous results for different collision systems [12, 10, 22].

Across the three energies, the results do not show a strong beam energy dependence. At RHIC energies, the chemical composition of the fireball does not vary much since it is meson-dominated, as compared to the lower AGS/SPS energies where we find a much bigger baryon fraction [12, 85]. For this reason, λ_f will largely remain constant at RHIC energies and the freeze-out densities will reach asymptotic values. In addition, we see very little increase in the number of participants at each centrality for the $Au + Au$ collisions going from 39 to 200 GeV (at 0–10% centrality, $N_{part} = 316.6$ for 39 GeV and 325.8 for 200 GeV). These two factors could explain the lack of a strong beam energy dependence in the $Au + Au$ collisions at the three beam energies shown in Figure 5.15.

5.3.2. m_T dependence

Figure 5.16 shows the m_T dependence of the $Au + Au$ system at 39, 62, and 200 GeV for the most central 0–30% centrality events. All three energies show the previously observed decrease of HBT radii with an increase in m_T [1, 24, 35].

Collective effects or flow introduce space-momentum correlations to the system. Due to these space-momentum correlations, high k_T particles tend to be emitted more from the surface of the source. Since HBT radii measure regions of homogeneity (region where particles are emitted with the same average k_T), the HBT radii, both in the transverse and longitudinal directions, will be seen to decrease with k_T as pairs with large k_T are emitted from smaller regions of homogeneity [93, 96]. The results also show a much stronger fall-off with k_T of the longitudinal HBT radius as compared to the transverse radii. These can be attributed to the expected boost-invariant expansion in the longitudinal direction, which in turn would make the longitudinal geometric size much larger than the size measured in HBT.

Across the three energies, no strong beam energy dependence was observed, within error, either in magnitude or in trends, suggesting that the dynamics of expansion do not vary much within the three energies compared here.

The R_{out}/R_{side} ratio for $Au + Au$ 39, 62, and 200 GeV

Figure 5.17 shows the R_{out}/R_{side} dependence on m_T for $Au + Au$ collisions at 39, 62, and 200 GeV. The ratios for 39 and 62 GeV are comparable to within error while 200 GeV is systematically lower across the whole m_T range studied. All three energies show a gentle decrease of the R_{out}/R_{side} ratio with an increase in m_T.

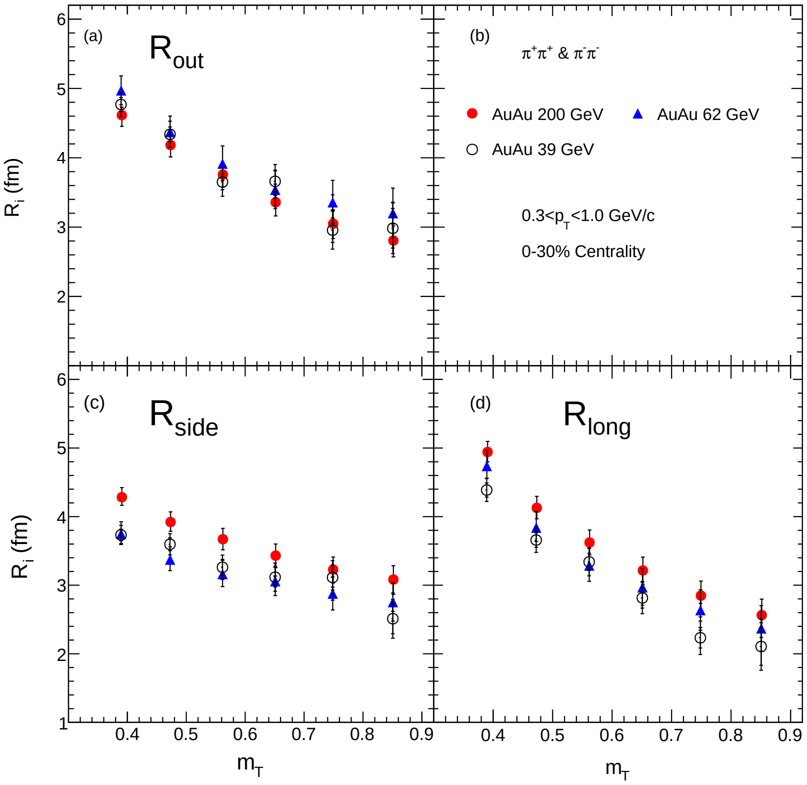

Figure 5.16.: Dependence of HBT radii on m_T for $Au+Au$ $\sqrt{s_{NN}}$ = 39, 62, and 200 GeV for the most central 0–30% centrality.

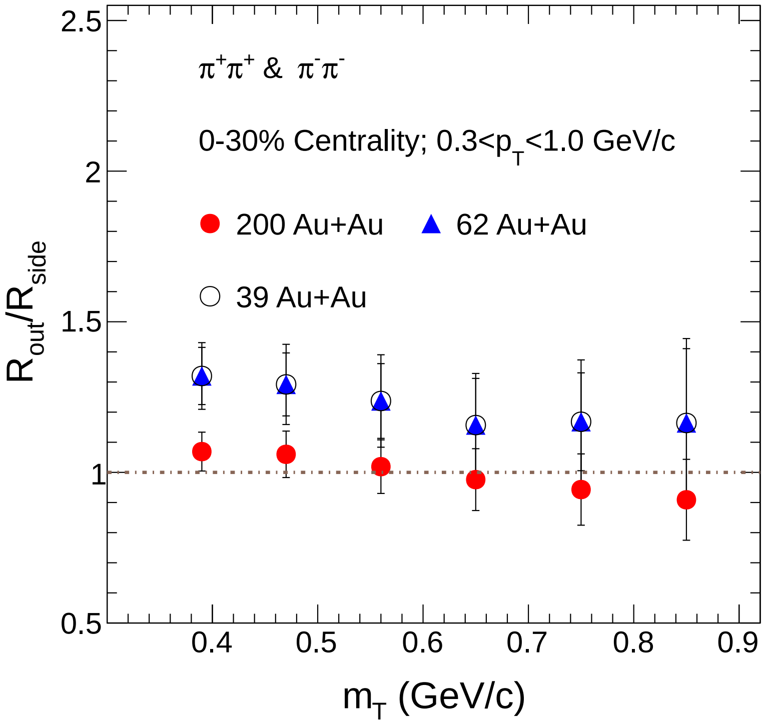

Figure 5.17.: R_{out}/R_{side} dependence on m_T for $Au+Au$ $\sqrt{s_{NN}}$ = 39, 62, and 200 GeV for 0–30% centrality.

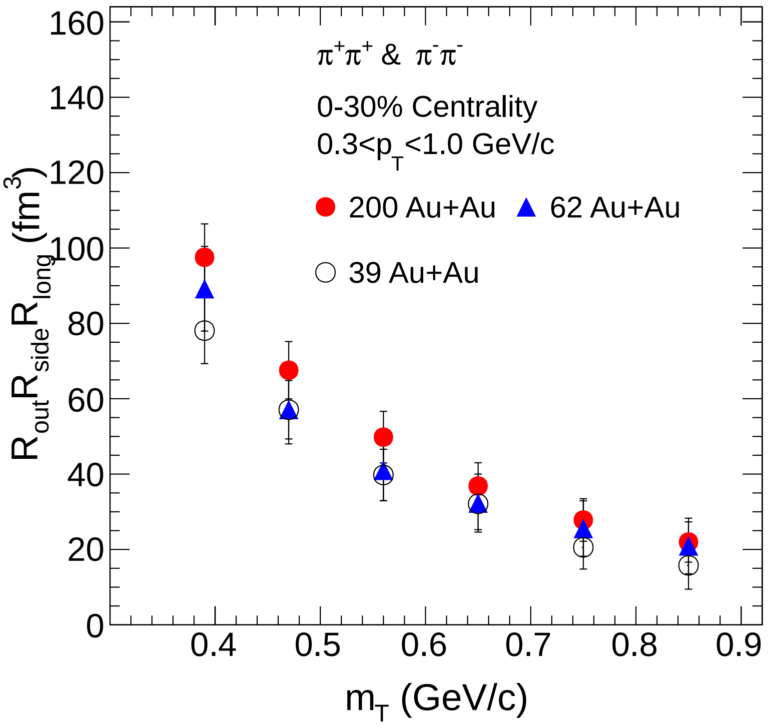

Figure 5.18.: Freeze-out volume for 0–30% central collisions in $Au + Au$ at $\sqrt{s_{NN}}$ = 39, 62, and 200 GeV.

V_f for $Au + Au$ collisions: 39, 62, and 200 GeV

The freeze-out volume, V_f, is estimated as the product of R_{out}, R_{side}, and R_{long}. As expected, V_f shows a decrease with m_T in all three energies to within systematic error. No large variations in the magnitude were observed between 39, 62, and 200 GeV. This observation again can be tied to the little increase in the number of participants going across the three energies as the freeze-out densities remain constant.

5.3.3. $\sqrt{m_T}$ dependence

Figure 5.19 is a comparison of PHENIX and STAR results for HBT radii dependence on $1/\sqrt{m_T}$ at two centrality selections, and for 39, 62, and 200 GeV $Au + Au$ collisions. The results show an almost linear dependence on $1/\sqrt{m_T}$ for R_{out}, R_{side}, and R_{long}. A very good match is also found between the PHENIX and STAR results. Combining the results from the two experiments serves two primary functions: (1) It allows for an extended m_T coverage by leveraging the PHENIX data. STAR results terminate at m_T = 0.52 GeV/c but combining the two sets of data allows the coverage to be extended to 1.0 GeV/c. (2) The two detectors have different systematics, and therefore a good match in measurements made for the same parameters builds confidence that the relevant experiment-specific systematics have been sufficiently addressed.

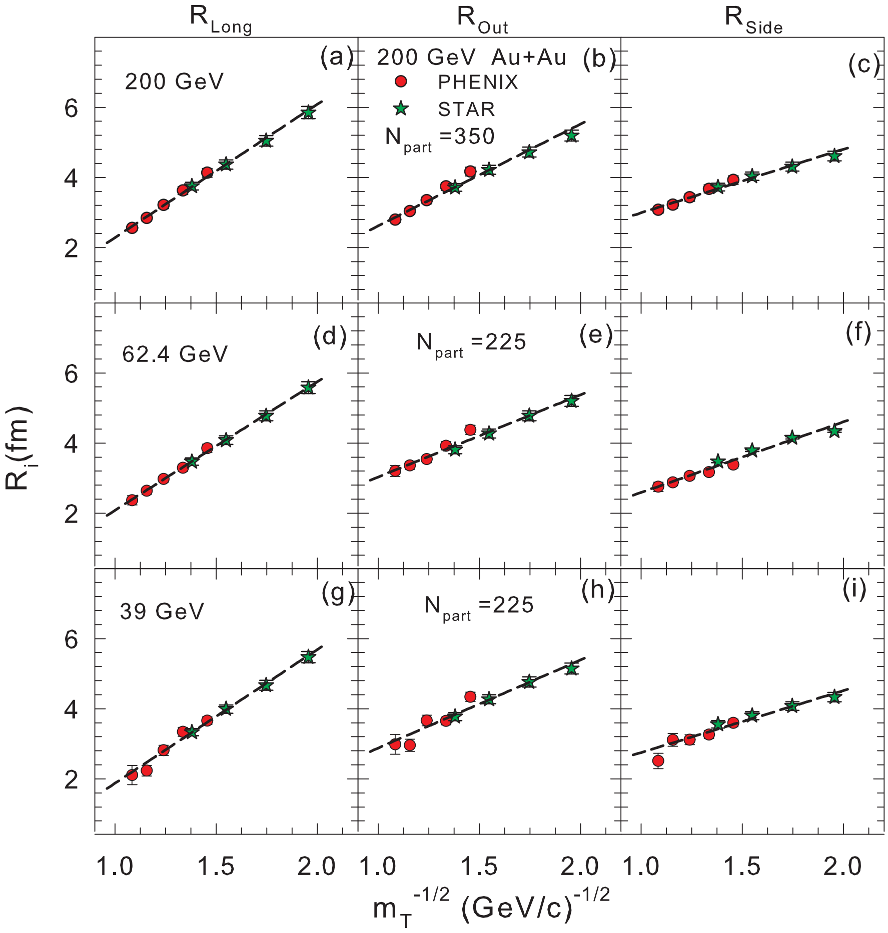

Figure 5.19.: A comparison of PHENIX and STAR HBT radii dependence on $1/\sqrt{m_T}$ $(GeV/c)^{1/2}$ for $Au + Au$ collisions at $\sqrt{s_{NN}}$ = 39,62, and 200 GeV, and for two N_{part} values of 350 and 225.

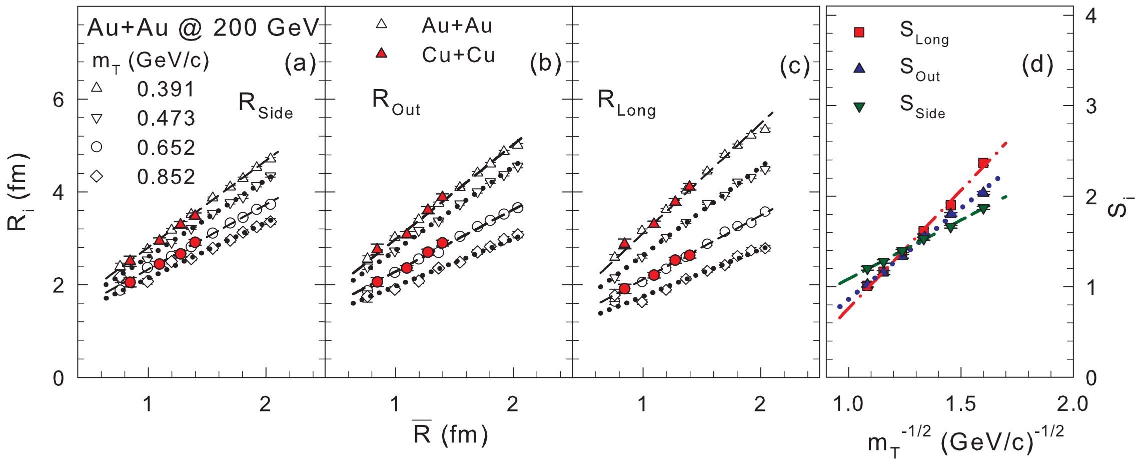

Figure 5.20.: Panels (a)–(c) show HBT radii $\overline{R}$ dependence for four m_T cuts at $\sqrt{s_{NN}} =$ 200 GeV in $Au+Au$ and $Cu+Cu$ collision systems. The centrality selection in $Cu + Cu$ corresponds to 0–10%, 10–20%, 20–30%, and 30–40%. Those in $Au + Au$ are 0–5%, 5–10%, 10–15%, 15–20%, 20–30%, 30–40%, 40–50%, 50–60%, and 60–70%. The dashed and dotted curves are linear fits to the data, and the slopes extracted from these fits, S_i, are plotted in panel (d) as a function of $1/\sqrt{m_T}$ $(GeV/c)^{1/2}$ for R_{side}, R_{out}, and R_{long}.

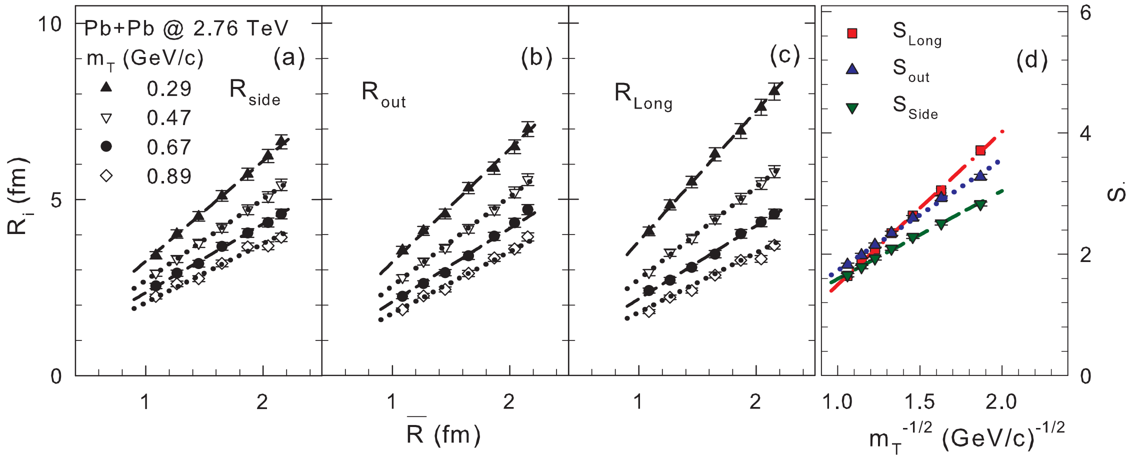

Figure 5.21.: Panels (a)–(c) show HBT radii $\overline{R}$ dependence for four m_T cuts at $\sqrt{s_{NN}} =$ 2.76 TeV in the $Pb+Pb$ collision system for measurements done at the LHC [77]. Similar to Figure 5.20, the dashed and dotted curves are linear fits to the data, and the slopes extracted from these fits, S_i, are plotted in panel (d) as a function of $1/\sqrt{m_T}$ $(GeV/c)^{1/2}$ for R_{side}, R_{out}, and R_{long}.

5.3.4. $\overline{R}$ dependence

In Figure 5.20, a comparison of $Cu + Cu$ and $Au + Au$ for R_{out}, R_{side}, and R_{long} is made for a dependence on $\overline{R}$ (panels a, b, and c). Both systems show similar scaling patterns with $\overline{R}$. Their magnitudes are also similar at the same m_T bins and $\overline{R}$. Slopes of the scaling curves are seen to decrease with an increase in m_T which is an indication of the influence of space-momentum correlations resulting from collective expansion effects. Similar scaling patterns are also seen in Figure 5.21 (a, b, c) for LHC data at 2.76 TeV which show a larger HBT size. The increase in size from RHIC energies to LHC energies can be attributed to an increase in τ and $< c_s >$ rather than an increase in the initial geometry, going from $Au+Au$ to $Pb+Pb$ (the change in $\overline{R}$ between $Au+Au$ and $Pb+Pb$ is only 5%).

In Figure 5.20 (d) and 5.21 (d), plots for the slopes extracted from the linear fits to Figure 5.20 (a, b, and c) and Figure 5.21 (a,b, and c) respectively are shown. These slopes are found to scale with $1/\sqrt{m_T}$ in both systems. The dependence on $1/\sqrt{m_T}$ also reveals that the space momentum correlation do not act uniformly on all three HBT radii but are strongest in R_{long} and weakest in R_{side}. Equally important is the observation that the complete set of measurements for dependence in centrality and m_T at different energies can be scaled into one curve.

5.4. Search for CEP and/or Onset of Deconfinement

Central to understanding the QCD phase diagram is identifying the location of the phase boundaries, as well as the QCD Critical End Point (CEP) in the temperature (T) versus baryon chemical potential (μ_B) plane. As previously discussed in the introduction, close to the CEP, it is expected that significant changes in the dynamic as well as static properties of the medium will be evident. One such change in the dynamic properties is the slowing down of the system expansion such that there is a drastic reduction in the expansion speed, $<c_s>$ (i.e., $<c_s>\rightarrow 0$). An emitting system that is thus slowed down will be able to emit for longer and will therefore show an increase in $\Delta\tau$. Since R_{out} encodes information about the emission of the system, this would be reflected in an R_{out} that is larger than R_{side}. To identify such changes, it is imperative that we are able to access a wide range of reaction trajectories on the $T : \mu_B$ plane. This is only possible through a beam energy scan.

As mentioned before, the final size measured at freeze-out consists of contributions from the initial system size, the increase in size due to expansion, and the reduction in size attributed to the effects of space-momentum correlations. The need to account for the initial size when studying the expansion dynamics of the system in HBT can clearly be seen in Figures 5.22, 5.23, and 5.24. Here, plots for the R_{out}/R_{side} ratio dependence on $\sqrt{s_{NN}}$, for the range 7.7 GeV to 2.76 TeV, and the same ratio after subtracting the initial size, $\sqrt{2}\,\overline{R}$ $((R_{out}\text{-}\sqrt{2}\,\overline{R})/(R_{side}\text{-}\sqrt{2}\,\overline{R}))$ are shown for 0–5% centrality and for three m_T selections. Non-monotonic behavior is evident over a small $\sqrt{s_{NN}}$ range after removal of the initial size. These effects would otherwise be suppressed in the R_{out}/R_{side} ratios due to the contribution from the initial size. The non-monotonic behavior is also strongest at low m_T values since at those values, there is a smaller contribution of space-momentum correlations.

To investigate further the signs of non-monotonic behavior observed in Figures 5.22, 5.23 and 5.24, the quantities R^2_{out} - R^2_{side} are plotted for the same dependence on $\sqrt{s_{NN}}$

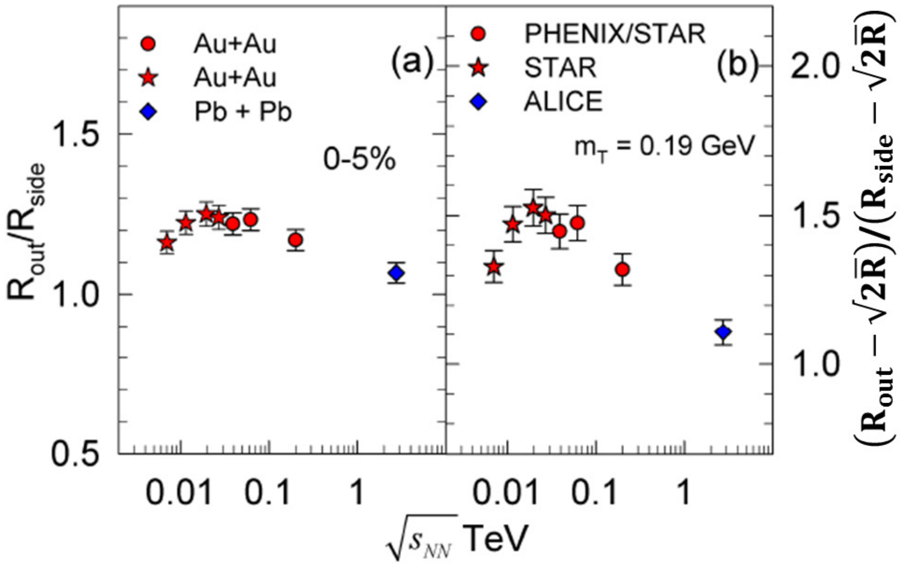

Figure 5.22.: (a) R_{out}/R_{side} and (b) $(R_{out}$ - $\sqrt{2}\,\overline{R})/(R_{side}$ - $\sqrt{2}\,\overline{R})$ dependence on $\sqrt{s_{NN}}$ for 0–5% centrality and m_T = 0.19 GeV. R_{out}/R_{side} ($R_{out}/R_{side} \propto \Delta\tau$) includes the effects of the initial size while in $(R_{out}$ - $\sqrt{2}\,\overline{R})/(R_{side}$ - $\sqrt{2}\,\overline{R})$, this contribution is accounted for by subtracting the initial size, estimated to be $\sqrt{2}\,\overline{R}$ at very central collisions. The combined PHENIX and STAR data points are extracted from fits to the m_T dependence in Figure 5.19.

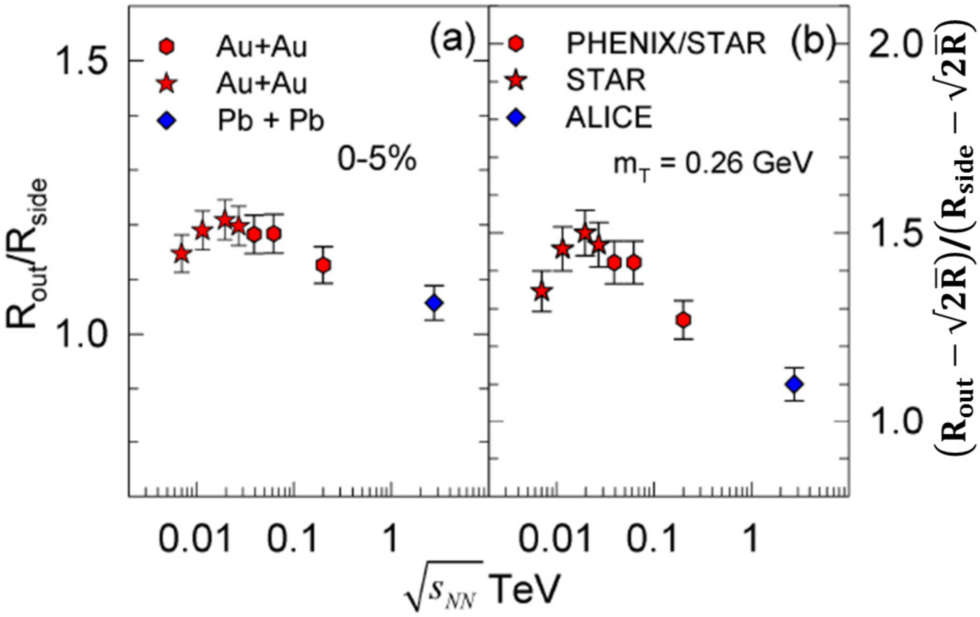

Figure 5.23.: (a) R_{out}/R_{side} and (b) $(R_{out}$ - $\sqrt{2}\,\overline{R})/(R_{side}$ - $\sqrt{2}\,\overline{R})$ dependence on $\sqrt{s_{NN}}$ for 0–5% centrality and m_T = 0.26 GeV.

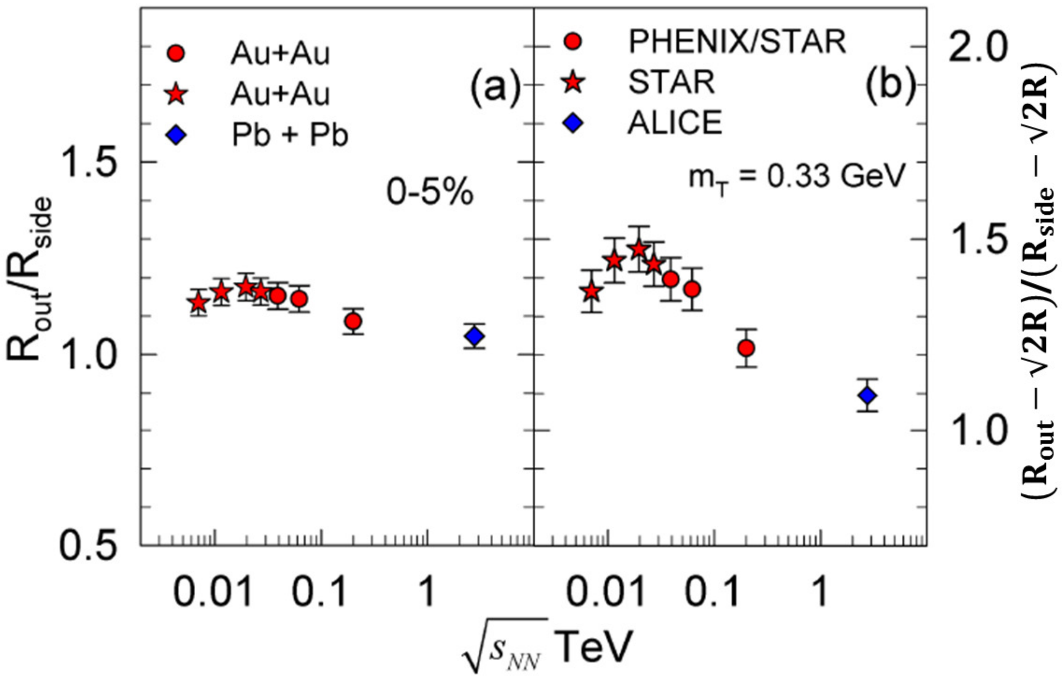

Figure 5.24.: (a) R_{out}/R_{side} and (b) (R_{out} - $\sqrt{2}\,\overline{R}$)/(R_{side} - $\sqrt{2}\,\overline{R}$) dependence on $\sqrt{s_{NN}}$ for 0–5% centrality and m_T = 0.33 GeV.

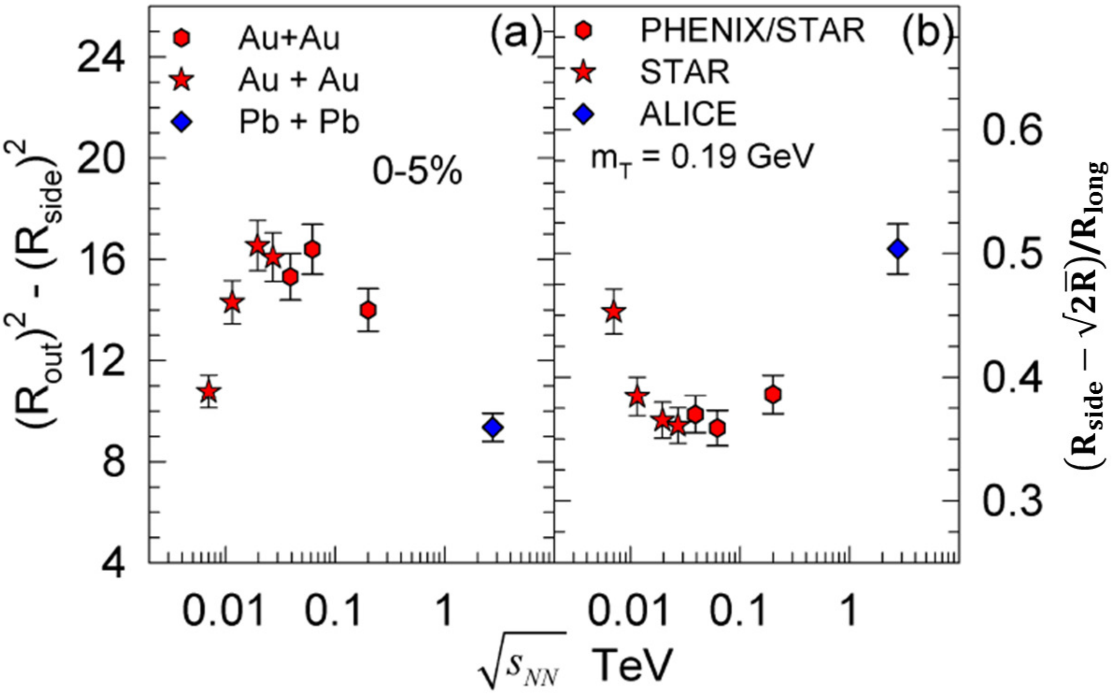

Figure 5.25.: (a) R_{out}^2 - R_{side}^2 and (b) (R_{side} - $\sqrt{2}\,\overline{R}$)/R_{long} dependence on $\sqrt{s_{NN}}$ for 0–5% centrality and $m_T = 0.19$ GeV. R_{out}^2 - R_{side}^2 is proportional to $\Delta\tau^2$ while (R_{side} - $\sqrt{2}\,\overline{R}$)/R_{long} is proportional to $< c_s >$. The combined PHENIX and STAR data points are extracted from fits to the m_T dependence in Figure 5.19.

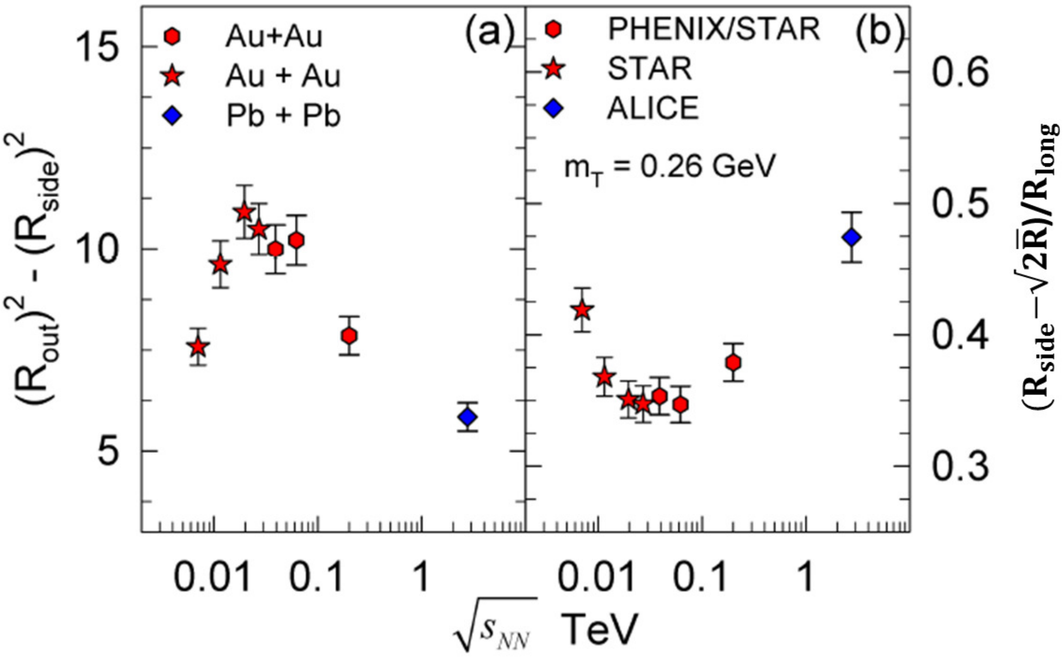

Figure 5.26.: (a) R^2_{out} - R^2_{side} and (b) $(R_{side}$ - $\sqrt{2}\,\overline{R})/R_{long}$ dependence on $\sqrt{s_{NN}}$ for 0–5% centrality and $m_T = 0.26$ GeV.

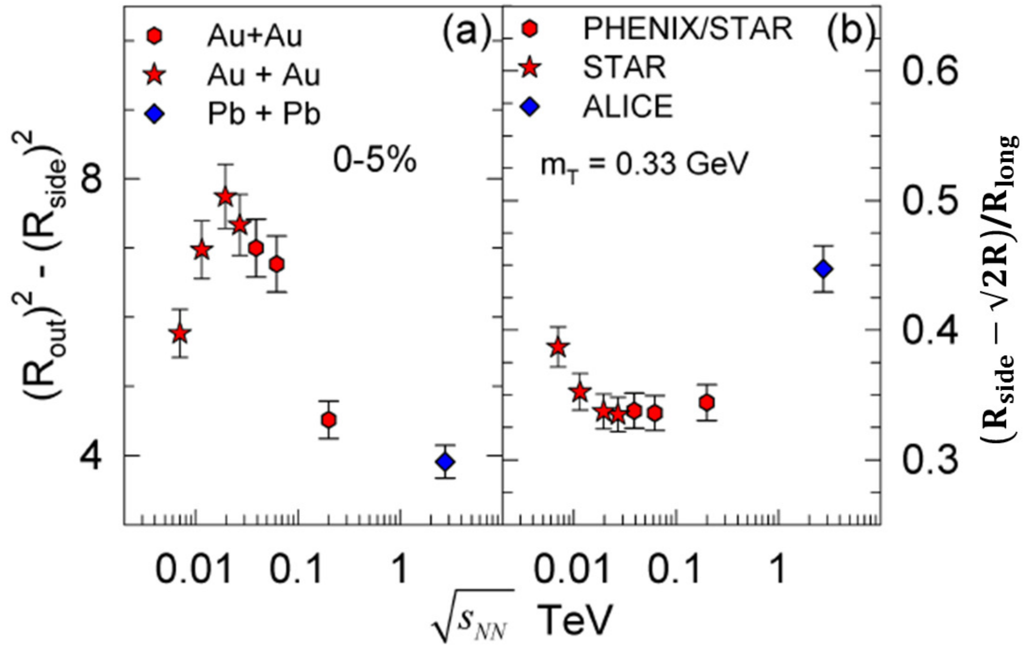

Figure 5.27.: (a) R^2_{out} - R^2_{side} and (b) $(R_{side}$ - $\sqrt{2}\,\overline{R})/R_{long}$ dependence on $\sqrt{s_{NN}}$ for 0–5% centrality and $m_T = 0.33$ GeV.

(the range 7.7 GeV to 2.76 TeV). R^2_{out} - R^2_{side} here is used as a proxy for $\Delta\tau^2$ but with greater sensitivity than the R_{out}/R_{side} ratio. $(R_{side}$ - $\sqrt{2}\,\overline{R})/R_{long}$ is proportional to $< c_s >$. Figures 5.25, 5.26, and 5.27 show this dependence for 0–5% centrality events and three m_T selections. R^2_{out} - R^2_{side} shows a maximum at a narrow $\sqrt{s_{NN}}$ range with a complimentary minimum in $(R_{side}$ - $\sqrt{2}\,\overline{R})/R_{long}$ for the same range in $\sqrt{s_{NN}}$. This non-monotonic behavior suggests that the beam energies studied might be sampling from reaction trajectories in the vicinity of the CEP. Furthermore, the strength of the non-monotonic behavior is observed to increase at lower m_T values due to the suppression of space-momentum correlations contributions at these m_T values. Additional energy scans as proposed for the RHIC Beam Energy Scan Phase II (BES II), with emphasis on this narrow energy region, might help pin-point the exact location of the CEP.

6. Conclusion

Two-pion interferometry measurements using the Hanbury-Brown and Twiss method, applied to different collision systems and beam energies, are presented in this thesis. These measurements are important in extracting the space-time extent of the pion emission sources created in heavy-ion collisions at RHIC. In this work, HBT measurements were made with two objectives in mind: (1) Develop an understanding of the contribution of hydrodynamic-driven final-state effects to the expansion dynamics of small asymmetric systems and (2) look for universal scaling patterns in dependencies of HBT measurements, and use these measurements to search for signatures of the CEP and/or onset of deconfinement.

A study of the N$_{part}$ dependence of $A+A$ collisions, comparing $Cu+Cu$ and $Au+Au$ systems, revealed that R_{out}, R_{side}, and R_{long} show a linear dependence with N_{part}. This scaling property is attributed to the increase in multiplicity with increasing N_{part}. The $Cu+Cu$ and $Au+Au$ systems were also found to to have both the same trend and same magnitude at similar N_{part} for all HBT radii. There was no strong beam energy dependence observed for the three energies of $\sqrt{s_{NN}}$ $= 39$, 62 and 200 GeV in $Au+Au$. At RHIC energies, the pion mean free path at freeze-out, λ_f^π , remains constant while the freeze-out densities reach asymptotic levels. These, and the little increase in N_{part} across energies would explain the lack of a strong energy dependence. A comparison of $d+Au$ and $Au+Au$ HBT radii for N_{part} dependence found that the two systems have the same increasing trend with an increase in N_{part}, but with a slight change in the slope for R_{long}. This difference in slope was attributed to a change in the longitudinal expansion dynamics. The difference in magnitude between the $d+Au$ and $Au+Au$ HBT radii at the same N_{part} suggests that N_{part} might not be the ideal parameter for studies of the initial geometry in small systems.

The m_T dependence of HBT parameters was also studied in this analysis. The rapid expansion of the hot and dense systems emanating from heavy-ion collisions introduces space-momentum correlations that are manifest in the final size of the pion emitting source. Studies of the m_T dependence of HBT measurements allow for a detailed investigation of the dynamics of these hot and dense systems. These analysis found that the three beam energies and three collision systems studied demonstrate a decrease in size with increasing m_T. This behavior has been reported before, and is indicative of a radially expanding system. For a static source, HBT measurements would be a true measure of the actual geometric size of the system. On the contrary, an expanding source, as previously mentioned, introduces space-momentum correlations such that the HBT measurements represent not the geometric size but the widths of a region in the source that is emitting pion pairs of the same average momentum. It was found too that as a result of the stronger longitudinal flow, R_{long} shows a stronger m_T dependence as compared to R_{side} and R_{out}. A comparison of the $A+A$ systems of $Cu+Cu$ and $Au+Au$ found that that at the same selection in N_{part}, the two systems were comparable both in magnitude and slope for their dependence in m_T. A similar comparison between $d+Au$ and $Au+Au$, and with quantitative values of the size of the system extracted using blast-wave fits to the HBT radii, found that the $d + Au$ system has both a smaller geometric transverse size (R_{geom}) as well as a shorter emission duration. Despite the smaller size, the $d + Au$ system was found to show a similar pattern to $Au+Au$ in its m_T dependence. Previously, the small $d + A$ and $p + p$ systems have been considered too small and too short-lived for significant medium effects to form. The results presented here are a strong indication that even in these small systems, the role of final state re-scattering effects in the evolution of the hot and dense medium cannot be overlooked.

A detailed comparison of the HBT radii for $Au + Au$ and $Cu + Cu$ at $\sqrt{s_{NN}} = 200$ GeV, as well as $Pb + Pb$ at $\sqrt{s_{NN}} = 2.76$ TeV (measured at LHC) found that the three collision systems show similar scaling with $\bar{R}$. The $Au + Au$ and $Cu + Cu$ systems HBT radii were found to have the same magnitude in their $\bar{R}$ dependence for the same m_T slices. In addition, the study found that the slopes extracted from linear fits to the $\bar{R}$ dependence at each m_T bin showed scaling with $1/\sqrt{m_T}$, highlighting the important role of space-momentum correlations in the final freeze-out geometry.

A primary objective of this analysis was to study the excitation functions of HBT parameters in different collision systems for non-monotonic behavior that would be suggestive of a phase transition and/or the prescence of the QCD Critica End Point (CEP). Towards this goal, an analysis of the $R^2_{out} - R^2_{side}$ and (R_{side} - $\sqrt{2}\,\overline{R}$)/R_{long} excitation functions was made. R_{out} carries information about the transverse geometric size of the system as well it emission duration. R_{side} only encodes information about the transverse geometric size. For this reason, $R^2_{out} - R^2_{side}$ is proportional to $\Delta\tau^2$. Similarly, the ratio (R_{side} - $\sqrt{2}\overline{R}$)/R_{long} is proportional to the mean expansion speed, $\langle c_s \rangle$. In the $\sqrt{s_{NN}}$ range of 7.7 GeV - 2.76 TeV and 0-5% in centrality, the study found that $R^2_{out} - R^2_{side}$ shows a maximum while (R_{side} - $\sqrt{2}\,\overline{R}$)/R_{long} shows a complimentary minimum over a small $\sqrt{s_{NN}}$ range. According to model calculations based on thermodynamics, a softening of the Equation of State (EoS) in the vicinity of a CEP or phase transition will lead to a drastic slowing down in the expansion of the system. This will in turn lead to an increase in the emission duration and a decrease in $\langle c_s \rangle$ which tends to zero. The observed non-monotonic behavior in the excitation functions of $R^2_{out} - R^2_{side}$ and (R_{side} - $\sqrt{2}\,\overline{R}$)/R_{long} points to dramatic changes happening in the system dynamics over a narrow range in beam collision energy. This could be indicative of reaction trajectories that traverse the QCD critical-end-point and/or the onset of deconfinement. It is the author's opinion that further measurements are needed over this small energy range of interest that might help pin-point the exact location of the CEP. The proposed RHIC Beam Energy Scan Phase II (BES II) might provide for such an opportunity.

Bibliography

[1] K. Aamodt et al. Two-pion Bose-Einstein correlations in central Pb-Pb collisions at $\sqrt{s_{\mathrm{NN}}} = 2.76$ TeV. *Phys.Lett.*, B696:328–337, 2011. doi: 10.1016/j.physletb.2010.12.053.

[2] K. Aamodt et al. Harmonic decomposition of two-particle angular correlations in Pb-Pb collisions at $\sqrt{s_{NN}} = 2.76$ TeV. *Phys.Lett.*, B708:249–264, 2012. doi: 10.1016/j.physletb.2012.01.060.

[3] Betty Abelev et al. Long-range angular correlations on the near and away side in *p*-Pb collisions at $\sqrt{s_{NN}} = 5.02$ TeV. *Phys.Lett.*, B719:29–41, 2013. doi: 10.1016/j.physletb.2013.01.012.

[4] Betty Bezverkhny Abelev et al. Long-range angular correlations of π, K and p in p-Pb collisions at $\sqrt{s_{\mathrm{NN}}} = 5.02$ TeV. *Phys.Lett.*, B726:164–177, 2013. doi: 10.1016/j.physletb.2013.08.024.

[5] Betty Bezverkhny Abelev et al. Freeze-out radii extracted from three-pion cumulants in pp, p–Pb and Pb–Pb collisions at the LHC. *Phys.Lett.*, B739:139–151, 2014. doi: 10.1016/j.physletb.2014.10.034.

[6] B.I. Abelev et al. Long range rapidity correlations and jet production in high energy nuclear collisions. *Phys.Rev.*, C80:064912, 2009. doi: 10.1103/PhysRevC.80.064912.

[7] B.I. Abelev et al. Pion Interferometry in Au+Au and Cu+Cu Collisions at RHIC. *Phys.Rev.*, C80:024905, 2009. doi: 10.1103/PhysRevC.80.024905.

[8] Alberto Accardi, N. Armesto, M. Botje, S.J. Brodsky, B. Cole, et al. Hard probes in heavy ion collisions at the LHC: PDFs, shadowing and pA collisions. 2004.

[9] K.H. Ackermann et al. STAR detector overview. *Nucl.Instrum.Meth.*, A499:624–632, 2003. doi: 10.1016/S0168-9002(02)01960-5.

[10] L. Adamczyk et al. Beam energy dependent two-pion interferometry and the freeze-out eccentricity of pions in heavy ion collisions at STAR. 2014.

[11] M. Adamczyk et al. The BRAHMS experiment at RHIC. *Nucl.Instrum.Meth.*, A499:437–468, 2003. doi: 10.1016/S0168-9002(02)01949-6.

[12] D. Adamova et al. Universal pion freezeout in heavy ion collisions. *Phys.Rev.Lett.*, 90:022301, 2003. doi: 10.1103/PhysRevLett.90.022301.

[13] J. Adams et al. Evidence from d + Au measurements for final state suppression of high p(T) hadrons in Au+Au collisions at RHIC. *Phys.Rev.Lett.*, 91:072304, 2003. doi: 10.1103/PhysRevLett.91.072304.

[14] J. Adams et al. Azimuthally sensitive HBT in Au + Au collisions at $\sqrt{s_{\mathrm{NN}}}$ = 200-GeV. *Phys.Rev.Lett.*, 93:012301, 2004. doi: 10.1103/PhysRevLett.93.012301.

[15] J. Adams et al. Pion interferometry in Au+Au collisions at $\sqrt{s_{\mathrm{NN}}}$ = 200-GeV. *Phys.Rev.*, C71:044906, 2005. doi: 10.1103/PhysRevC.71.044906.

[16] A. Adare et al. Quadrupole Anisotropy in Dihadron Azimuthal Correlations in Central d+Au Collisions at $\sqrt{s_{_{NN}}}$ = 200 GeV. *Phys.Rev.Lett.*, 111(21):212301, 2013. doi: 10.1103/PhysRevLett.111.212301.

[17] A. Adare et al. Measurement of long-range angular correlation and quadrupole anisotropy of pions and (anti)protons in central d+Au collisions at $\sqrt{s_{_{NN}}}$ = 200 GeV. 2014.

[18] K. Adcox et al. PHENIX detector overview. *Nucl.Instrum.Meth.*, A499:469–479, 2003. doi: 10.1016/S0168-9002(02)01950-2.

[19] K. Adcox et al. PHENIX central arm tracking detectors. *Nucl.Instrum.Meth.*, A499:489–507, 2003. doi: 10.1016/S0168-9002(02)01952-6.

[20] Clemens Adler, Alexei Denisov, Edmundo Garcia, Michael J. Murray, Herbert Strobele, et al. The RHIC zero degree calorimeter. *Nucl.Instrum.Meth.*, A470:488–499, 2001. doi: 10.1016/S0168-9002(01)00627-1.

[21] S.S. Adler et al. Absence of suppression in particle production at large transverse momentum in $\sqrt{s_{\mathrm{NN}}}$ = 200-GeV d + Au collisions. *Phys.Rev.Lett.*, 91:072303, 2003. doi: 10.1103/PhysRevLett.91.072303.

[22] S.S. Adler et al. Bose-Einstein correlations of charged pion pairs in Au + Au collisions at $\sqrt{s_{\mathrm{NN}}}$ = 200-GeV. *Phys.Rev.Lett.*, 93:152302, 2004. doi: 10.1103/PhysRevLett.93.152302.

[23] S. Afanasiev et al. Source breakup dynamics in Au+Au Collisions at $\sqrt{s_{\mathrm{NN}}}$ = 200-GeV via three-dimensional two-pion source imaging. *Phys.Rev.Lett.*, 100:232301, 2008. doi: 10.1103/PhysRevLett.100.232301.

[24] M.M. Aggarwal et al. An Experimental Exploration of the QCD Phase Diagram: The Search for the Critical Point and the Onset of De-confinement. 2010.

[25] M.M. Aggarwal et al. Pion femtoscopy in $p^{+}p$ collisions at $\sqrt{s}$ = 200 GeV. *Phys.Rev.*, C83:064905, 2011. doi: 10.1103/PhysRevC.83.064905.

[26] M. Aizawa et al. PHENIX central arm particle ID detectors. *Nucl.Instrum.Meth.*, A499:508–520, 2003. doi: 10.1016/S0168-9002(02)01953-8.

[27] M. Allen et al. PHENIX inner detectors. *Nucl.Instrum.Meth.*, A499:549–559, 2003. doi: 10.1016/S0168-9002(02)01956-3.

[28] B. Alver et al. System size dependence of cluster properties from two-particle angular correlations in Cu+Cu and Au+Au collisions at $\sqrt{s_{\mathrm{NN}}}$ = 200-GeV. *Phys.Rev.*, C81:024904, 2010. doi: 10.1103/PhysRevC.81.024904.

[29] E. Andersen et al. Strangeness enhancement at mid-rapidity in Pb Pb collisions at 158-A-GeV/c. *Phys.Lett.*, B449:401–406, 1999. doi: 10.1016/S0370-2693(99)00140-9.

[30] L. Aphecetche et al. PHENIX calorimeter. *Nucl.Instrum.Meth.*, A499:521–536, 2003. doi: 10.1016/S0168-9002(02)01954-X.

[31] S.H. Aronson et al. PHENIX magnet system. *Nucl.Instrum.Meth.*, A499:480–488, 2003. doi: 10.1016/S0168-9002(02)01951-4.

[32] M. Asakawa, S. A. Bass, B. Müller, and C. Nonaka. Transverse velocity dependence of the proton-antiproton ratio as a signature of the qcd critical point. *Phys. Rev. Lett.*, 101:122302, Sep 2008. doi: 10.1103/PhysRevLett.101.122302. URL `http://link.aps.org/doi/10.1103/PhysRevLett.101.122302`.

[33] Masayuki Asakawa and Chiho Nonaka. Critical end point and its consequences. *Nucl.Phys.*, A774:753–756, 2006. doi: 10.1016/j.nuclphysa.2006.06.130.

[34] B.B. Back et al. The PHOBOS detector at RHIC. *Nucl.Instrum.Meth.*, A499:603–623, 2003. doi: 10.1016/S0168-9002(02)01959-9.

[35] B.B. Back et al. Transverse momentum and rapidity dependence of HBT correlations in Au + Au collisions at $\sqrt{s_{\mathrm{NN}}} = 62.4$-GeV and 200-GeV. *Phys.Rev.*, C73:031901, 2006. doi: 10.1103/PhysRevC.73.031901.

[36] A Barducci, R Casalbuoni, S De Curtis, Raoul Gatto, and Giulio Pettini. Chiral-symmetry breaking in qcd at finite temperature and density. *Physics Letters B*, 231(4):463–470, 1989.

[37] Gordon Baym and Peter Braun-Munzinger. Physics of Coulomb corrections in Hanbury-Brown-Twiss interferometry in ultrarelativistic heavy ion collisions. *Nucl.Phys.*, A610:286C–296C, 1996. doi: 10.1016/S0375-9474(96)00363-6.

[38] I.G. Bearden, H. Boggild, J. Boissevain, J. Dodd, B. Erazmus, et al. High-energy Pb + Pb collisions viewed by pion interferometry. *Phys.Rev.*, C58:1656–1665, 1998. doi: 10.1103/PhysRevC.58.1656.

[39] Boris Berdnikov and Krishna Rajagopal. Slowing out-of-equilibrium near the QCD critical point. *Phys.Rev.*, D61:105017, 2000. doi: 10.1103/PhysRevD.61.105017.

[40] Jürgen Berges and Krishna Rajagopal. Color superconductivity and chiral symmetry restoration at non-zero baryon density and temperature. *Nuclear Physics B*, 538(1–2):215 – 232, 1999. ISSN 0550-3213. doi: http://dx.doi.org/10.1016/S0550-3213(98)00620-8. URL `http://www.sciencedirect.com/science/article/pii/S0550321398006208`.

[41] R.S. Bhalerao, Jean-Paul Blaizot, Nicolas Borghini, and Jean-Yves Ollitrault. Elliptic flow and incomplete equilibration at RHIC. *Phys.Lett.*, B627:49–54, 2005. doi: 10.1016/j.physletb.2005.08.131.

[42] J. D. Bjorken. Highly relativistic nucleus-nucleus collisions: The central rapidity region. *Phys. Rev. D*, 27:140–151, Jan 1983. doi: 10.1103/PhysRevD.27.140. URL `http://link.aps.org/doi/10.1103/PhysRevD.27.140`.

[43] H. Boggild et al. Two proton correlations near mid-rapidity in p + Pb and S + Pb collisions at the CERN SPS. *Phys.Lett.*, B458:181–189, 1999. doi: 10.1016/S0370-2693(99)00614-0.

[44] M.G. Bowler. Extended Sources, Final State Interactions and Bose-Einstein Correlations. *Z.Phys.*, C39:81, 1988. doi: 10.1007/BF01560395.

[45] Piotr Bozek, Wojciech Broniowski, and Giorgio Torrieri. Mass hierarchy in identified particle distributions in proton-lead collisions. *Phys.Rev.Lett.*, 111:172303, 2013. doi: 10.1103/PhysRevLett.111.172303.

[46] Frank R. Brown, Frank P. Butler, Hong Chen, Norman H. Christ, Zhihua Dong, Wendy Schaffer, Leo I. Unger, and Alessandro Vaccarino. On the existence of a phase transition for QCD with three light quarks. *Phys. Rev. Lett.*, 65:2491–2494, Nov 1990. doi: 10.1103/PhysRevLett.65.2491. URL `http://link.aps.org/doi/10.1103/PhysRevLett.65.2491`.

[47] N. Cabibbo and G. Parisi. Exponential hadronic spectrum and quark liberation. *Physics Letters B*, 59(1):67 – 69, 1975. ISSN 0370-2693. doi: http://dx.doi.org/10.1016/0370-2693(75)90158-6. URL `http://www.sciencedirect.com/science/article/pii/0370269375901586`.

[48] Z. Chajecki. Pion interferemetry from p + p to Au + Au in STAR. 2005.

[49] Scott Chapman and Ulrich W. Heinz. HBT correlators: Current formalism versus Wigner function formulation. *Phys.Lett.*, B340:250–253, 1994. doi: 10.1016/0370-2693(94)01277-6.

[50] Scott Chapman, J. Rayford Nix, and Ulrich W. Heinz. Extracting source parameters from Gaussian fits to two particle correlations. *Phys.Rev.*, C52:2694–2703, 1995. doi: 10.1103/PhysRevC.52.2694.

[51] Scott Chapman, Pierre Scotto, and Ulrich W. Heinz. A New cross term in the two particle HBT correlation function. *Phys.Rev.Lett.*, 74:4400–4403, 1995. doi: 10.1103/PhysRevLett.74.4400.

[52] Serguei Chatrchyan et al. Observation of long-range near-side angular correlations in proton-lead collisions at the LHC. *Phys.Lett.*, B718:795–814, 2013. doi: 10.1016/j.physletb.2012.11.025.

[53] A.K. Chaudhuri. Centrality dependence of elliptic flow and QGP viscosity. *J.Phys.*, G37:075011, 2010. doi: 10.1088/0954-3899/37/7/075011.

[54] J. C. Collins and M. J. Perry. Superdense matter: Neutrons or asymptotically free quarks? *Phys. Rev. Lett.*, 34:1353–1356, May 1975. doi: 10.1103/PhysRevLett.34.1353. URL `http://link.aps.org/doi/10.1103/PhysRevLett.34.1353`.

[55] Laszlo P. Csernai, Joseph.I. Kapusta, and Larry D. McLerran. On the Strongly-Interacting Low-Viscosity Matter Created in Relativistic Nuclear Collisions. *Phys.Rev.Lett.*, 97:152303, 2006. doi: 10.1103/PhysRevLett.97.152303.

[56] T. Csorgo, B. Lorstad, J. Schmid-Sorensen, and Andras Ster. Partial coherence in the core/halo picture of Bose-Einstein n-particle correlations. *Eur.Phys.J.*, C9: 275–281, 1999. doi: 10.1007/s100529900024.

[57] A. Drees, L. Ahrens, J. Alessi, M. Bai, D. Barton, et al. Summary of the RHIC performance during the FY07 heavy ion run. *Conf.Proc.*, C070625:722, 2007.

[58] Kevin Dusling and Raju Venugopalan. Azimuthal collimation of long range rapidity correlations by strong color fields in high multiplicity hadron-hadron collisions. *Phys.Rev.Lett.*, 108:262001, 2012. doi: 10.1103/PhysRevLett.108.262001.

[59] Kevin Dusling and Raju Venugopalan. Comparison of the color glass condensate to dihadron correlations in proton-proton and proton-nucleus collisions. *Phys.Rev.*, D87(9):094034, 2013. doi: 10.1103/PhysRevD.87.094034.

[60] Akitomo Enokizono. Space-time evolution of hot and dense matter probed by Bose-Einstein correlation in $Au + Au$ collisions at $\sqrt{s_{NN}} = 200$ GeV. 2004.

[61] C.J. Gardner, N.P. Abreu, L. Ahrens, J.G. Alessi, M. Bai, et al. Setup and Performance of RHIC for the 2008 Run with Deuteron and Gold Collisions. *Conf.Proc.*, C0806233:WEPP011, 2008.

[62] R.V. Gavai and Sourendu Gupta. QCD at finite chemical potential with six time slices. *Phys.Rev.*, D78:114503, 2008. doi: 10.1103/PhysRevD.78.114503.

[63] Gerson Goldhaber, Sulamith Goldhaber, Won-Yong Lee, and Abraham Pais. Influence of Bose-Einstein statistics on the anti-proton proton annihilation process. *Phys.Rev.*, 120:300–312, 1960. doi: 10.1103/PhysRev.120.300.

[64] Rajan Gupta. Introduction to lattice QCD: Course. pages 83–219, 1997.

[65] M. Gyulassy, S.K. Kauffmann, and L.W. Wilson. Pion Interferometry of Nuclear Collisions. 1. Theory. *Phys.Rev.*, C20:2267–2292, 1979. doi: 10.1103/PhysRevC.20.2267.

[66] Miklos Gyulassy and Larry McLerran. New forms of QCD matter discovered at RHIC. *Nucl.Phys.*, A750:30–63, 2005. doi: 10.1016/j.nuclphysa.2004.10.034.

[67] H. Hahn, E. Forsyth, H. Foelsche, M. Harrison, J. Kewisch, et al. The RHIC design overview. *Nucl.Instrum.Meth.*, A499:245–263, 2003. doi: 10.1016/S0168-9002(02)01938-1.

[68] M. A. Halasz, A. D. Jackson, R. E. Shrock, M. A. Stephanov, and J. J. M. Verbaarschot. Phase diagram of QCD. *Phys. Rev. D*, 58:096007, Sep 1998. doi: 10.1103/PhysRevD.58.096007. URL `http://link.aps.org/doi/10.1103/PhysRevD.58.096007`.

[69] R. Hanbury Brown and R.Q. Twiss. A Test of a new type of stellar interferometer on Sirius. *Nature*, 178:1046–1048, 1956. doi: 10.1038/1781046a0.

[70] M. Harrison, T. Ludlam, and S. Ozaki. RHIC project overview. *Nucl.Instrum.Meth.*, A499:235–244, 2003. doi: 10.1016/S0168-9002(02)01937-X.

[71] Ulrich W. Heinz. Hanbury-Brown/Twiss interferometry for relativistic heavy ion collisions: Theoretical aspects. 1996.

[72] M. Herrmann and G.F. Bertsch. Source dimensions in ultrarelativistic heavy ion collisions. *Phys.Rev.*, C51:328–338, 1995. doi: 10.1103/PhysRevC.51.328.

[73] Norbert Herrmann, Johannes P. Wessels, and Thomas Wienold. Collective flow in heavy-ion collisions. *Annual Review of Nuclear and Particle Science*, 49(1): 581–632, 1999. doi: 10.1146/annurev.nucl.49.1.581. URL `http://dx.doi.org/10.1146/annurev.nucl.49.1.581`.

[74] L. Hulthén and M. Sugawara. *Handbuch der Physik*, volume 39. Springer-Verlag, 1957.

[75] C.M. Hung and Edward V. Shuryak. Hydrodynamics near the QCD phase transition: Looking for the longest lived fireball. *Phys.Rev.Lett.*, 75:4003–4006, 1995. doi: 10.1103/PhysRevLett.75.4003.

[76] Vardan Khachatryan et al. Observation of Long-Range Near-Side Angular Correlations in Proton-Proton Collisions at the LHC. *JHEP*, 1009:091, 2010. doi: 10.1007/JHEP09(2010)091.

[77] Adam Kisiel. Overview of the femtoscopy studies in Pb Pb and p p collisions at the LHC by the ALICE experiment. *PoS*, WPCF2011:003, 2011.

[78] Peter F. Kolb, Josef Sollfrank, and Ulrich W. Heinz. Anisotropic transverse flow and the quark hadron phase transition. *Phys.Rev.*, C62:054909, 2000. doi: 10.1103/PhysRevC.62.054909.

[79] Lokesh Kumar. Systematics of kinetic freeze-out properties in high energy collisions from STAR. *Nuclear Physics A*, (0):–, 2014. ISSN 0375-9474. doi: http://dx.doi.org/10.1016/j.nuclphysa.2014.08.085. URL `http://www.sciencedirect.com/science/article/pii/S0375947414003455`.

[80] Roy Lacey. PHENIX Measurements of Higher-order Flow Harmonics in Au+Au collisions at $\sqrt{s_{NN}} = 200$ GeV. *J.Phys.*, G38:124048, 2011.

[81] Roy A. Lacey, N.N. Ajitanand, J.M. Alexander, P. Chung, J. Jia, et al. An Estimate for the location of QCD critical end point. 2007.

[82] Roy A. Lacey, Rui Wei, N.N. Ajitanand, and A. Taranenko. Initial eccentricity fluctuations and their relation to higher-order flow harmonics. *Phys.Rev.*, C83: 044902, 2011. doi: 10.1103/PhysRevC.83.044902.

[83] Roy A. Lacey, Yi Gu, X. Gong, D. Reynolds, N.N. Ajitanand, et al. Is anisotropic flow really acoustic? 2013.

[84] Roy A. Lacey, D. Reynolds, A. Taranenko, N.N. Ajitanand, J.M. Alexander, et al. Acoustic scaling of anisotropic flow in shape-engineered events: implications for extraction of the specific shear viscosity of the quark gluon plasma. 2013.

[85] Michael Annan Lisa, Scott Pratt, Ron Soltz, and Urs Wiedemann. Femtoscopy in relativistic heavy ion collisions. *Ann.Rev.Nucl.Part.Sci.*, 55:357–402, 2005. doi: 10.1146/annurev.nucl.55.090704.151533.

[86] Brian Love. The Design, Implementation and Performance of the PHENIX Time-of-Flight West Detector.

[87] Gines Martinez. Advances in Quark Gluon Plasma. 2013.

[88] H. Masui. Anisotropic flow in $\sqrt{s_{NN}} = 200$ GeV Cu+Cu and Au+Au collisions at PHENIX. *Nucl.Phys.*, A774:511–514, 2006.

[89] J.T. Mitchell et al. Event reconstruction in the PHENIX central arm spectrometers. *Nucl.Instrum.Meth.*, A482:491–512, 2002. doi: 10.1016/S0168-9002(01)01512-1.

[90] T. Mizoguchi and M. Biyajima. An Improved formulation for three charged particles correlations in terms of Coulomb wave functions with degree of coherence. *Phys.Lett.*, B499:245–252, 2001. doi: 10.1016/S0370-2693(01)00048-X.

[91] Christoph Montag and Alexei Fedotov. RHIC Low Energy Acceleration. *PoS*, CPOD2013:044, 2013.

[92] F. Pilat et al. Operations and Performance of RHIC as a Cu-Cu Collider. In *Particle Accelerator, IEEE Conference*, 2005. doi: 10.1109/PAC.2005.1591791.

[93] S. Pratt. Pion Interferometry for Exploding Sources. *Phys.Rev.Lett.*, 53:1219–1221, 1984. doi: 10.1103/PhysRevLett.53.1219.

[94] S. Pratt. Coherence and Coulomb Effects on Pion Interferometry. *Phys.Rev.*, D33: 72–79, 1986. doi: 10.1103/PhysRevD.33.72.

[95] M.L. Purschke, S.C. Adler, E. Desmond, L. Ewell, J. Haggerty, et al. The PHENIX online computing system. *IEEE Trans.Nucl.Sci.*, 47:51–55, 2000. doi: 10.1109/23.846116.

[96] Fabrice Retiere and Michael Annan Lisa. Observable implications of geometrical and dynamical aspects of freeze out in heavy ion collisions. *Phys.Rev.*, C70:044907, 2004. doi: 10.1103/PhysRevC.70.044907.

[97] Dirk H. Rischke and Miklos Gyulassy. The Time delay signature of quark - gluon plasma formation in relativistic nuclear collisions. *Nucl.Phys.*, A608:479–512, 1996. doi: 10.1016/0375-9474(96)00259-X.

[98] Dirk H. Rischke, Yaris Pursun, Joachim A. Maruhn, Horst Stoecker, and Walter Greiner. The Phase transition to the quark - gluon plasma and its effects on hydrodynamic flow. *Heavy Ion Phys.*, 1:309–322, 1995.

[99] Paul Romatschke and Ulrike Romatschke. Viscosity information from relativistic nuclear collisions: How perfect is the fluid observed at RHIC? *Phys. Rev. Lett.*, 99: 172301, Oct 2007. doi: 10.1103/PhysRevLett.99.172301. URL `http://link.aps.org/doi/10.1103/PhysRevLett.99.172301`.

[100] C.A. Salgado, J. Alvarez-Muniz, F. Arleo, N. Armesto, M. Botje, et al. Proton-Nucleus Collisions at the LHC: Scientific Opportunities and Requirements. *J.Phys.*, G39:015010, 2012. doi: 10.1088/0954-3899/39/1/015010.

[101] Christian Schmidt. QCD thermodynamics at zero and non-zero density. *Nucl.Phys.*, A820:41C–48C, 2009. doi: 10.1016/j.nuclphysa.2009.01.017.

[102] Edward Shuryak and Ismail Zahed. High-multiplicity pp and pA collisions: Hydrodynamics at its edge. *Phys.Rev.*, C88(4):044915, 2013. doi: 10.1103/PhysRevC.88.044915.

[103] Yu.M. Sinyukov, R. Lednicky, J. Pluta, B. Erazmus, and S.V. Akkelin. Coulomb corrections for interferometry analysis of expanding hadron systems. 1997.

[104] M.A. Stephanov. QCD phase diagram: An Overview. *PoS*, LAT2006:024, 2006.

[105] M.A. Stephanov. Non-Gaussian fluctuations near the QCD critical point. *Phys.Rev.Lett.*, 102:032301, 2009. doi: 10.1103/PhysRevLett.102.032301.

[106] Mikhail A. Stephanov. QCD phase diagram and the critical point. *Prog.Theor.Phys.Suppl.*, 153:139–156, 2004. doi: 10.1142/S0217751X05027965.

[107] Misha A. Stephanov, K. Rajagopal, and Edward V. Shuryak. Event-by-event fluctuations in heavy ion collisions and the QCD critical point. *Phys.Rev.*, D60:114028, 1999. doi: 10.1103/PhysRevD.60.114028.

[108] Boris Tomasik. Blast wave snapshots from RHIC. 2003.

[109] Urs Achim Wiedemann, Pierre Scotto, and Ulrich W. Heinz. Transverse momentum dependence of Hanbury-Brown-Twiss correlation radii. *Phys.Rev.*, C53:918–931, 1996. doi: 10.1103/PhysRevC.53.918.

[110] Frank Wilczek. Asymptotic freedom: From paradox to paradigm. *Proc.Nat.Acad.Sci.*, 102:8403–8413, 2005. doi: 10.1103/RevModPhys.77.857.

[111] Li Yi. Azimuthal anisotropy measurements by STAR. *Nuclear Physics A*, 926(0): 198 – 204, 2014.

A. Correlation functions

These are the projected 3-D correlation functions used in extracting the HBT parameters discussed in this thesis. The fit lines are from the Sinyukov function.

A.1. $Au + Au$ $\sqrt{s_{NN}}$ = 39 GeV correlation functions

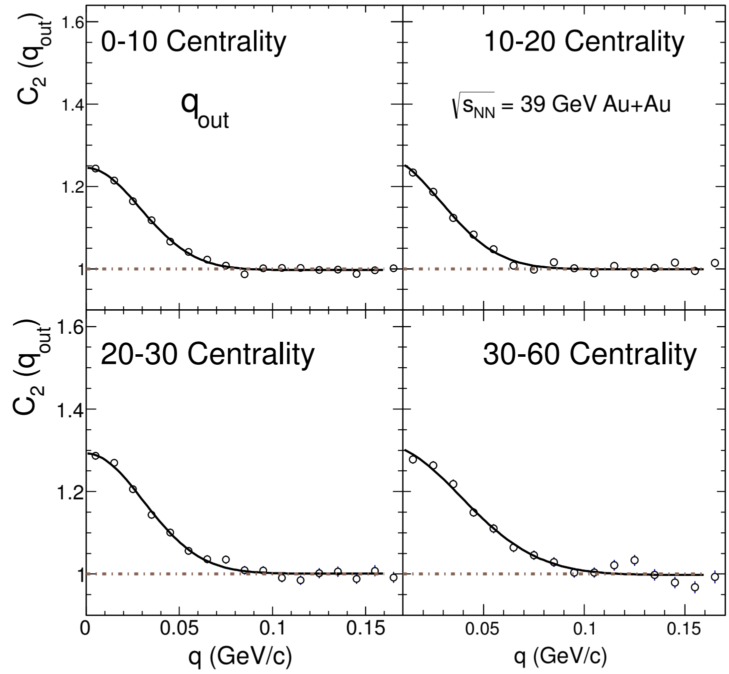

Figure A.1.: $Au + Au$ $\sqrt{s_{NN}} = 39$ GeV correlation functions: q_{out}

A.2. $Au + Au$ $\sqrt{s_{NN}}$ = 62 GeV correlation functions

A.3. $Au + Au$ $\sqrt{s_{NN}}$ = 200 GeV correlation functions

A.4. $Cu + Cu$ $\sqrt{s_{NN}}$ = 200 GeV correlation functions

A.5. $d + Au$ $\sqrt{s_{NN}}$ = 200 GeV correlation functions

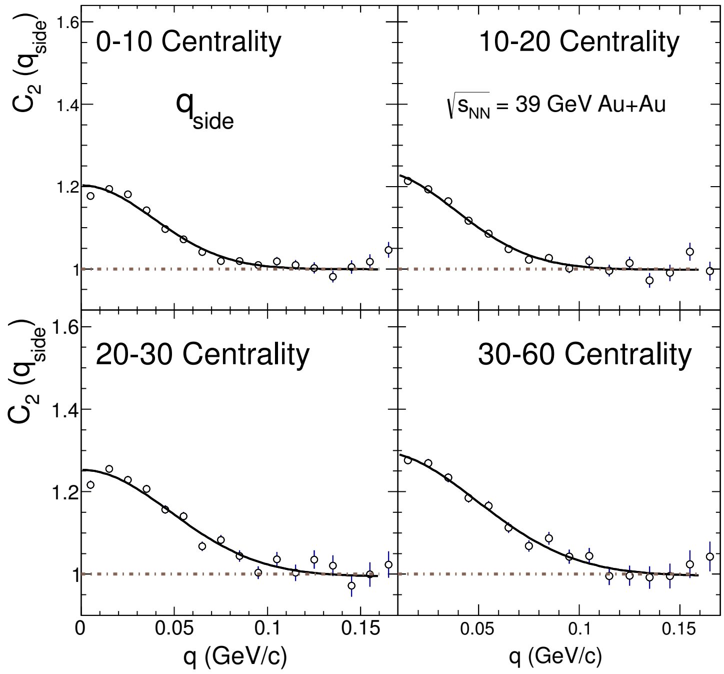

Figure A.2.: $Au + Au$ $\sqrt{s_{NN}} = 39$ GeV correlation functions: q_{side}

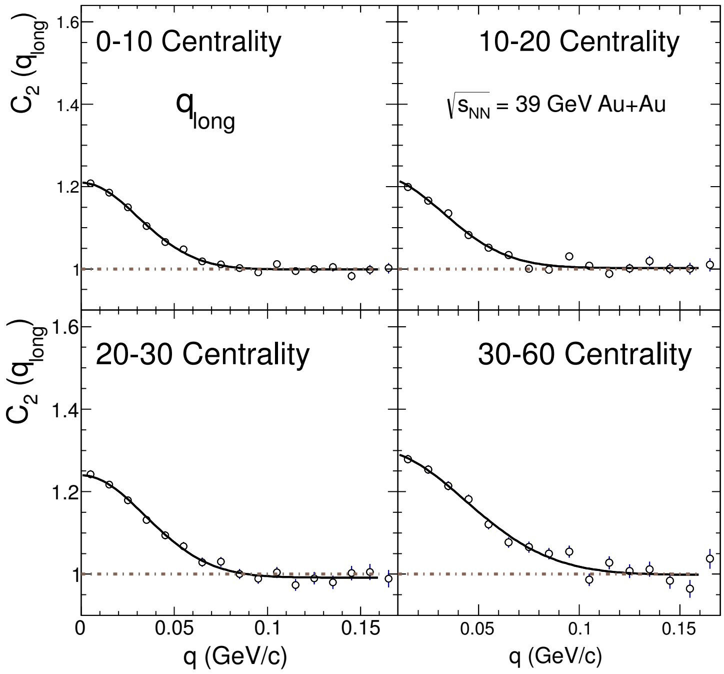

Figure A.3.: $Au + Au$ $\sqrt{s_{NN}} = 39$ GeV correlation functions: q_{long}

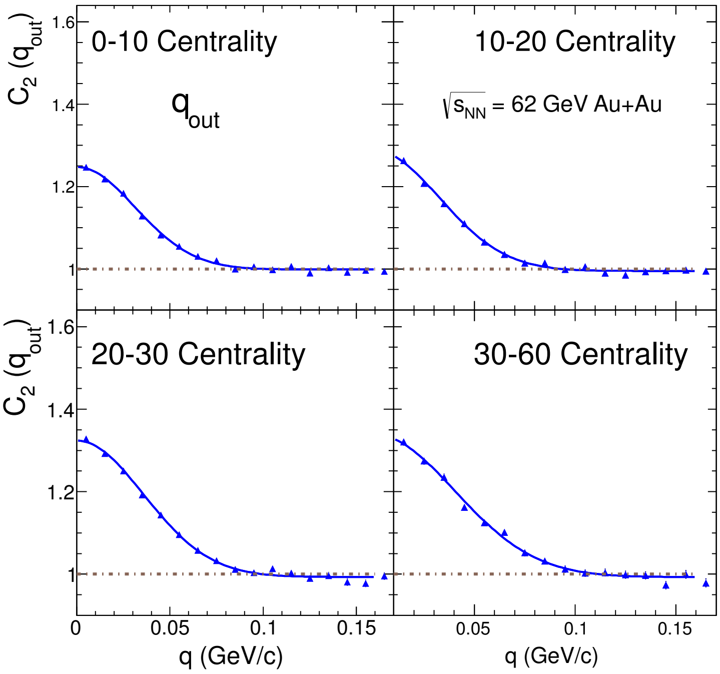

Figure A.4.: $Au + Au$ $\sqrt{s_{NN}} = 62$ GeV correlation functions: q_{out}

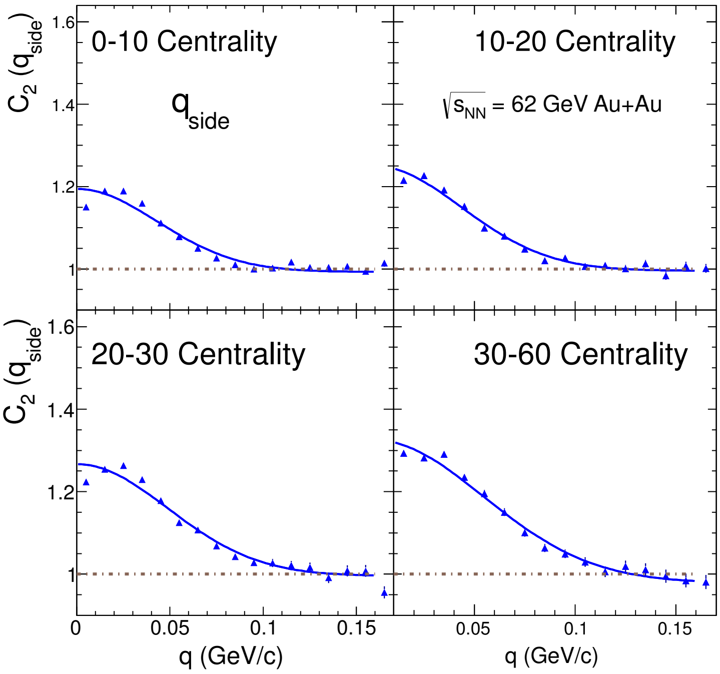

Figure A.5.: $Au + Au$ $\sqrt{s_{NN}} = 62$ GeV correlation functions: q_{side}

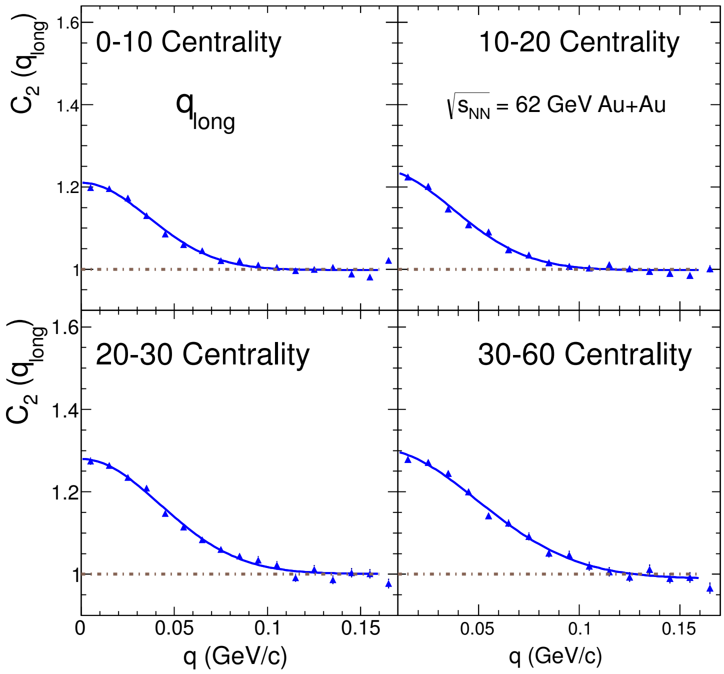

Figure A.6.: $Au + Au$ $\sqrt{s_{NN}} = 62$ GeV correlation functions: q_{long}

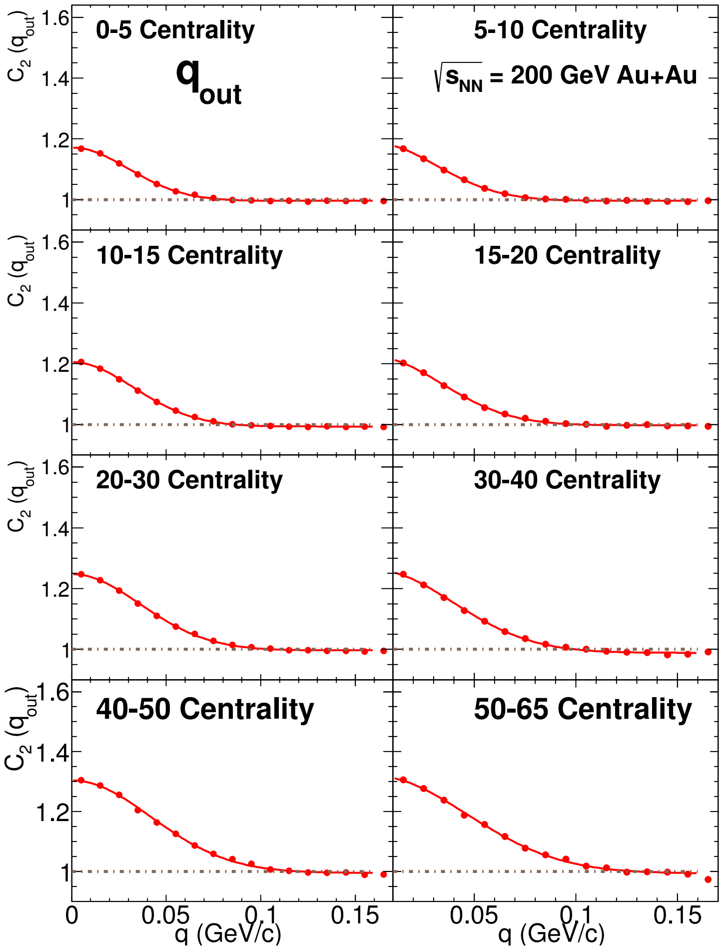

Figure A.7.: $Au + Au$ $\sqrt{s_{NN}} = 200$ GeV correlation functions: q_{out}

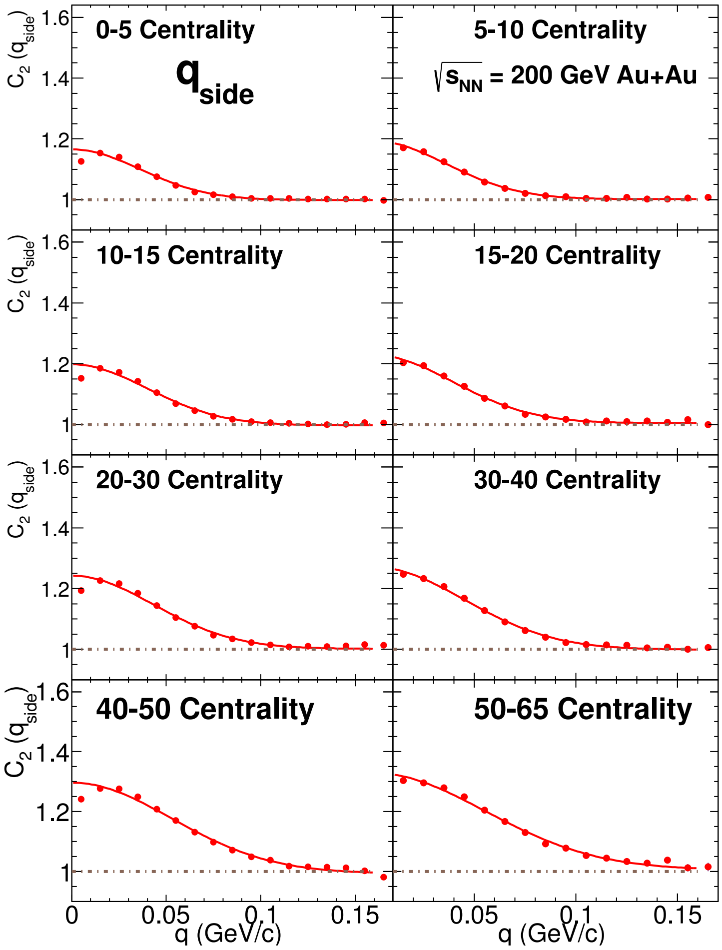

Figure A.8.: $Au + Au$ $\sqrt{s_{NN}}$ = 200 GeV correlation functions: q_{side}

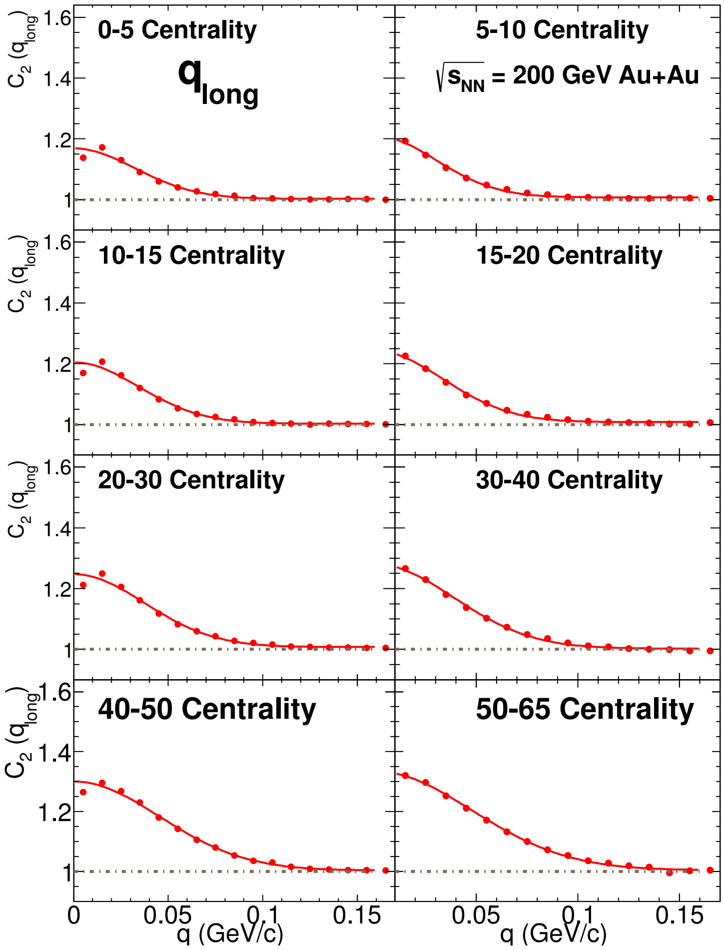

Figure A.9.: $Au + Au$ $\sqrt{s_{NN}} = 200$ GeV correlation functions: q_{long}

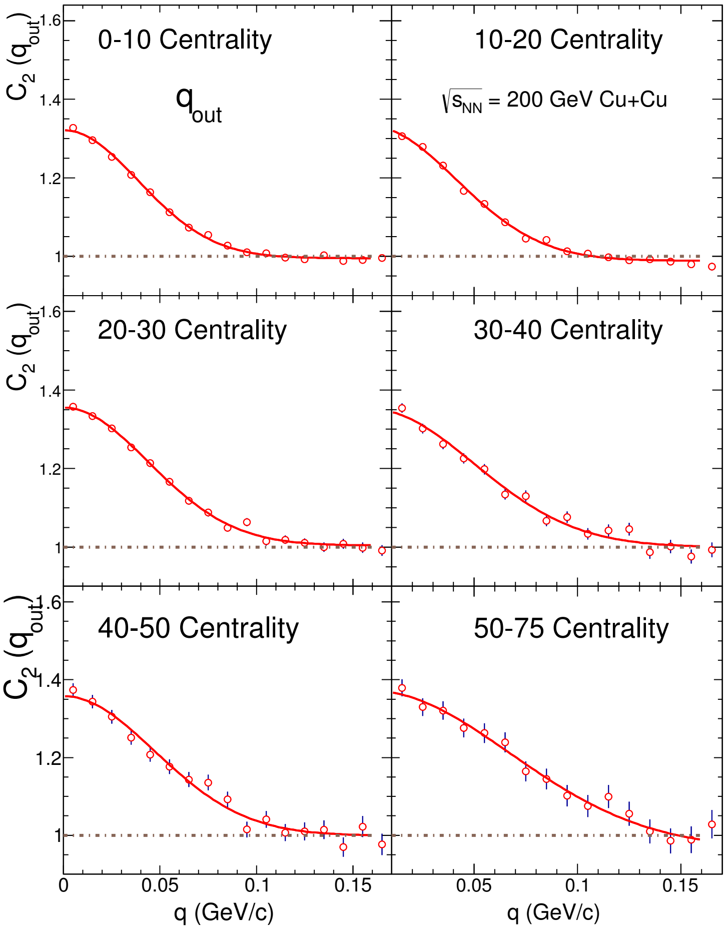

Figure A.10.: $Cu + Cu$ $\sqrt{s_{NN}}$ = 200 GeV correlation functions: q_{out}

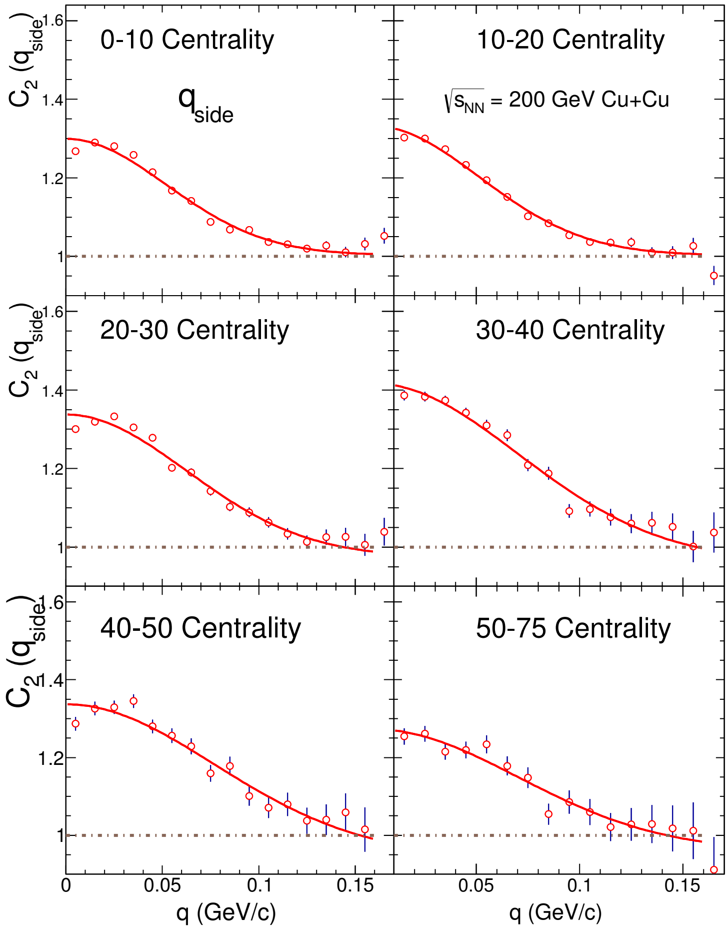

Figure A.11.: $Cu + Cu$ $\sqrt{s_{NN}}$ = 200 GeV correlation functions: q_{side}

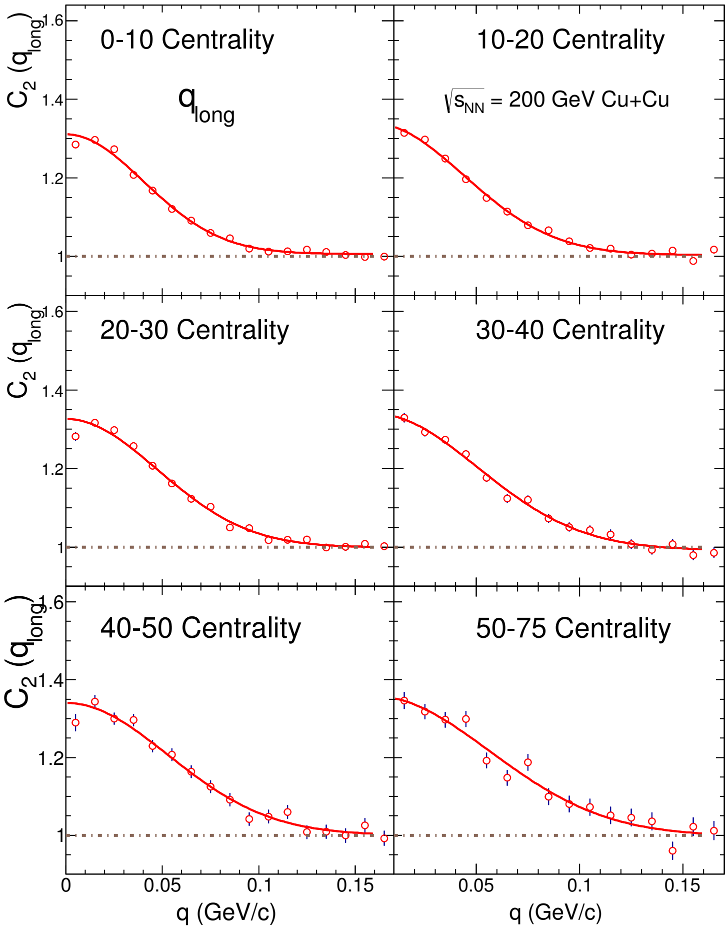

Figure A.12.: $Cu + Cu$ $\sqrt{s_{NN}} = 200$ GeV correlation functions: q_{long}

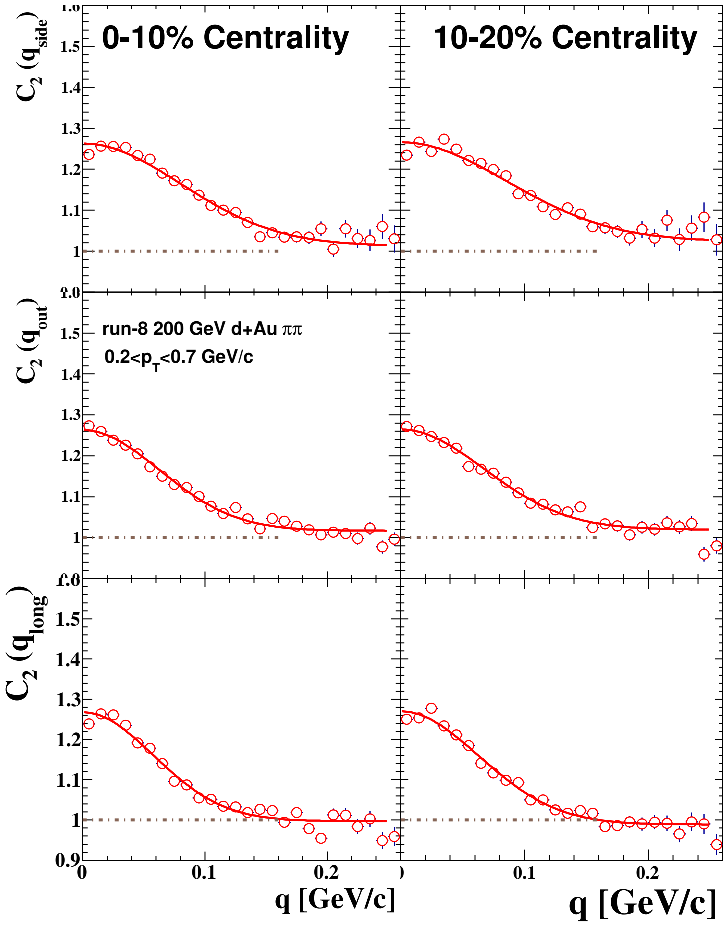

Figure A.13.: $d + Au$ $\sqrt{s_{NN}} = 200$ GeV correlation functions: 0–10% and 10–20% centrality.

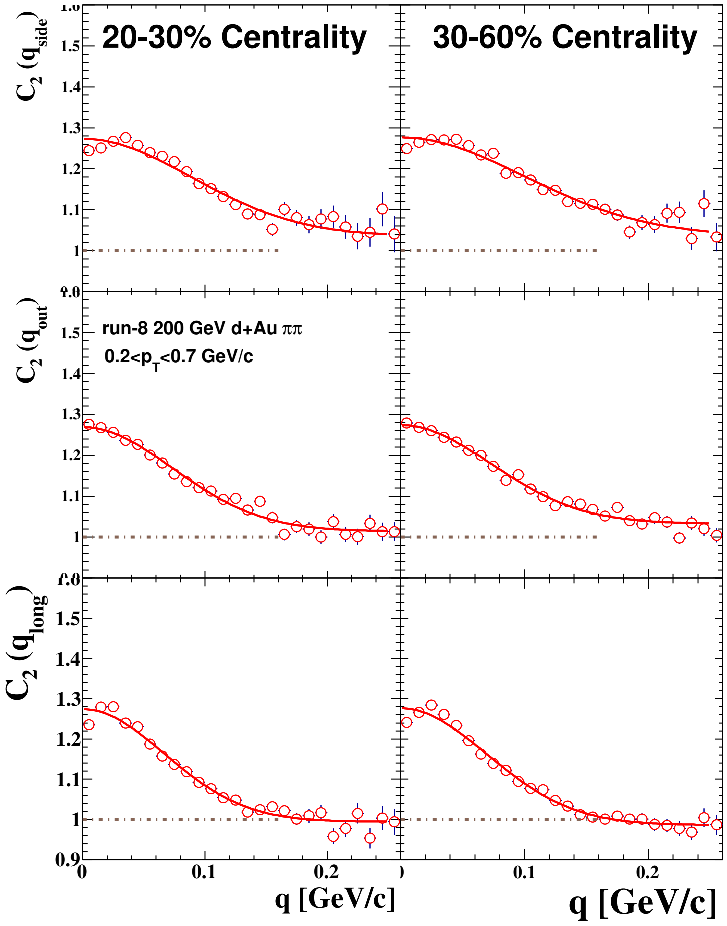

Figure A.14.: $d + Au$ $\sqrt{s_{NN}} = 200$ GeV correlation functions: 20–30% and 30–60% centrality.